

Lawrence Berkeley National Laboratory

Lawrence Berkeley National Laboratory

Title

LASER PHOTOCHEMICAL REACTION DYNAMICS IN FORMALDEHYDE

Permalink

<https://escholarship.org/uc/item/63r800b8>

Author

Zughul, Muhammad B.

Publication Date

1978-08-01

LBL-8050

c. 2

LASER PHOTOCHEMICAL REACTION DYNAMICS
IN FORMALDEHYDE

Muhammad B. Zughul
(Ph. D. Thesis)

RECEIVED
LAWRENCE
BERKELEY LABORATORY

NOV 17 1978

August 1978

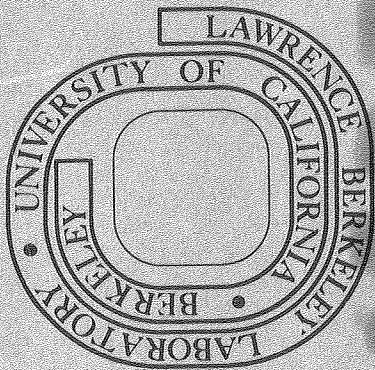
LIBRARY AND
DOCUMENTS SECTION

Prepared for the U. S. Department of Energy
under Contract W-7405-ENG-48

TWO-WEEK LOAN COPY

This is a Library Circulating Copy
which may be borrowed for two weeks.

For a personal retention copy, call
Tech. Info. Division, Ext. 6782



LBL-8050
c. 2

— LEGAL NOTICE —

This report was prepared as an account of work sponsored by the United States Government. Neither the United States nor the Department of Energy, nor any of their employees, nor any of their contractors, subcontractors, or their employees, makes any warranty, express or implied, or assumes any legal liability or responsibility for the accuracy, completeness or usefulness of any information, apparatus, product or process disclosed, or represents that its use would not infringe privately owned rights.

LASER PHOTOCHEMICAL REACTION DYNAMICS IN FORMALDEHYDE

Muhammad Bari Ahmad Zughul

Materials and Molecular Research Division
Lawrence Berkeley Laboratory
University of California
Department of Chemistry
Berkeley, California 94720

ABSTRACT

Appearance rate constants of molecular photochemical products have been measured following laser photolysis of formaldehyde in the near ultraviolet. The pressure dependence of appearance rates has been studied for three formaldehyde isotopic species, namely: H_2CO , HDCO , and D_2CO . The effect of added foreign gases on those rates in H_2CO has been determined for He, Ar, Xe, and NO. The energy dependence of photodissociation rates has been examined following laser photolysis at 354.7 and 299.1 nm and the results compared with earlier data obtained at 337.1 nm. The corresponding appearance rates measured for other carbonyls such as acrolein, propynal, ketene, and cyclobutanone were found to be much faster and greater than gas kinetic, indicating a photodissociation mechanism which is different from that of formaldehyde. The decay rates of $\text{CO}(v=1)$ have been measured for several collision partners including H_2CO , HDCO , acrolein, ketene, cis-2-butene, and cyclobutanone. The measurement of appearance rates for the radical dissociation channel in formaldehyde by monitoring H-atom production has been attempted using three different techniques. Those include resonance fluorescence, resonance absorption, and two-photon excited fluorescence of Hydrogen Lyman- α photons. Details of procedures followed and experimental limitations are also given.

C. Bradley Moore

Dedicated to my parents

CONTENTS

I.	Introduction	1
II.	Dynamics of Photopredissociation in Formaldehyde	7
	A. Spectroscopy	7
	B. Decay of the Excited Singlet ($^1A''$)	9
	1. Fluorescence Lifetimes and Decay Rates	9
	(i) H_2CO	12
	(ii) D_2CO	13
	(iii) HDCO	14
	2. Appearance Rates of Photochemical Products	15
	C. Quantum Yields and Branching Ratios.	16
	1. Pure H_2CO	16
	2. Pure D_2CO	19
	3. Pure HDCO.	19
	D. Effect of Foreign Gases on Branching Ratios.	21
	1. Nitric Oxide	21
	2. Oxygen	23
	3. Argon and Nitrogen	25
	E. Predissociation Mechanism.	26
	1. Potential Energy Surfaces.	26
	2. Geometrical Rearrangement to Hydroxymethylene.	29
III.	Experimental	32
	A. General Description.	32
	B. The Nd:YAG Laser	32
	C. Generation of the Optical Harmonics.	47
	1. Phase Matching	48

2. Conversion Efficiency.	53
(i) Second Harmonic.	55
(ii) Third Harmonic	55
(iii) Fourth Harmonic.	56
D. Stimulated Raman Scattering.	57
E. Infrared Fluorescence Detection.	64
F. Signal Processing Electronics.	69
G. Gas Handling System.	70
1. Vacuum Line.	70
2. Gas Flow System.	71
3. Fluorescence Cell.	72
H. Gas Preparation.	75
1. Formaldehyde	75
2. Ketene	76
3. Acrolein	76
4. Propynal	77
5. Cyclobutanone.	77
6. Other Gases.	77
V. Experimental Set Up.	77
1. Set Up for Photolysis at 354.7 nm.	78
2. Set Up for Photolysis at 266 and 299.1 nm.	81
3. Detector Optical Alignment and Signal Optimization	82
IV. Results.	86
A. Formaldehyde	86
1. H ₂ CO (354.7 nm).	86
2. H ₂ CO + Foreign Gases	99

3.	H ₂ CO (299.1 nm)	108
4.	D ₂ CO (354.7 nm)	122
5.	HDCO (354.7 nm)	130
B.	Propynal	130
C.	Acrolein	130
D.	Ketene	140
E.	Cyclobutanone	154
F.	Summary of Results	166
V.	Hydrogen Atom Detection	169
A.	General Description	169
B.	Resonance Trapping of H _α Fluorescence	169
C.	Collisional Deactivation of H ₂ (² S, ² P) States	172
D.	Doppler-Free Two-Photon 1S-2S Excitation	174
1.	1S-2S Transition Rate	175
2.	Photoionization of the 2S State	177
3.	Two-Photon Laser Excitation Source	178
E.	H _α Detection and Electronic Processing System	179
F.	Gas Handling System	180
G.	Resonance Fluorescence Cell	181
H.	Resonance Absorption Cell	182
I.	Two-Photon Excitation Cell	182
J.	H _α Resonance Lamp	182
K.	Resonance Fluorescence and Lamp Performance	186
1.	Spectroscopic Apparatus	187
2.	Resonance Line Profile	188

3.	Resonance Lamp Spectrum.	193
4.	H ₂ CO Absorption Coefficient.	193
L.	Detection By Resonance Absorption.	197
M.	Doppler-Free Two-Photon Excited H _α Fluorescence.	201
N.	Detection by Three-Photon Ionization	202
VI.	Discussion	206
A.	Appearance Rates of Molecular Photoproducts.	206
B.	CO(v=1) Decay Rates.	214
C.	Summary and Suggestions for Future Work.	215
VII.	References	219

ACKNOWLEDGMENTS

I would like to express my sincere gratitude to Professor C. Bradley Moore for his continuous guidance and encouragement throughout this work. It would be impossible to thank him enough for his great contribution to my scientific development and research ability. I am very grateful for the resourcefulness with which he helped me obtain essential financial support, and I shall always treasure the kindness and friendship he extended to me.

I would also like to thank Professors Harold S. Johnston and T. Kenneth Gustafson for reading this thesis and criticizing the manuscript.

I have learned a great deal from the many useful discussions I have had with members of this research group: Paul L. Houston helped out with early stages of experimental work, as did Andy Baronavski, John Clark, Steve Leone, Glen Macdonald, and Nick Nogar. I have had many discussions and enjoyed working with Jim Weisshaar, Jay Wissenfeld, Cameron Dasch, Floyd Hovis, Donald Douglass, Chang-Chi Mei and Mike Berman. Andy Kung has been of great help in various aspects of laser work and maintenance. The many discussions we had stand out in my memory. To these and all other members of this splendid research group, many thanks.

Jackie Denney has been a blessing ever since she joined the group as secretary. To her exceptional character and beautiful work efficiency, many, many thanks.

Finally, I would like to thank Lorine Hesleph, Jean Wolslegel, and Valerie Kelly for their tremendous help in typing this thesis and their perceptiveness in deciphering my handwriting.

This work was supported by Division of Advanced Systems Materials Production, Office of Advanced Isotope Separation, U. S. Department of Energy.

I. INTRODUCTION

Unravelling the dynamics of formaldehyde photophysics and photochemistry is of fundamental importance in the fields of photochemistry, radiationless transitions, isotope separation, photochemical air pollution and interstellar molecular spectroscopy.

The fact that it is the smallest carbonyl compound renders its chemistry a possible prototype for higher aldehydes and ketones. Its photophysical and photochemical behavior serves as a testing ground for theories of radiationless transitions and energy transfer, subjects which occupy a central part of chemical reaction dynamics.

The rather large isotope effects on the radiative and non-radiative transition rates in formaldehyde,^{1,2} combined with the recent success of laser isotope separation,³⁻⁷ motivates further studies of the photophysical pathways which govern its predissociation. Those studies will prove essential towards a better understanding of the role formaldehyde plays in the chain of photochemical reactions with other gases found as pollutants of urban atmospheres,^{8,9} and also, in interstellar space.^{10,11}

Absorption of ultraviolet photons in the wavelength range 360-260 nm excites formaldehyde into the first excited singlet state ($^1A''$), an $n \rightarrow \pi^*$ transition. This subsequently either fluoresces into the ground singlet ($^1A''$), or decays non-radiatively into the ground state or into photochemical products.¹²⁻¹⁴ Examination of the energy dependence of the fluorescence lifetimes and photochemical quantum yields reveals the following features:

1. The fluorescence lifetimes decrease rapidly with excitation energy and show a pronounced deuterium isotope effect; the lifetimes increasing in the order: $\text{H}_2\text{CO} < \text{HDCO} < \text{D}_2\text{CO}$.^{1,2,15-17} The observed decay rates increase with energy of excitation more so than in higher aldehydes or ketones.^{18,19}
2. There appears to be no smooth correlation between the decay rates and the particular vibrational modes excited.^{1,2}
3. The photochemical quantum yields increase with energy of excitation approaching unity beyond the energy threshold for radical dissociation.^{20,21} Molecular photoproduct quantum yields show a deuterium isotope effect with D_2CO having the lowest quantum yield near the origin of the excited singlet.^{20,21} These yields increase with excitation energy until the energy threshold for radical dissociation is exceeded, whereby radical production begins to compete with the molecular channel.²⁰⁻²⁴
4. There is also no apparent smooth correlation between photochemical quantum yields and the vibrational modes excited. Near the energy threshold for radical dissociation, the radical product quantum yields increase rapidly with excitation energy but remain constant beyond that.^{20,21,23,24}

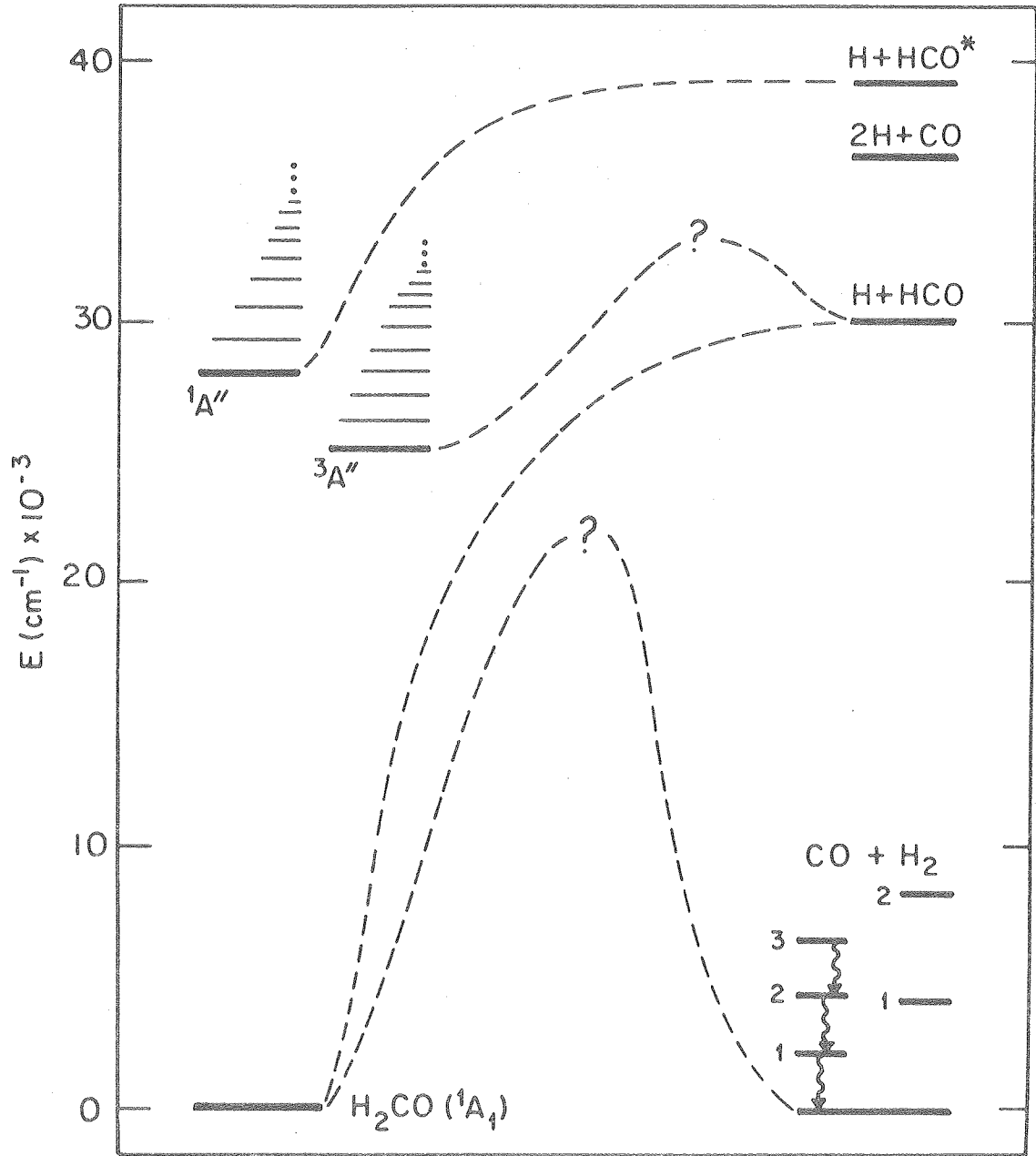
In recent experiments carried out by Houston and Moore in which the appearance rates of molecular photoproducts were measured as a function of formaldehyde gas pressure, it was found that those rates were pressure dependent when measured at 337.1 nm wavelength of excitation.²⁵ They were also found to be slower than the measured decay rates of the excited singlet at that wavelength, thus indicating

an intermediate state to which the excited singlet decays prior to dissociation. The identity of this state is not yet known, however. It is also not known why the intermediate is long-lived; whether it is due to an energy barrier to dissociation or to some inefficient coupling between this intermediate state and the corresponding dissociative continua is yet to be resolved.

The excited singlet ($^1A''$) does not correlate with molecular photoproducts; it correlates with radical products in which the formyl radical is electronically excited at an energy of about $40,000\text{ cm}^{-1}$ above ground state formaldehyde (see figure 1 for an energy level diagram).²⁵ The lower triplet ($^3A''$) does correlate with ground state radical products but not with molecular products. Ab initio potential energy surface calculations indicate a non planar path for radical dissociation in both of the above states.²⁶

The ground electronic state (1A_1) correlates with molecular photoproducts, and ab initio potential energy surface calculations demonstrate an energy barrier to dissociation of about 4.5 eV ($36,300\text{ cm}^{-1}$).^{27,28} Now, since dissociation into molecular photoproducts occurs at much lower energies ($28,200\text{ cm}^{-1}$), then the apparent delay between decay of the excited singlet and photodissociation into molecular products could be understood in light of a higher energy barrier to dissociation. So, in order to verify this assumption, it is necessary to measure the appearance rates of photochemical products at different energies of excitation. An examination of the pressure dependence of those rates measured at different energies and with different foreign

Figure 1. Energy level diagram for H_2CO . The correlation between bound states and dissociation product continua are indicated by the dashed lines. The barrier heights are unknown.



XBL 788-5608

Fig. 1.

gases will certainly provide a better picture of the mechanism of formaldehyde predissociation.

In what follows is a description of the experiments carried out in this work to measure the appearance rates of photochemical products in formaldehyde. Chapter II gives a general background on the theory and experimental data available in the literature that have a bearing on this work. Chapter III describes the equipment used and the experimental procedure followed in measuring the appearance rates of molecular photoproducts. Chapter IV lists the experimental results obtained for the isotopic species: H_2CO , HDCO and D_2CO and also for some related small carbonyls such as ketene, acrolein, propynal and cyclobutanone. Chapter V describes the experiments used in an attempt to measure the appearance rates of radical products by optical detection of H-atoms. Finally, Chapter VI is a discussion of the various results obtained including suggestions for further experiments to be carried out in light of those results.

II. DYNAMICS OF PHOTOPREDISSOCIATION IN FORMALDEHYDE

Although it has been subjected to many intensive experimental and theoretical studies in recent years, the mechanism of formaldehyde predissociation is still not well understood. Since it is rather difficult to cover the wealth of literature available on the physics and chemistry of this interesting molecule, only those aspects of photochemical processes pertaining to this work will be described in this chapter.

A. SPECTROSCOPY

The near ultraviolet absorption spectrum of formaldehyde consists of a progression of well-resolved vibrational bands covering the wavelength range 360-260 nm.^{14, 30} The band is weak, typical of an $n \rightarrow \pi^*$ transition connecting the ground electronic state (1A_1) with the first excited singlet ($^1A''$). The triplet state ($^3A''$) lies about 2994 cm^{-1} below the origin of the excited singlet which is placed at 28188 cm^{-1} above the ground electronic state of H_2CO .^{30, 31} The molecule is planar in its ground state and nonplanar in the excited singlet ($^1A''$) and triplet ($^3A''$) states with the hydrogens $\sim 33^\circ$ and 37° out of the molecular plane, respectively.³⁰

Even though this absorption band shows a discrete vibrational structure, the rotational line envelopes become more diffuse with higher vibrational energy of excitation, thus indicating a possible predissociation.^{2, 32} No phosphorescence has been detected that could be related to singlet-triplet intersystem crossing thus far. There is also no evidence of phosphorescence from the triplet of H_2CO excited directly in the range 390-360 nm.³³ D_2CO , on the other hand, does

phosphoresce when excited in the same wavelength range (390-360 nm).³³ The absence of phosphorescence from the triplet ($^3A''$) of H_2CO could be attributed to the presence of a fast radiationless relaxation process which is slower or even absent in D_2CO .

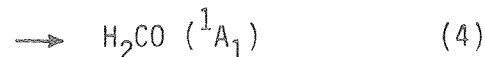
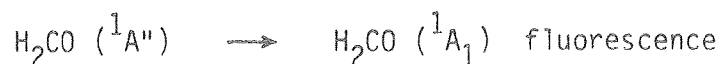
Inspection of magnetic rotation absorption spectra³⁴ and Zeeman line broadening studies³⁵ show some singlet ($^1A''$)-triplet($^3A''$) perturbations at 326 nm. This corresponds to excitation of the $2^2_4^1$ vibrational level in the $^1A''$ state in which rotational line displacements of up to 0.23 cm^{-1} have been observed.³⁴ Zeeman line displacements of up to 0.5 cm^{-1} have been found in this vibrational level ($2^2_4^1$) and the interactions were interpreted to occur through intersystem spin-rotation coupling with the triplet $1^1_2^2_4^1$ level, or through vibronic spin-orbit coupling with the triplet $1^1_2^2$ level.³⁵ There is no evidence for singlet-triplet perturbations at other energies of excitation based on these two studies.^{34,35}

The possibility of interaction with other excited states of formaldehyde is ruled out at least in the energy range of $40,000\text{ cm}^{-1}$ above the ground electronic state. The next higher excited state is the triplet state $\pi \rightarrow \pi^*$ (3A_1). Theoretical calculations place it in the energy range 5.0 to 7.2 eV.^{30,36,37} Beyond that the electronic spectrum of formaldehyde shows a progression of Rydberg states starting with the $(n \rightarrow 3S)$ 3B_2 at 6.96 eV or $\sim 1780\text{ nm}$ in the vacuum UV.^{30,36,37} The singlet $\pi \rightarrow \pi^*$ state (1A_1) position is still unresolved and calculations indicate it may be hidden with the progression of Rydberg bands at energies of 8.0 eV or above.^{30,38}

Figure 2 depicts an energy level diagram of the lower excited states of H₂CO. On the right side of the figure is a schematic of the energies of possible photochemical products relative to the ground state of H₂CO. For a complete review of formaldehyde spectroscopy, the reader is referred to reference 30.

B. DECAY OF THE EXCITED SINGLET (¹A''):

The principal modes of decay of the singlet state (¹A'') excited in the wavelength range 355-260 nm are illustrated by the following set of equations:

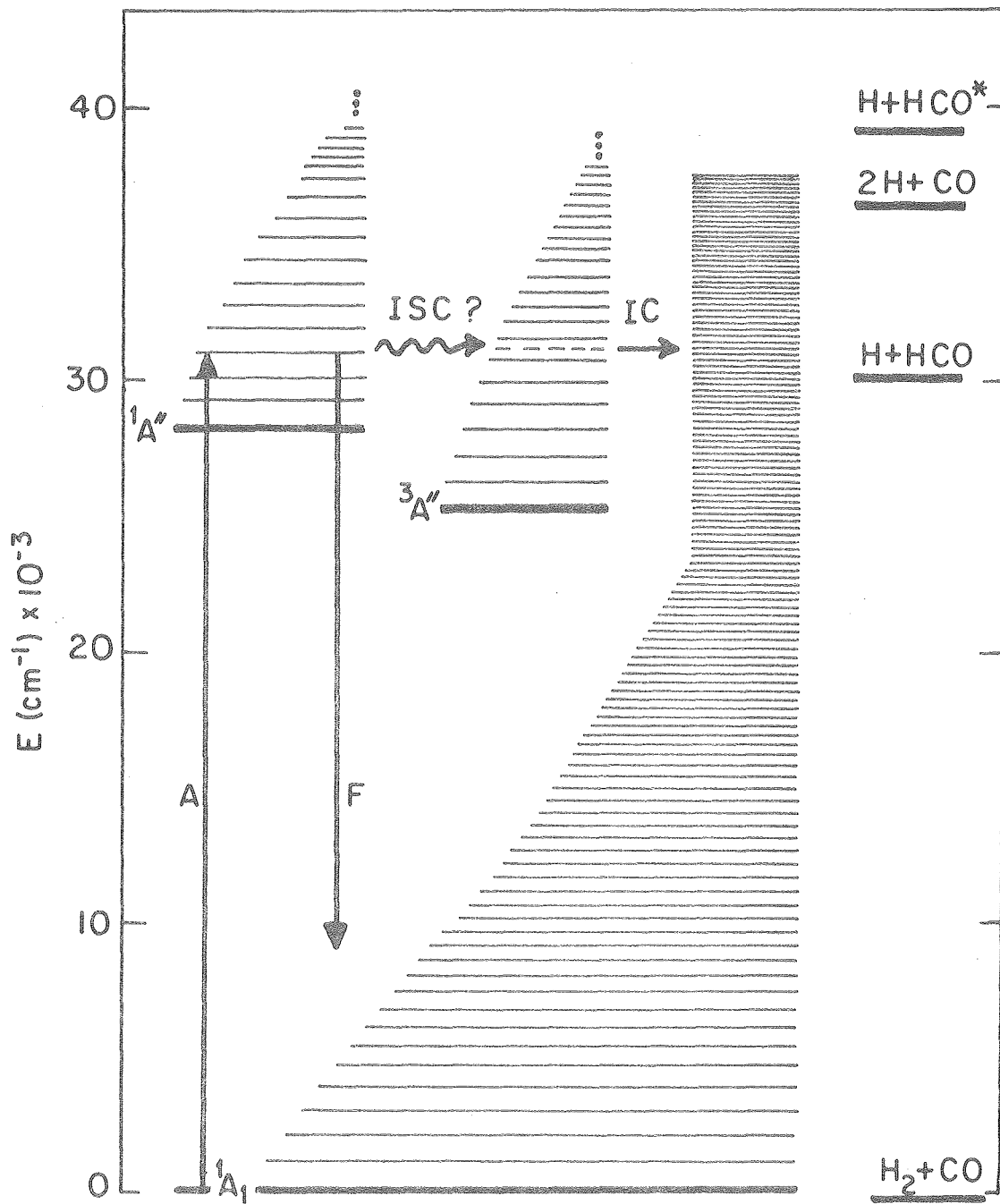


Equations (1) and (2) indicate the two primary photodissociation processes occurring at wavelengths above 280 nm, and eqn. (3) refers to a radical dissociation channel which becomes energetically accessible below 274 nm.¹⁴ Equation (4) indicates internal conversion or collisional quenching down to the ground electronic state. Relaxation within the individual rovibronic levels of the excited singlet is ignored here, and will be referred to when necessary. The decay rates of the excited singlet and the appearance rates of photoproducts will be discussed below.

1. Fluorescence Lifetimes and Decay Rates

The decay rates of single vibronic levels of the excited singlet demonstrate a rather large energy dependence, becoming shorter with

Figure 2. Energy level diagram of H_2CO showing the electronic states within $50,000 \text{ cm}^{-1}$ above the ground electronic state. The symbols A and F refer to absorption and fluorescence, respectively. ISC designates possible intersystem crossing and IC refers to internal conversion. On the right hand side of the figure are shown the energy levels of photochemical products relative to the ground state of H_2CO .



XBL 788-5609

Fig. 2.

higher excitation energy.^{1,2,5} They also exhibit a deuterium isotope effect with decay rates in the order: $\text{H}_2\text{CO} > \text{HDCO} > \text{D}_2\text{CO}$.^{1,2} The Stern-Volmer plots of inverse lifetimes versus pressure show the following interesting features:

- (i) For H_2CO in which the 4^0 vibrational level is excited at pressures in the range 2×10^{-4} to 0.1 torr, the zero pressure lifetimes as well as the quenching rates depend on the particular rotational quantum numbers (J' and K') excited.¹⁵ For example, the zero pressure lifetimes vary between $4.17 \mu\text{s}$ for the $rQ_0(4)$, $J' = 4$, $K' = 1$ rotational level to values in the range 0.07 to $0.7 \mu\text{s}$ for many higher rotational levels.^{15,39} There is no apparent systematic correlation between those lifetimes and the particular rotational quantum number excited, however. At the sufficiently low pressure range mentioned above, and for most of the rotational levels excited, the decay curves of the 4^0 and 4^1 vibronic levels were found to be single exponentials when single rotational lines were excited.³⁹ The zero pressure decay often occurs more than 20 times faster than the calculated radiative lifetimes.^{15,40,41} Below pressures of 0.020 torr, the Stern-Volmer plots give quenching rates of 2.2 to $6.5 \times 10^{-9} \text{ cm}^3 \text{ molecule}^{-1} \text{ sec}^{-1}$. At pressures above 1 torr, a quenching rate constant of only $2.2 \times 10^{-11} \text{ cm}^3 \text{ molecule}^{-1} \text{ sec}^{-1}$ is observed and thus the Stern-Volmer curve appears very much curved. At pressures above 0.1 torr, the fluorescence decay curves are single exponentials, independent of J' and K' ,

with some modification from $4^0 \leftrightarrow 4^1$ energy transfer.¹⁵ The energy transfer rate of $4^1 \leftrightarrow 4^0$ has been measured as $6.9 \times 10^{-10} \text{ cm}^3 \text{ molecule}^{-1} \text{ sec}^{-1}$,⁴² which corresponds to $\sim 0.45 \mu\text{sec}^{-1}$ at 0.020 torr; the corresponding quenching rate is $6.5 \times 10^{-9} \text{ cm}^3 \text{ molecule}^{-1} \text{ sec}^{-1}$ or $\sim 4 \mu\text{sec}^{-1} \text{ torr}^{-1}$.¹⁵ This shows that, at low pressures, vibrational energy transfer is less important in quenching H_2CO fluorescence.

It should also be noted here that the fluorescence lifetimes decrease by almost two orders of magnitude when the energy of excitation is varied between 353 nm (4^1 level) and 300 nm ($2^2 5^1$ level) in H_2CO and for pressures above 0.1 torr.^{1,17} There is no low pressure data for the lower wavelengths to compare with those obtained for the 4^0 and 4^1 level.¹⁵ At wavelengths below 300 nm, the rotational structure of the rovibronic bands becomes very diffuse and the lifetimes are a few p sec.²

(ii) For D_2CO , the decay curves of both the 4^0 and 4^1 levels were found to be single exponential over the pressure range 4×10^{-5} to 4 torr.¹⁵ The zero pressure lifetimes obtained were $7.8 \pm 0.7 \mu\text{s}$ for the 4^0 level, and $6.0 \pm 0.4 \mu\text{s}$ for the 4^1 level and are presumed to be the radiative lifetimes.¹⁵ The rate of energy transfer ($4^1 \rightarrow 4^0$) was measured as $(9.6 \pm 0.4) \times 10^{-10} \text{ cm}^3 \text{ molecule}^{-1} \text{ sec}^{-1}$, a value higher than that of H_2CO possibly due to the lower energy gap in D_2CO .

The Stern-Volmer plots show some negative curvature at low pressures (below 10 mtorr). The curvature is much less

dramatic than what is observed in H₂CO for the same vibronic levels excited.¹⁵ The low pressure decay rates were estimated roughly as $(9 \pm 6) \times 10^{-10} \text{ cm}^3 \text{ molecule}^{-1} \text{ sec}^{-1}$ and $(3 \pm 2) \times 10^{-10} \text{ cm}^3 \text{ molecule}^{-1} \text{ sec}^{-1}$ for the 4⁰ and 4¹ levels, respectively.¹⁵ The high pressure portion of the Stern-Volmer plot gives a decay rate of $(2.96 \pm 0.19) \times 10^{-11} \text{ cm}^3 \text{ molecule}^{-1} \text{ sec}^{-1}$ for either level and over the pressure range 0.1 to 4 torr. This is only about 0.1 times the gas kinetic rate.¹⁵

The variation of fluorescence lifetimes with vibrational excitation at pressures above 0.1 torr follows a similar trend to that of H₂CO. The lifetime at 308 nm (2³4³ level) is only 53 ns.¹ Below 290 nm, the lifetimes decrease substantially to a few psec with values almost twice those of H₂CO at the same vibronic level excited.²

- (iii) For HDCO, there are no low pressure data on the fluorescence lifetimes to compare with those of H₂CO and D₂CO presented above. Lifetimes measured at pressures above 0.1 torr vary from 0.3 μs for the 4¹ level at 353 nm to about 8 nsec for the 2³4³ level at 304 nm.¹ At higher energies, lower wavelengths, the lifetimes decrease more so than the corresponding values for H₂CO or D₂CO and do not extrapolate to those at higher wavelengths.²

The above data on fluorescence lifetimes and decay rates clearly indicate a fast decay of the excited singlet 4¹ and 4⁰ levels of H₂CO at low pressures. A collision-induced

decay rate more than 20 times the gas kinetic rate looks rather intriguing for such a small polyatomic molecule. D_2CO appears to decay much more slowly at low pressure with a zero pressure decay rate probably equivalent to that of the radiative lifetime. HDCO lifetimes are probably intermediate between H_2CO and D_2CO as seen from the high pressure data. The anomalous behavior of HDCO lifetimes at high energy of excitation is also peculiar.

2. Appearance Rates of Photochemical Products

In his recent experiments on the energy distribution of molecular photoproducts in formaldehyde, P. L. Houston measured the rate of appearance of CO as a function of gas pressure.²⁵ At 337.1 nm wavelength of excitation, and in the pressure range 0.1 to 5.0 torr of H_2CO , the rate was measured as $1.65 \pm 0.12 \mu\text{sec}^{-1} \text{ torr}^{-1}$. At 1.0 torr of H_2CO , the lifetime for molecular photodissociation would therefore be $\sim 0.6 \mu\text{sec}$, much longer than the fluorescence lifetime of the excited singlet state measured as 29 nsec at 339 nm (1.0 torr) and ~ 11 nsec at 331 nm (2.0 torr).¹⁷ This finding led to the conclusion that the excited singlet does not decay into molecular photoproducts directly, rather, it goes into a long-lived intermediate, $H_2CO(I_1)$, which subsequently dissociates upon collisions into molecular products:²⁵



The CO appearance rate was also measured for D_2CO at 337.1 nm and found to be $0.96 \pm 0.07 \mu\text{sec}^{-1} \text{ torr}^{-1}$, which is a little slower

than that of H_2CO , possibly due to a deuterium isotope effect.²⁵ The effect of nitric oxide on the CO appearance rate was measured for 0.5 torr H_2CO and 0-2 torr of NO with the rate of appearance of CO due to NO gas given as $1.9 \pm 0.5 \mu\text{sec}^{-1} \text{ torr}^{-1}$. The effect of Ar gas was also studied for 1.5 torr of D_2CO and Ar pressure varying over the range 0-15 torr, the rate of CO appearance due to Ar was measured as $0.10 \pm 0.01 \mu\text{sec}^{-1} \text{ torr}^{-1}$.²⁵

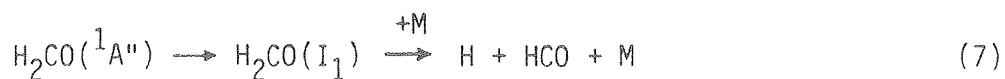
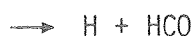
The nature of the intermediate is still not resolved, however, and the variation of the photoproduct appearance rates with energy of excitation needs to be examined. This is necessary from the standpoint of locating possible energy barriers for dissociation, and also correlating the photoproduct appearance rates with the corresponding decay rates of the individual vibronic levels excited.

C. QUANTUM YIELDS AND BRANCHING RATIOS

1. Pure H_2CO

The molecular photoproduct quantum yields increase from 0.68 at the band origin (353 nm) up to about 0.9 near 335 nm where it begins to drop as a new dissociation channel for radical products begins to compete.²⁰ The onset for radical dissociation has been placed between 339.2 and 329.8 nm (84.2 and 86.6 kcal/mole),²⁰ which is well within the experimental error limit of the thermodynamic C-H bond energy of 86.9 ± 2 kcal/mole.⁴³ The measured radical product quantum yields vary from almost zero at 339 nm to ~0.5 at 299.1 nm.²⁰ Horowitz, et al.⁴⁴ reported radical yields of 0.68 at 313 nm with molecular yield of 0.32.

It should be noted however that the total photochemical quantum yield attains unity beyond the threshold for radical dissociation, and the H₂ and CO quantum yields are equivalent.²⁰ This suggests a photodissociation mechanism represented by the following equations:

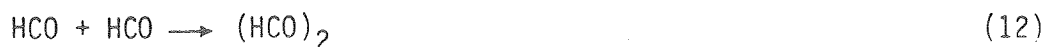


Here I₁ and I₂ indicate possible intermediates formed upon decay of the excited singlet ({}¹A'') prior to dissociation. Reactions indicated in eq. (7) are highly speculative at the present stage since it is not clear whether radical dissociation occurs on the same time scale of decay of the {}¹A'' state, or via intermediates I₁ or I₂. The mechanism however is compatible with the equal H₂ and CO quantum yields measured over the energy range 335 to 299.1 nm,²⁰ as is seen in reactions (6) through (9) above. Two other reactions are also compatible with the above mechanism, namely



Reaction (10) is not expected to compete with reaction (8), however, due to the much lower concentration of HCO radicals compared with H_2CO . For example, the rate constant for reaction (8) has been measured as $5.4 \times 10^{-14} \text{ cm}^3 \text{ molecule}^{-1} \text{ sec}^{-1}$.⁴⁵ Reaction (10), though has a higher rate constant ($5 \times 10^{-10} \text{ cm}^3 \text{ molecule}^{-1} \text{ sec}^{-1}$),^{46,47} occurs to a lower extent than reaction (10) since the H and HCO concentrations are very low under the photolysis conditions of quantum yield experiments. (The radical concentration is typically $8 \times 10^{12} \text{ cm}^{-3}$ thus making the contribution of reaction (10) about one fifth that of reaction (8)).

Reaction (11) may occur to some extent, and the relative branching ratio has been estimated to be >10 in favor of reaction 9.²⁰ A reaction leading to the formation of glyoxal (12) below has been estimated to be negligible since it would lead to unequal H_2 and CO yields



contrary to experimental results.²⁰ The following reaction (13) may occur but has no effect on the relative H_2/CO ratio. It could be critical though in case an isotopic selectivity is desirable since it leads to scrambling of selectively produced H_2CO .



2. Pure D₂CO

The energy dependence of product quantum yields is qualitatively the same as that of H₂CO except for much lower molecular photoproduct yields at the origin of the excited singlet. This is probably due to higher non-reactive quenching in D₂CO. The quantum yield of molecular products is about 0.3 at 340 nm and increases to a total photochemical yield of unity beyond the threshold for radical dissociation.²⁰ The energy threshold for radical dissociation has been placed between 326.0 and 319.7 nm (87.6 and 89.4 kcal/mole), a little higher than that of H₂CO which is in agreement with the C-D dissociation energy being higher than C-H by ~2.1 kcal/mole.²⁰

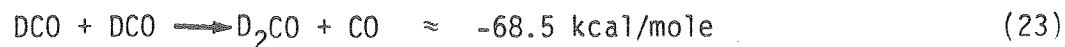
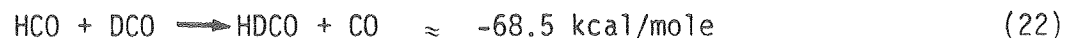
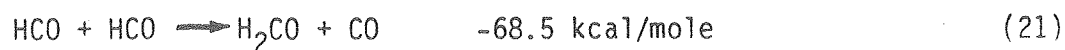
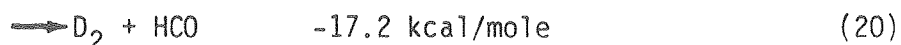
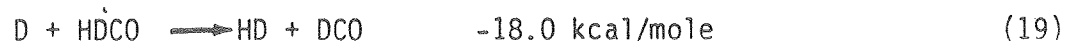
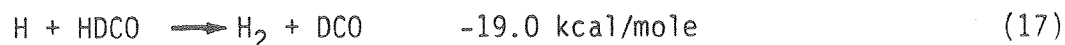
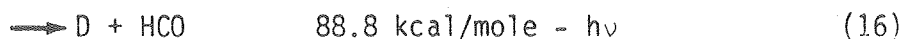
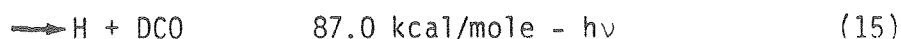
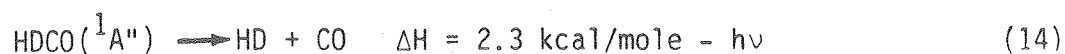
The radical quantum yields of D₂CO appear to be equal to those of H₂CO in the energy range 326-300 nm. The relative H₂/CO yield is unity thus suggesting the same mechanism for photodissociation similar to that of H₂CO described above.

3. Pure HDCO

There are no absolute photochemical quantum yields available for HDCO. The relative radical to total quantum yields were however measured by J. B. Marling in the wavelength range 353 to 300 nm.⁶ Those were obtained from the (H₂ + D₂)/(H₂ + HD + D₂) ratio since both H₂ and D₂ occur as a result of secondary radical reactions as will be shown below. The variation of the above ratio with excitation energy exhibits a rapid increase between 332 and 320 nm (86.1 and 89.3 kcal/mole). This corresponds to the energy threshold for radical dissociation in HDCO where the C-H bond energy is ~0.4 kcal/mole higher

than in H_2CO due to the zero point energy differences.^{6,20} Below 320 nm the ratio attains a constant value of ~ 0.5 down to 300 nm.⁶

Marling reported an H_2/D_2 branching ratio of 5.3 which remained constant over the wavelength range 326-304 nm.⁶ This clearly shows a single secondary radical reaction mechanism which remains unchanged regardless of the energy states of H and DCO radicals produced. The constancy of H_2/D_2 and radical/total photochemical quantum yield ratio is consistent with a mechanism which is qualitatively the same as that in H_2CO . This is shown in eqs. (14) through (23) where the enthalpy H_{298}^0 is listed in each step for the sake of a qualitative comparison:



Reaction (15) is more exothermic than (16) and thus has more reaction channels available; reaction (17) would occur with a higher rate than (18) for the same reason and is thus expected to be faster than (18), (19) and (20). (Any effect of tunneling goes in the same

direction.) These all lead to an H_2/D_2 ratio greater than one. That the H_2/D_2 branching ratio stays constant regardless of excitation energy indicates that reactions (17)-(19) are probably slow compared to energy relaxation and that the ratio of (15) to (16) must be roughly energy independent.

D. EFFECT OF FOREIGN GASES ON BRANCHING RATIOS

1. Nitric Oxide (NO)

At 337.1 nm wavelength of excitation, the contribution of NO to the rate of appearance of molecular photoproducts in H_2CO was measured as $1.9 \pm 0.5 \mu\text{sec}^{-1} \text{ torr}^{-1}$.²⁵ This is not much different from $1.65 \pm 0.12 \mu\text{sec}^{-1} \text{ torr}^{-1}$ obtained for pure H_2CO within the experimental error limits of the measurements.²⁵ It was found however that NO increases the relative population of CO ($\nu = 1$) produced as the excitation energy was increased. For example, the CO ($\nu = 1$) population was found to increase by more than a factor of 3 at 305.5 nm, and by about 60% of that at 326.0 nm with very little effect at 337.1 nm over that of pure formaldehyde (H_2CO).²⁵ This led to some speculation as to whether NO may influence the vibrational distribution of molecular products through collisional interaction with the long-lived intermediate $H_2CO(I_1)$.²⁴

In two recent papers, Reilly, et al.⁴⁷ and Horowitz, et al.⁴⁸ suggested that the increase of vibrationally excited CO yield in the presence of NO may well be explained by the secondary reaction between NO and HCO which is exothermic as shown in reaction (24):



where the dagger on CO indicates vibrational excitation. The rate of the above reaction has been measured as $K_{24} = (1.4 \pm 0.2) \times 10^{-11} \text{ cm}^3 \text{ molecule}^{-1} \text{ sec}^{-1}$.⁴⁷

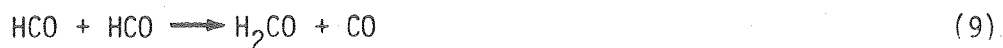
The effect of NO on the branching ratio for molecular photoproduct yields has been determined, and found to increase the relative CO to H₂ quantum yields, due to the following secondary reactions with H and HCO radicals,⁴⁷ namely:



Reaction (25) does suppress reaction (8) which occurs between H and H₂CO:



at sufficiently high NO pressures (ca. 50 torr NO/5 torr H₂CO) thus reducing the relative H₂ yields. Furthermore, reaction (24) dominates reaction (9)



thus producing more CO yields with the net result of a decrease in the relative H₂/CO ratio. This method of adding NO to H₂CO has been used to measure the radical quantum yields by equating them to the difference between CO and H₂ quantum yields for each wavelength used.^{20,21} (The

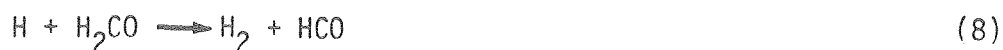
rate of reaction (9) was recently measured by Reilly, et al.⁴⁷ and found to be approximately $10^{(-10.2 \pm 0.5)} \text{ cm}^3 \text{ molecule}^{-1} \text{ sec}^{-1}$).

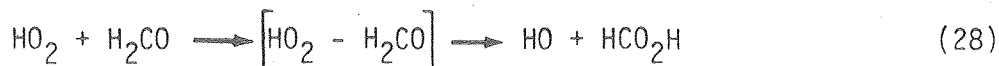
2. Oxygen

Oxygen appears to play an important role in a series of radical chain reactions following formaldehyde photodissociation which differ significantly from that of NO. P. L. Houston²⁵ reported an increase in the product yield of CO ($v = 1$) in $\text{O}_2 + \text{H}_2\text{CO}$ mixtures photolyzed at 305.5 nm over pure H_2CO samples. This effect was less than what was observed with $\text{NO} + \text{H}_2\text{CO}$ mixtures under same conditions, but oxygen led to higher CO ($v = 0$) quantum yields than NO, possibly due to the less exothermicity of $\text{HCO} + \text{O}_2$ reaction compared with $\text{HCO} + \text{NO}$.

Jack Marling⁶ observed higher $\text{H}_2 + \text{D}_2$ yields in $\text{O}_2 + \text{HDCO}$ mixtures photolyzed at 314 nm than in pure HDCO. The relative H_2/D_2 ratio was also found to increase in the presence of oxygen (69 compared with only 5.3 in oxygen-free samples of HDCO). Furthermore, a negative, though less dramatic, effect on $\text{C}^{13}/\text{C}^{12}$ isotope enrichment in $\text{H}_2\text{C}^{13}\text{O} + \text{H}_2\text{C}^{12}\text{O}$ mixtures was observed where the presence of oxygen led to scrambling of selectively excited products.⁶

Recent studies carried out by Horowitz, et al.⁴⁸ on the photolysis of $\text{O}_2 + \text{H}_2\text{CO}$ mixtures at 313 nm, and the subsequent measurement of photoproduct quantum yields, suggest a mechanism in which oxygen induces a chain reaction the result of which is production of H_2 and CO quantum yields in excess of 4; mentioned briefly:





Here, it is assumed that at sufficiently high oxygen pressure (ca. 1 torr O_2 /8 torr H_2CO) reaction (27) competes with (8) leading together with reaction (26) to the formation of HO_2 radical. HO_2 subsequently reacts with H_2CO , reaction (28), to produce the reactive OH radical which might produce HCO^+ and/or HCO via reactions (29) and (30), respectively. In the above mechanism, HCO^+ is proposed to dissociate into $\text{H} + \text{CO}$ via reaction (31) thus producing more CO and H, or else, it may react with O_2 as in the case of HCO to produce more HO_2 and CO (reaction (27)). It should be noted that reactions (31) and (32) produce more H radicals thus increasing H_2 yields via reaction 8. This probably explains the higher $\text{H}_2 + \text{D}_2$ yields observed by Jack Marling⁶ in $\text{O}_2 + \text{HDCO}$ mixtures mentioned before. The large increase in H_2/D_2 branching ratio could then be accounted for by the thermodynamically more favorable reactions that lead to H-atom abstraction over D-atom abstraction from HDCO.

3. Argon and Nitrogen

A study of the rate of appearance of CO in mixtures of 1.5 torr D₂CO and 0-15 torr Ar gave a rate of CO appearance of $0.10 \pm 0.01 \mu\text{sec}^{-1} \text{ torr}^{-1}$ of Ar at 337.1 nm.²⁵ In the same study it was found that the CO ($v = 0$) absorption decreases by ~4% per torr of Ar added. In the above range of pressure, about 1.5% decrease in the CO ($v = 0$) yield was attributed to pressure broadening of the CO absorption line, and the balance (2.5%) to collisional quenching of the D₂CO (¹A") state by Ar possibly to the ground state. No similar study on Ar + H₂CO mixtures was attempted, then, but it was found that N₂ gas decreases the CO ($v = 1$) quantum yields in N₂ + H₂CO mixtures irradiated at 305.5 nm.²⁵ This apparent decrease was accounted for entirely by the pressure broadening of the CO ($v = 1$) absorption line by N₂ gas.

One perhaps should mention here that pressure broadening of formaldehyde absorption lines in the ultraviolet at the pressures used is too small to affect CO quantum yields. For example, the effect of Ar on pressure broadening of H₂CO absorption lines was measured for the rR ($J'' = 11, K'' = 7$) line at 3390 Å (29586.77 cm⁻¹) and also for the pP ($J'' = 11, K'' = 5$) line at 3430 Å (29008.99 cm⁻¹) and found to be only $9.2 \times 10^{-21} \text{ cm}^{-1}/\text{atom cm}^{-3}$ of Ar.⁴⁹ This corresponds to a broadening of $\sim 3.0 \times 10^{-4} \text{ cm}^{-1} \text{ torr}^{-1}$ of Ar which is well within the laser bandwidth used for excitation of formaldehyde + Ar mixtures.

E. PREDISSOCIATION MECHANISM

In exploring the various possibilities involved in the photodissociation mechanism of formaldehyde, an attempt is made here to discuss the results of recent potential energy surface calculations carried out by Hayes, Jaffe and Morokuma for both primary dissociation processes.²⁶⁻²⁸ Also, theoretical calculations on the rearrangement of carbonyl compounds to oxacarbenes, which were conducted by Altmann, et al.⁵⁰ and also by Lucchese and Schaefer,⁵¹ will be invoked in light of the yet unresolved but experimentally suggested long-lived intermediate.²⁵

1. Potential Energy Surfaces

Ab initio calculations of the ground (1A_1), excited singlet ($^1A''$), and the excited triplet ($^3A''$) states of H_2CO leading to either molecular ($H_2 + CO$) or radical ($H + HCO$) products indicate the following:^{25,27,28}

- (i) The planar asymmetric potential hypersurface of the ground state (C_s') is the only possible path leading to molecular products within $\sim 40,000 \text{ cm}^{-1}$ of excitation energy.²⁶

A non-planar asymmetric path (C_s) was found to have a higher energy barrier of $\sim 54,000 \text{ cm}^{-1}$, well beyond the dissociation energy experimentally verified to be in the vicinity of $\sim 28,000 \text{ cm}^{-1}$.^{14,25,27} The rather large asymmetry of the path suggests some rotational excitation of products H_2 and CO .²⁷ Also, since the H-H and CO bond distances near the saddle point (1.32 Å and 1.22 Å, respectively) are obviously either more close to the H_2CO values

(1.89, 1.21Å, respectively) or higher than those of the free molecules (0.74Å and 1.13Å, respectively), the product molecules were presumed to end up with high vibrational excitation.²⁷ The above conclusion was also based on the fact that the reaction itself is almost thermoneutral ($\Delta H \approx -140 \text{ cm}^{-1}$), and since no electronically excited products are accessible within the excitation energies used ($<40,000 \text{ cm}^{-1}$), the excitation energy would have to be deposited into the internal as well as the thermal translational motions of the molecular products. The energy barrier to dissociation has also been calculated to be in the range (4.3-4.5 eV) or $34,688\text{-}36,320 \text{ cm}^{-1}$.^{27,28}

- (ii) The excited singlet ($^1A''$), in view of the fact that it only correlates with electronically excited radical HCO products corresponding to $\sim 40,000 \text{ cm}^{-1}$ of excitation energy, is ruled out as the dissociating electronic state.^{26,27} The relatively very fast decay of this state compared with the much slower appearance of molecular photoproducts coupled with the lower dissociation energy threshold of $\sim 28,000 \text{ cm}^{-1}$ lend experimental credence to the above conclusions.^{1,14,24} In the case of dissociation to radical products (H + excited HCO), the excited singlet potential surface was found to be geometrically optimized in favor of non-planar dissociation in which the H-atom is ejected almost perpendicular to the H_2CO molecular plane.²⁶

(iii) The excited triplet ($^3A''$), which of course does not correlate with molecular photoproducts, also has a non-planar path towards radical dissociation into ground electronic state $H + HCO$.²⁶ The energy barrier of 4.79 eV ($38,641 \text{ cm}^{-1}$) is considered an overestimate due to the minimal basis set used in the calculation. It should be noted that the experimental energy threshold for radical dissociation is in the vicinity of $30,000 \text{ cm}^{-1}$.²⁰

It should be emphasized at this point that the above theoretical predictions, being helpful as they are, do not explain some of the experimental data obtained on formaldehyde thus far. A case in point is the discrepancy between the predicted high vibrational excitation of product molecules H_2 and CO ,²⁷ and the relatively low vibrational excitation of CO measured by P. L. Houston.²⁵ Here it was found that no more than 5% of the available energy ends up in vibrational excitation of CO molecules. Although no experimental data is available on the vibrational excitation of H_2 product molecules, an analogy could perhaps be made with the low vibrational excitation of HF molecules (<10% of available energy) produced in the photolysis of $HFCO$.⁵² If the above analogy is justified, then this raises the question as to the loss mechanism of the excess energy which may be as much as 80% of the excitation energy. It remains to be verified whether the balance will end up in rotational and/or translational energy of products

H₂ and CO. It is fair to say however that the above theoretical calculations are approximate as indicated by the authors,²⁶⁻²⁸ and the energy barriers could actually be much lower than predicted. The authors speculate on the possibility of energy pooling between two excited molecules to produce one H₂CO (¹A₁) molecule with energy in excess of the energy barrier.²⁸ It may be possible that the excess energy which does not end up as vibrational excitation of product molecules is lost as translational energy in product molecules plus the collision partner. This latter point is understandable in view of the pressure dependence of molecular product appearance rates measured in the pressure range 0.1 to 5 torr H₂CO and D₂CO.²⁵

The relatively fast decay rates of the excited singlet state of H₂CO is also intriguing. Formaldehyde is a small polyatomic with a very low density of quantum states near the origin of the excited singlet (~10/cm⁻¹ for the ground state and ~0.02/cm⁻¹ for the triplet) to serve as irreversible dissipating channels for the excited singlet and therefore reduce its lifetime.

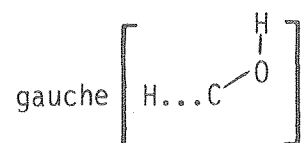
Finally, to add to the above speculation, it is very likely that H₂CO, upon excitation, acquires enough energy to undergo isomerization to hydroxymethylene which may very well be the long-lived intermediate suggested by Houston's experimental findings.²⁵

2. Geometrical Rearrangement to Hydroxymethylene

Detailed ab initio SCF molecular orbital calculations have recently been carried out by Altman, et al.⁵⁰ on the geometrical isomerism

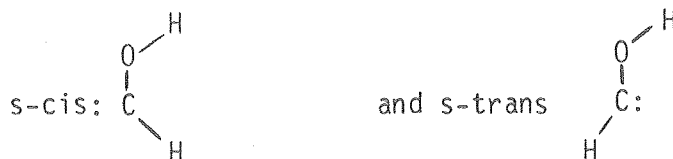
of H_2CO and hydroxymethylene. The results of geometry optimization in both the excited singlet and triplet states of H_2CO and the isomeric hydroxymethylene (or oxacarbene) indicate the following:

- (i) The triplet hydroxymethylene has only one stable form:



which was predicted to be about 48 kcal/mole above ground state H_2CO .

- (ii) The singlet however has two stable forms which are planar, that is, the



forms with energies of ~54 and 47 kcal/mole relative to the ground state of H_2CO .

The energy states of the three possible isomers of hydroxymethylene mentioned above are certainly well below the vertical excitation energy of H_2CO , thus making either one as a possible intermediate. The same calculation however predicted the triplet state of H_2CO to be only ~36 kcal/mole relative to the ground state. This is much less than the experimentally known value of ~72 kcal/mole thus shadowing the predictions with some uncertainty.

H. F. Schaefer and co-workers have recently carried out a follow up to the above calculation where they incorporated electron correlation using the configuration interaction methods into the calculation.⁵¹

The results obtained also showed the three isomers to be much lower in energy than the excited singlet of H_2CO . The s-trans configuration appears to be the most favorable among the three for two considerations: first, it has the lowest energy of ~ 29 kcal per mole below the origin of the excited singlet, and second because it is more favored for the least motion required in isomerism. In this calculation, the energy of the triplet state of H_2CO was predicted correctly thus giving more credence to the predictions. So it seems possible the migration of H-atom towards the oxygen atom in H_2CO occurs to form the corresponding isomer. If this process does occur at all, and if it could be proved to be as fast as the decay of the excited singlet, then hydroxymethylene could be the long-lived intermediate. The lower molecular quantum yields and slower appearance rates of CO near the singlet origin of D_2CO compared to H_2CO may then be understood in terms of a higher energy barrier for migration of the heavier deuterium atom vis a vis hydrogen.

III. EXPERIMENTAL

A. GENERAL DESCRIPTION

Appearance rates of photochemical products were obtained from their measured fluorescence intensity as a function of time. The fluorescing species were produced as a result of photolysis of a gas sample with ultraviolet laser radiation obtained from a Nd:YAG laser through a system of nonlinear crystals. The UV laser beam was directed through a fluorescence cell containing the gas sample, and IR fluorescence was detected at right angles by focusing it into an IR photoconductive detector equipped with the appropriate interference filters. The electrical signal was then amplified, filtered and fed into a digital system for processing, display and recording.

B. THE Nd:YAG LASER

This is a high power Q-switched oscillator-power amplifier system (Raytheon model SS-404) capable of delivering up to 20 MW peak power in short (~15 nsec) pluses at 1064.1 nm. The laser output beam is in the TEM₀₀ mode with a beam diameter of ~3 mm and divergence less than 1 mrad. The linewidth is roughly 1 cm⁻¹ (FWHM) and can be reduced to ~0.1 cm⁻¹ through an easily installed intracavity etalon within the master oscillator.

The laser consists of a master oscillator equipped with a Pockels cell for Q-switching, and three amplifier stages. The laser rods (0.7% Nd³⁺ dopant) were all optically pumped with flashlamps situated in elliptical cavities, and all cooled with circulating deionized water. In order to minimize undesirable beam reflections within the oscillator-amplifier system, the laser rods and all other optical

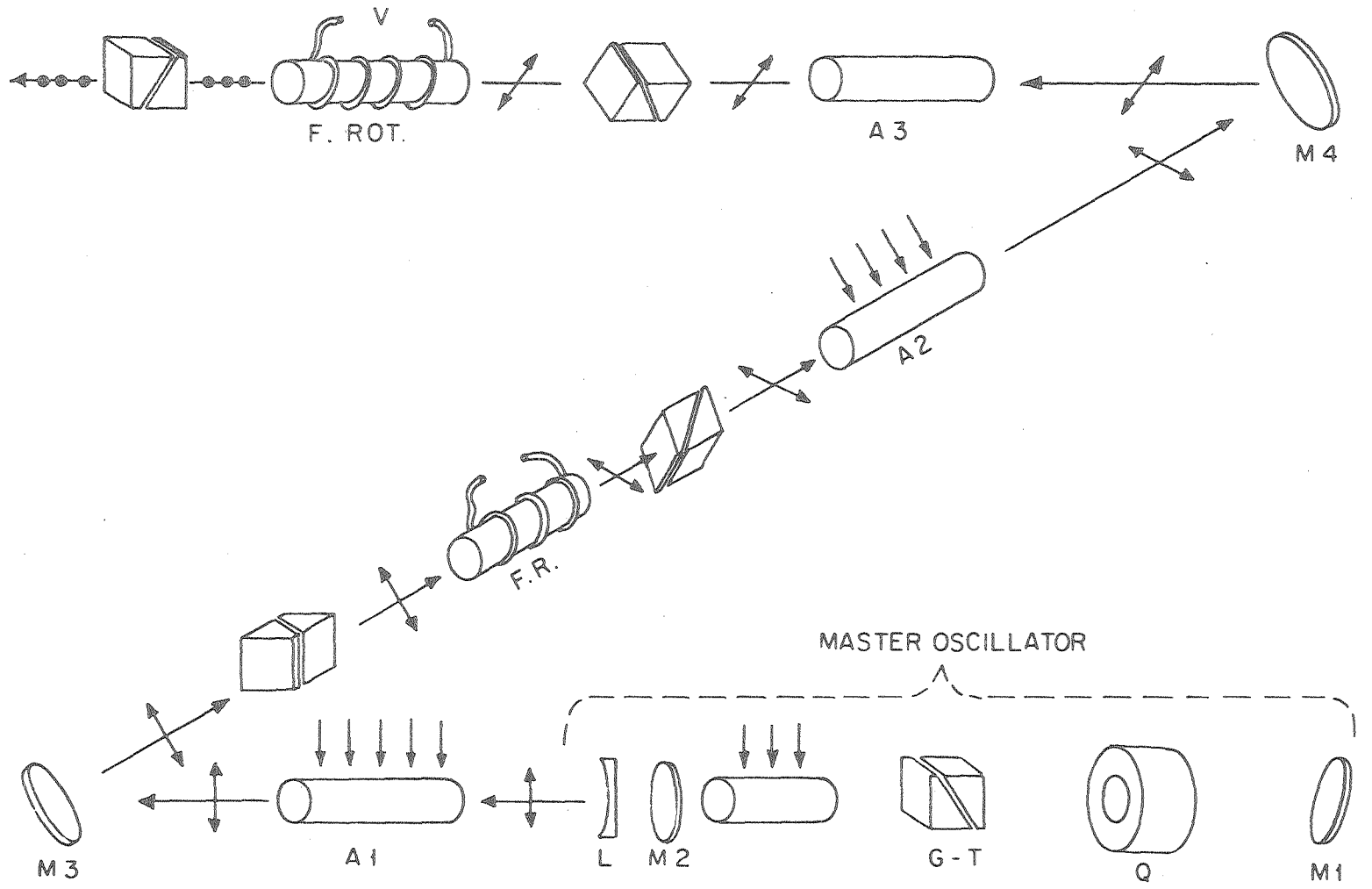
components aside from the reflective mirrors were cut at a wedged angle and coated with antireflection coatings. Furthermore, a system of two Faraday isolators were placed within the power amplifier system in order to prevent the output beam from travelling in the opposite direction thus possibly damaging the laser optics through undesirable amplification. Figure 3 shows a schematic layout of the various optical elements enclosed within the laser head. Since the energy level diagram and oscillation parameters of the Nd:YAG laser are well covered in the literature,⁵³ the remainder of this section will only point some special design features implemented in this system and the optics used to alter the polarization direction of the output beam.

1. Faraday Isolators

This is a system designed to prevent a beam of plane polarized light from travelling in the opposite direction through rotation of the polarization plane by 90° round trip. It consists of two cross-polarized prisms and a magneto-optic crystal situated in between whose function is to rotate the plane of polarization by 45° each time the beam passes through.⁵⁴ A magnetic field applied across the crystal optic axis induces a magneto-optic birefringence, that is, a phase shift between the right and left-handed circularly polarized components of the incident beam. The magnitude of this phase shift (ϕ), as manifested by a rotation of the beam polarization vector, is proportional to the applied magnetic field (B) and also to the length of the crystal (d) according to:

$$\phi = vBd \quad (33)$$

Figure 3. Schematic of the optical components within the laser head of the Nd:YAG laser. M_1 , M_3 and M_4 are reflective mirrors with 100% reflectivity at 1.06μ . M_2 has 50% transmission at the same wavelength. F. R. stands for Faraday rotator, C for calcite prism, A_1 through A_3 are for amplifiers, and arrows along the optic axis indicate the polarization vector of the laser beam.



XBL 788-5610

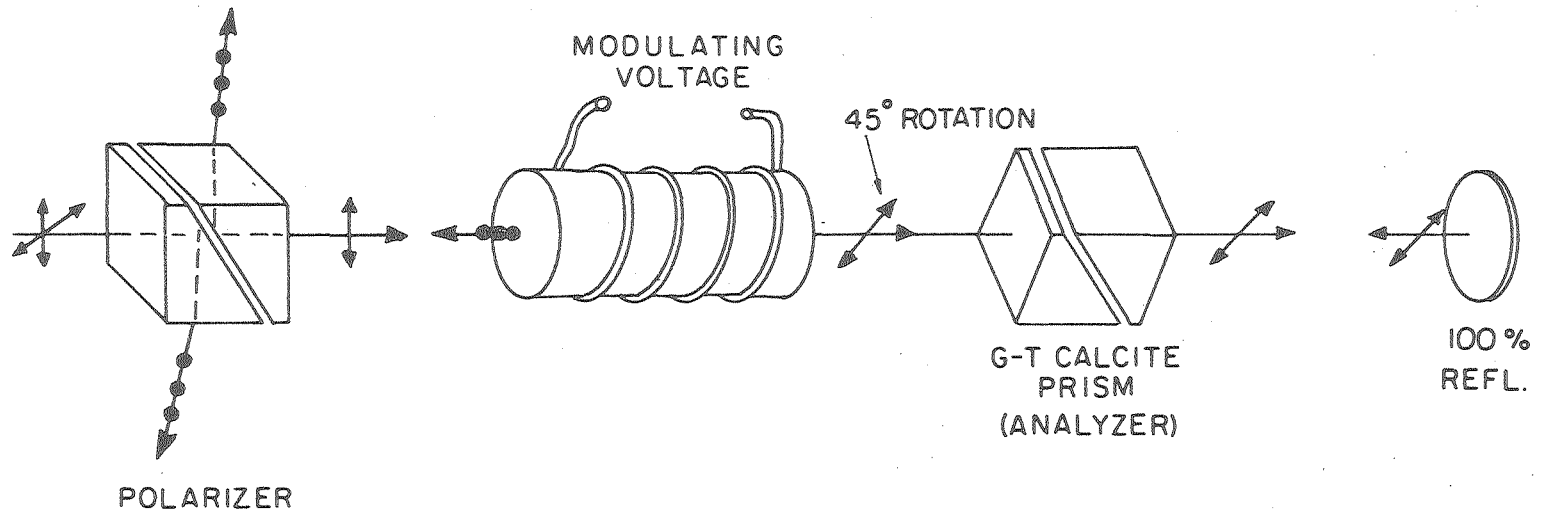
Fig. 3.



where v is a proportionality factor called the Verdet constant, B is given in units of gauss, d in cm and ϕ is in units of minutes of arc. For the particular magneto-optic material used here (Hoya FR-5, 15 x 54 mm glass), the Verdet constant at 1064.1 nm is $v = -0.0826$ min of arc cm^{-1} gauss^{-1} with the negative sign indicating the direction of rotation relative to that of the applied magnetic field, $d = 5.4$ cm thus the magnetic field required to rotate the plane of polarization by 45° each time would be: $B \approx 6.05 \times 10^3$ gauss.


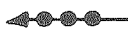
Figure 4 shows the overall 90° rotation of the light beam upon passage through the rotator twice. As is shown in the figure, the beam first passes through a calcite prism (polarizer) with its optic axis parallel to the beam polarization plane, then the beam is rotated by 45° through the Faraday crystal, and finally passes through the second calcite prism (analyzer) whose optic axis is tilted at the same angle. Now, if the beam is reflected back through the analyzer, it will be rotated again by 45° through the Faraday crystal, and will emerge with a plane of polarization rotated by 90° to the polarizer optic axis. This of course prevents the beam from passing through the polarizer and will be refracted out of the laser optic axis as desired.

It should be noted here that the beam coming out of the laser head is normally polarized in the horizontal plane. Since the need may arise to have it polarized in the vertical plane or at 45° to it, the presence of Faraday isolators adds some flexibility towards accomplishing that without the need for extra optics. For example, if one needs a beam polarized in the vertical plane, then it is

Figure 4. Schematic layout of the optical elements of a Faraday rotator. Arrows indicate the polarization vector of transmitted beam.



TRANSMITTED BEAM:  and 

REFLECTED BEAMS:  and 

XBL 788-5611

Fig. 4.

only necessary to reverse the two electrodes connected across the second (last) Faraday crystal, for reversing the direction of the applied magnetic field rotates the polarization plane by 45° in the opposite direction. This leads to a beam polarized in the vertical plane and, therefore, requires the analyzer to be rotated by 90° to its original orientation in order to transmit the output beam. If, on the other hand, the beam needs to be polarized at 45° to the horizontal plane, then the last Faraday crystal and analyzer should be taken out of the beam. In this case, it is essential to prevent the output beam from reflecting back along the laser optics axis. This is usually done by tilting whatever optical components are used outside the laser head such that the reflected portion of the beam is slightly off-axis.

2. Q-Switching

Q-switching of the Nd:YAG laser is provided by a Pockels cell mounted within the master oscillator cavity. This is simply a device which utilizes the electro-optic effect demonstrated by some uniaxial crystals such as ADP, KDP, or KD*P.⁵⁴ In this type of crystal, a beam of plane polarized light whose propagation vector is aligned with the crystal optic axis (z-axis), and whose plane of polarization is parallel to either of the x or y crystallographic axes will pass through unretarded. If, however, an electric field is applied across the crystal z-axis, the crystallographic x and y axes will then be rotated by an angle proportional to the applied electric field. This induces a phase shift between the two orthogonal components of the beam polarization vector (e-ray and o-ray) and therefore results in

rotation of the polarization plane. The magnitude of this rotation (γ) is a function of the applied electric field (V), the crystal electro-optic coefficient (r_{63}), the refractive index of the transmitted beam (n_0), and the wavelength (λ) according to:⁵⁵

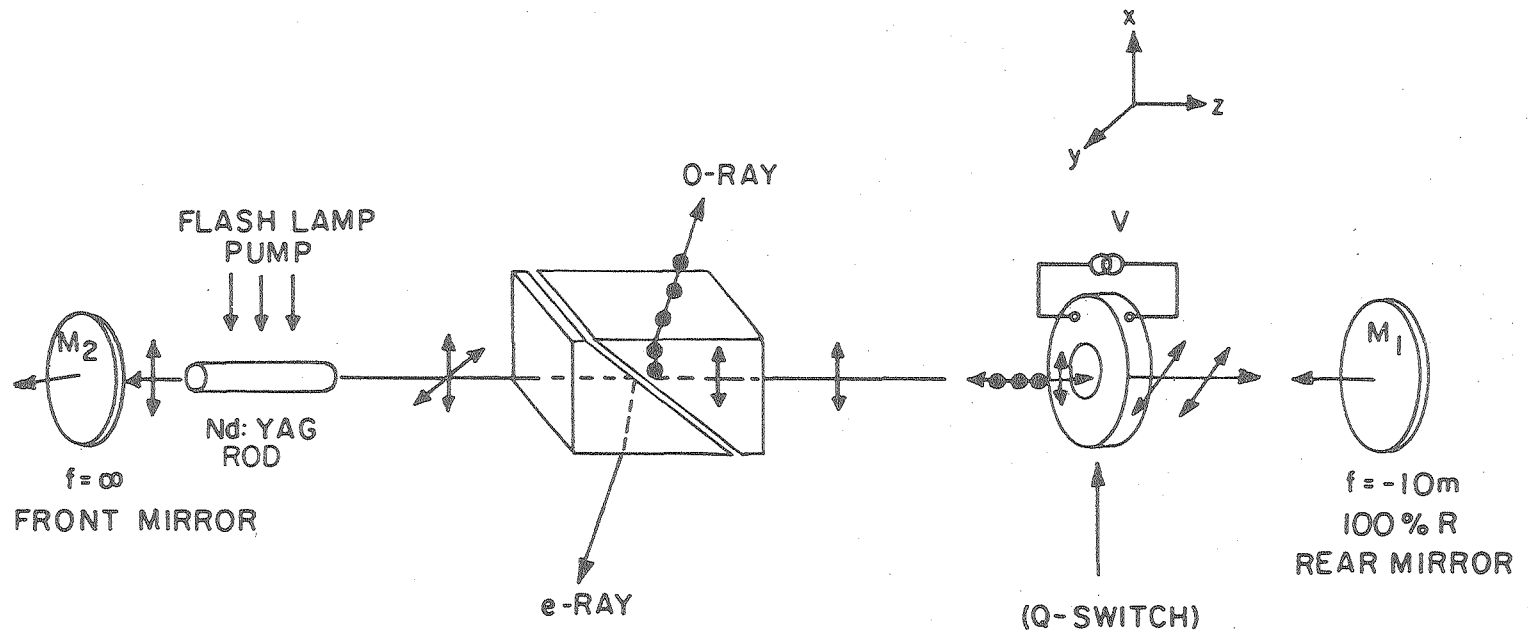
$$\gamma = n_0^3 r_{63} V / \lambda \quad (34)$$

where γ is expressed in units of wavelengths (λ), V in volts, r_{63} in micron/volt, and λ in microns.

It is seen here that the electro-optic crystal functions as a retardation plate where by varying the applied electric field it is possible to produce circularly polarized light from a plane polarized beam (45° overall rotation such as in $\lambda/4$ plate) or else rotation of the beam polarization plane by 90° as in the case of a $\lambda/2$ retardation plate. This later type of rotation is the one used for Q-switching in the present laser. The crystal is KD^*P purchased from Lasermetrics (Q-switch model 1057 FV) with an electro-optic coefficient $r_{63} = 2.64 \times 10^{-5}$ microns/volt. Thus for a $\lambda/2$ retardation at $\lambda = 1.06$ microns with $n_0 \cong 1.52$, the electric field required would be according to eq. (34) equal to ~ 2.87 kV. KD^*P is more suitable in this case for its higher transmission at 1.06μ and, also, for its higher electro-optic coefficient (which means less voltage is needed) relative to KDP or ADP.⁵⁵

Figure 5 shows a schematic of the master oscillator cavity and the position of the Pockels cell within the cavity. The calcite prism which is situated between the laser rod and the Q-switch will only transmit the beam reflected back by the rear mirror (M_1) during the

Figure 5. Schematic of the optical components within the Master Oscillator cavity including the Q-switch. Arrows indicate the polarization vector of the beam.



XBL 788-5612

Fig. 5.

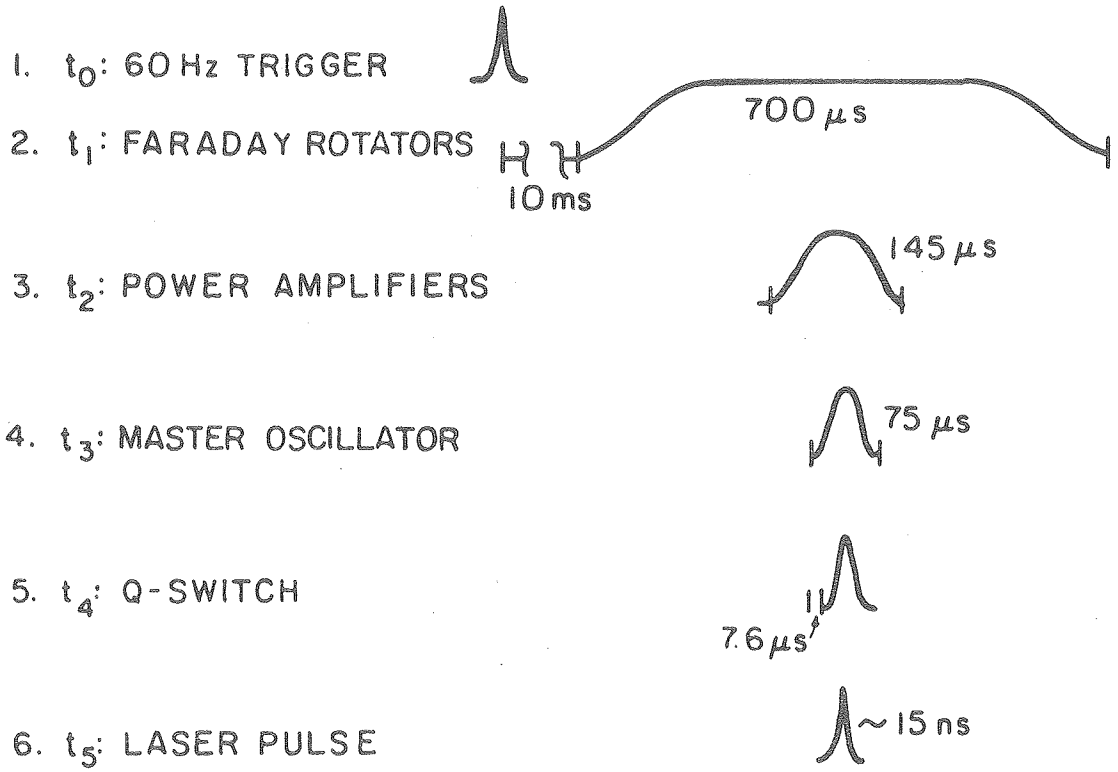
short period in which the Q-switch is deenergized. The timing sequence used for activating the Faraday rotators, firing the power amplifier and then the master oscillator flash lamps followed by deenergization of the Q-switch is indicated in Figure 6.

Care should always be taken not to activate the Q-switch except when the laser is in use, for it seems that prolonged energization shortens its lifetime.

3. Alignment of the Laser Optics

In order to get the Nd:YAG laser beam in the TEM_{00} mode it is necessary to have all optics aligned perfectly, especially those of the master oscillator. A He-Ne laser beam propagating through mirror M_3 , the first amplifier rod, the negative lense (L) and the output mirror (M_2) should be reflected back along the same axis by the rear mirror (M_1) (see Figures 2 and 4 for the layout of optical components). With the Q-switch removed from the master oscillator cavity, adjustment of the rear mirror (M_1) mount through the set of three screws insures reflection of the He-Ne beam onto itself. The next step would be to install the Q-switch in its mount, remove the He-Ne laser and turn on the Faraday rotator power supplies, the master oscillator power supply and activate the Q-switch. Now, with the master oscillator turned on, the beam shape is checked by a Polaroid print. If the fringe pattern is concentric and well-defined, then the laser is oscillating in the TEM_{00} mode as required. This is not normally the case, however, for final tuning of the rear mirror is done by monitoring the beam output power using a photodiode and

Figure 6. Timing sequence employed in firing the Nd:YAG laser.



XBL788-5613

Fig. 6.

scope until maximum power is obtained. A further check on the beam shape is necessary and is done as mentioned above.

After aligning the master oscillator optics, it is then necessary to ensure that the output beam is propagating through the center of the amplifier rods and Faraday rotators (see Figure 2). This is easily done using a video TV Camera (Hitachi CCTV model HV-62U) coupled with a TV video monitor (Hitachi VM-909U) to monitor the position of the beam incident on the amplifier rods. The procedure is as follows: insert a teflon ring into position on the second amplifier beam incidence port and place the TV camera facing the teflon ring. Now, turn the master oscillator on and watch the image of the incident beam within the teflon ring on the TV monitor. If the beam does not pass through the center of the teflon ring, that is, the center of the amplifier rod, then adjustment of a couple of screws attached to the mirror mount (M_3) would help complete alignment of the beam to the center of the amplifier rod. Once that is done, the teflon ring is removed and positioned similarly on the third amplifier stage and the TV camera is placed facing that ring. Now, adjustment of mirror (M_4) will allow alignment of the beam to the center of the third amplifier as in the case of the second amplifier mentioned above.

It should be emphasized here that alignment of the beam to coincide with the center of the last two amplifier stages should be checked very frequently since it improves the beam quality and output power. It is only when this procedure does not improve the output power or beam shape that the master oscillator should be aligned.

There are two types of uniaxial crystals, however. One is a positive uniaxial for which $\eta_e > \eta_o$, such as quartz, and the other is negative uniaxial for which $\eta_e < \eta_o$; KDP, KD^*P , and ADP crystals belong to this latter class.^{54,56} This property lends itself to the use of the above crystals for frequency doubling and also up-conversion (called mixing) as is described below.

1. Phase Matching

Since the refractive index of most materials, including the above crystals, increases with the frequency of the incident photon, then it is possible to phase match two photons of different frequency by a proper choice of which one is to be aligned relative to the optic z-axis as an o-ray. For example, if the crystal is negative uniaxial ($\eta_e < \eta_o$), then in order to phase match an incident beam of photons with its second harmonic, the incident beam is to be aligned with its polarization vector perpendicular to the plane defined by the z-axis and the propagation direction (as an o-ray) so that the second harmonic (twice the frequency) would propagate through the crystal as an e-ray. This should become more evident if one recalls from the above discussion that the refractive index of an e-ray depends on its propagation direction relative to the z-axis. Now, since both beams propagate along the same axis, then it is only necessary to choose the angle between the incident beam propagation vector and the crystal z-axis at which both beams will have the same refractive index (phase matching). The angle (θ) at which $\eta_e(\theta) = \eta_o$ is given by the index ellipsoid:^{53,57}

There are two types of uniaxial crystals, however. One is a positive uniaxial for which $n_e > n_o$, such as quartz, and the other is negative uniaxial for which $n_e < n_o$; KDP, KD*P, and ADP crystals belong to this latter class.^{54,56} This property lends itself to the use of the above crystals for frequency doubling and also up-conversion (called mixing) as is described below.

1. Phase Matching

Since the refractive index of most materials, including the above crystals, increases with the frequency of the incident photon, then it is possible to phase match two photons of different frequency by a proper choice of which one is to be aligned relative to the optic z-axis as an o-ray. For example, if the crystal is negative uniaxial ($n_e < n_o$), then in order to phase match an incident beam of photons with its second harmonic, the incident beam is to be aligned with its polarization vector perpendicular to the plane defined by the z-axis and the propagation direction (as an o-ray) so that the second harmonic (twice the frequency) would propagate through the crystal as an e-ray. This should become more evident if one recalls from the above discussion that the refractive index of an e-ray depends on its propagation direction relative to the z-axis. Now, since both beams propagate along the same axis, then it is only necessary to choose the angle between the incident beam propagation vector and the crystal z-axis at which both beams will have the same refractive index (phase matching). The angle (θ) at which $n_e(\theta) = n_o$ is given by the index ellipsoid:^{53,57}

$$\left[1/\eta_e(\theta)\right]^2 = \left[\cos\theta/\eta_o\right]^2 + \left[\sin\theta/\eta_e\right]^2 \quad (35)$$

In the case of second harmonic generation where $\omega_2 = 2\omega$, the phase matching condition is given by $\eta_e(\theta, 2\omega) = \eta_o(\omega)$, and the phase match angle (θ_m) is determined from eq. (35) by substituting $\eta_o(\omega)$ for $\eta_e(\theta)$ thus one obtains:

$$\left[1/\eta_o(\omega)\right]^2 = \left[\cos\theta_m/\eta_o(\omega)\right]^2 + \left[\sin\theta_m/\eta_e(2\omega)\right]^2 \quad (36)$$

solving for θ_m , one gets:

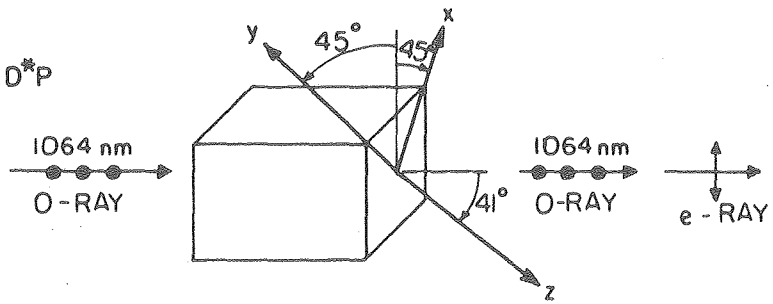
$$\theta_m = \left[\arcsin \left\{ \frac{(\eta_o(\omega))^{-2} - (\eta_o(2\omega))^{-2}}{(\eta_e(2\omega))^2 - ((\eta_o(2\omega))^2)} \right\} \right]^{1/2} \quad (37)$$

As an example, let us consider the generation of the second harmonic of 1064 nm at 532 nm in the negative uniaxial crystal KD^*P shown in Figure 7a. Here we have $\eta_e = 1.494$ at 1064 nm and $\eta_o = 1.5126$ and $\eta_e = 1.4708$ at 532 nm, so by substituting these figures into eq. (37) one obtains: $\theta_m \cong 41^\circ$.

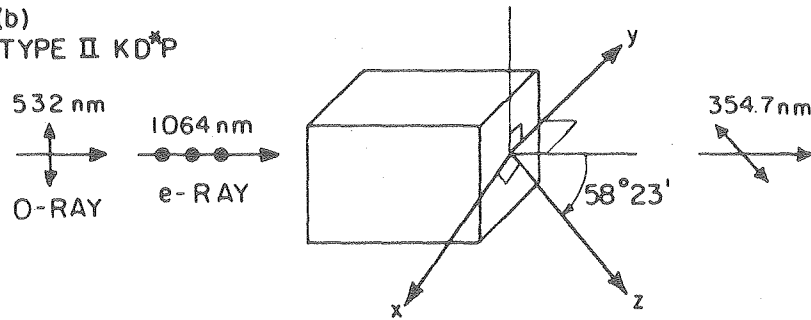
The phase matching considered above is called type I phase matching, for the sum frequency is obtained from two photons of the same polarization vector relative to the crystal z-axis (both photons at 1064 nm were aligned as an o-ray). Whenever the two photons to be summed up have orthogonal polarization, then it is necessary to have a crystal cut for type II phase matching. Figure 7b shows such a crystal (KDP type II) used to sum the Nd:YAG Fundamental at 1064 nm with its second harmonic in order to generate the third harmonic at 354.7 nm. Here one of the two beams is aligned as an o-ray and the other as an e-ray relative to the second mixing crystal z-axis. The choice of which

Figure 7. Nonlinear crystals used to generate the optical harmonics of Nd:YAG laser frequency at 1064 nm. (a) Indicates KD^*P type I crystal used to generate the second harmonic at 532 nm. (b) KD^*P type II crystal used to mix the fundamental with the second harmonic to obtain the third harmonic at 354.7 nm. (c) KDP type I crystal for doubling the frequency at the second harmonic to get the fourth harmonic at 266 nm. (d) Shows the configuration of a KD^*P type II crystal used for obtaining the second harmonic. The phase match angles and crystal axis are indicated for each.

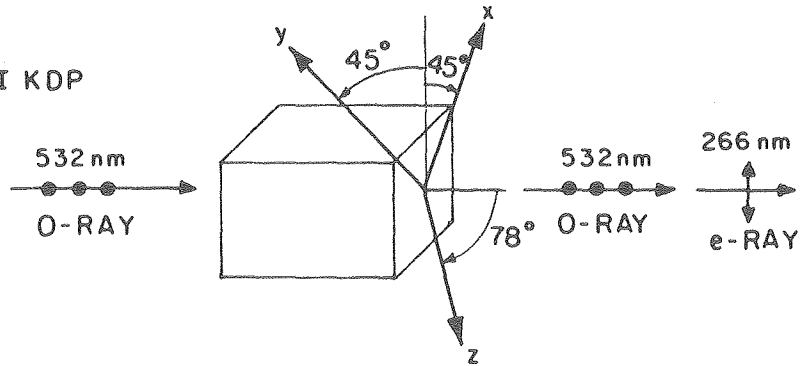
(a)
TYPE I KD*P



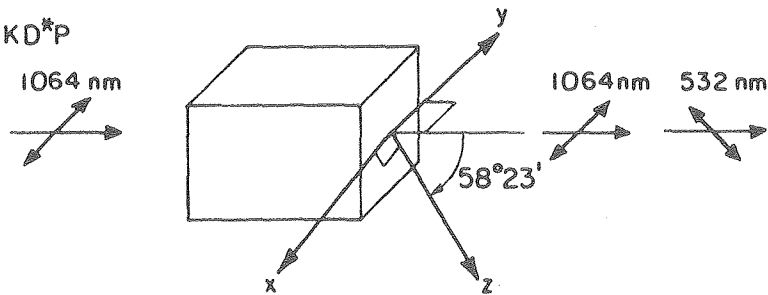
(b)
TYPE II KD*P



(c)
TYPE I KDP



(d)
TYPE II KD*P



XBL788-5614

Fig. 7.

to be aligned as an o-ray is normally determined by an examination of the individual refractive indices, and figuring out which one requires the lower phase match angle (θ_m). A lower phase match angle is desirable since it offers better conversion efficiency as will be shown later. The condition for phase matching of ω_3 with ω_1 and ω_2 where $\omega_3 = \omega_1 + \omega_2$ is given by either of the following equations:⁵³

$$\eta_e^{\omega_3}(\theta_m) \omega_3 = \eta_o^{\omega_1} \omega_1 + \eta_e^{\omega_2}(\theta_m) \omega_2 \quad (38)$$

$$= \eta_e^{\omega_1}(\theta_m) \omega_1 + \eta_o^{\omega_2} \omega_2 \quad (39)$$

where ω denotes the photon angular frequency ($\omega = \frac{2\pi\nu}{\lambda}$). Now, if one examines the refractive indices, namely: $\eta_o = 1.4937$, $\eta_e = 1.4597$ at 1064 nm; $\eta_o = 1.5126$, $\eta_e = 1.4708$ at 532 nm; and $\eta_o = 1.5318$, $\eta_e = 1.4862$ at 354.7 nm, substitution of these values into eq. (38) and also eq. (39) indicates a lower phase match angle when ω_1 at 1064 nm is used as an e-ray and ω_2 at 532 nm is aligned as an o-ray ($\theta_m \approx 58^\circ$). Consequently, the third harmonic will emerge as an e-ray with its polarization vector at 45° to the two other beams (see Figure 7b).

The fourth harmonic at 266 nm was obtained by using a third KD*P type I crystal cut at an angle of $\sim 78^\circ$ to the z-axis. This is close to the phase matching angle for doubling the second harmonic at 532 nm obtained using either of the above two crystals. Figures 7c and 7d indicate the phase match angles for both types of crystals I or II used to obtain the fourth and second harmonics, respectively.

Each of the above three crystals were mounted on a two dimensional Kinematic Burleigh mount so that final tuning of crystal angles was made and power conversion efficiency was therefore maximized.

2. Conversion Efficiency

Here we consider the general case of optical parametric conversion treated by Amnon Yariv,^{1,5} and then use it to derive the conversion efficiency of the frequency doubling crystals mentioned above.

If we assume two beams of photons of frequencies ω_1 and ω_2 traversing a nonlinear crystal and adding up to another beam of frequency ω_3 , then the change in their electric field vectors (E_i) along the crystal optic axis is given by:^{53,57}

$$dE_1/dz = -1/2(\mu_0/\epsilon_1)^{1/2} \left[\sigma_1 E_1 + i\omega_1 d E_3 E_2^* e^{-i(K_3 - K_2 - K_1)z} \right] \quad (40)$$

$$dE_2/dz = -1/2(\mu_0/\epsilon_2)^{1/2} \left[\sigma_2 E_2 - i\omega_2 d E_1 E_3^* e^{-i(K_1 - K_3 + K_2)z} \right] \quad (41)$$

$$dE_3/dz = -1/2(\mu_0/\epsilon_3)^{1/2} \left[\sigma_3 E_3 + i\omega_3 d E_1 E_2 e^{-i(K_1 + K_2 - K_3)z} \right] \quad (42)$$

where μ_0 is the permeability of free space = $4\pi \times 10^{-7}$ mks units
 $\sigma_1, \sigma_2, \sigma_3$ are the conductivities and $\epsilon_1, \epsilon_2, \epsilon_3$ are the permittivities of the individual photons ω_1, ω_2 and ω_3 , respectively (within the crystal); E_1, E_2, E_3 is their electric field vectors; and d is the nonlinear polarization coefficient along the z-axis. Now, if we make the assumption that the electric field amplitudes at ω_1 and ω_2 remain unattenuated throughout the crystal (which is a reasonable assumption in light of the normally small conversion efficiencies obtained), then both E_1 and E_2 could be considered constant and we need only to evaluate E_3 , that is:

$$dE_3/dz = -1/2(\mu_0/\epsilon_3)^{1/2} \left[\sigma_3 E_3 + i\omega_3 dE_1 E_2 e^{-i\Delta K z} \right] \quad (43)$$

where $\Delta K = K_1 + K_2 - K_3$ and K is the wave vector. Equating σ_3 to zero and integrating E_3 over the crystal length (ℓ), we obtain:

$$E_3 = \frac{i\omega_3}{2} (\mu_0/\epsilon_3)^{1/2} dE_1/E_2 \left(\frac{e^{-i\Delta K \ell} - 1}{\Delta K} \right) \quad (44)$$

Since the intensity I is related to the electric field vector by:

$I = 1/2(\epsilon/\mu_0)^{1/2} EE^*$, then I_3 will be given by:

$$I_3 = \frac{\omega_3^2}{8} (\mu_0/\epsilon_3)(\epsilon_3/\mu_0)^{1/2} d^2 E_1^2 E_2^2 \frac{2 - e^{i\Delta K \ell} - e^{-i\Delta K \ell}}{(\Delta K)^2} \quad (45)$$

Again, recognizing the trigonometric equivalents $e^{ix} + e^{-ix} = 2\cos x$, $1 - \cos x = 2\sin^2 x/2$, and substituting for E_1 and E_2 , the above equation reduces to

$$I_3 = 1/2(\mu_0/\epsilon_3)^{1/2}(\mu_0/\epsilon_2)^{1/2}(\mu_0/\epsilon_1)^{1/2} \omega_3^2 d^2 \ell^2 I_1 I_2 \times \left(\frac{\sin^2 \Delta K \ell/2}{(\Delta K \ell/2)^2} \right) \quad (46)$$

Also, since $\epsilon/\epsilon_0 = \eta^2$ where η is the refractive index, and letting $\phi = (\sin^2 \Delta K \ell/2)/(\Delta K \ell/2)^2$, and substituting for $\mu_0 = 4\pi \times 10^{-7}$ and $\epsilon_0 = 8.854 \times 10^{-12}$ in mks units, eq. (46) can be rewritten as

$$I_3 = 1/2(\mu_0/\epsilon_0)^{3/2} \omega_3^2 d^2 \ell^2 I_1 I_2 \phi / \eta_1 \eta_2 \eta_3$$

or (47)

$$I_3 = 2.67 \times 10^7 \omega_3^2 d^2 \ell^2 I_1 I_2 \phi / \eta_1 \eta_2 \eta_3$$

The above relation serves as the fundamental equation used to estimate the power conversion efficiency for any optical parametric oscillator utilized for three wave mixing. In the case of second harmonic generation where $\omega_3 = \omega_1 + \omega_2 = 2\omega$, $I_1 = I_2$, ϕ is equal to unity at exact phase matching where $\Delta K = 0$, $\eta_1 = \eta_2 = \eta_0$, and $\eta_3 = \eta_3(2\omega)$, eq. (47) assumes the general form

$$I_{2\omega} = 1.07 \times 10^8 \omega^2 d^2 \ell^2 I_{\omega}^2 / \eta_0^2 \eta_e^2(2\omega) \quad (48)$$

$$I_{2\omega}/I_{\omega} = 1.07 \times 10^8 \omega^2 d^2 \ell^2 I_{\omega} / \eta_0^2 \eta_e^2(2\omega) \quad (49)$$

The conversion efficiencies for the second, third and fourth harmonics of the Nd:YAG laser are calculated below.

(i) Second Harmonic

For the KD*P type I crystal used in this work, the nonlinear optical susceptibility coefficient at 1064 nm is $d_{36} = 0.6943 \times 10^{-12}$ meter/volt = 7.714×10^{-24} mks units. At 41° phase match angle, the effective value of the coefficient becomes $d = d_{36} \sin 41^\circ \approx 5.061 \times 10^{-24}$ mks units.⁵⁹ Substituting this value for d , and also $\ell = 2.5$ cm, $\eta_0 = 1.4948$, $\eta_e = 1.472$, $\omega = 1.772 \times 10^{15}$ Hz at 1064 nm, and $I_{\omega} = 130$ MW/cm² at 1064 nm, the power conversion efficiency to 532 nm is calculated from equation (49) as $I_{2\omega}/I_{\omega} = 28\%$. this is just about equal to the conversion efficiency of 30% obtained in this work where ($I_{2\omega}$ was typically ~ 45 MW/cm²).

(ii) Third Harmonic

Here we use the general eq. (47) which for a KD*P type II phase matching assumes the form:

$$I_3/I_1 = 2.67 \times 10^7 \omega_3^2 d^2 \ell^2 I_2 / \eta_{e1} \eta_{o2} \eta_{e3} \quad (50)$$

where I_1 is the power input of the fundamental frequency at 1064 nm, I_2 is that of the second harmonic where $I_2 \approx 45 \text{ MW/cm}^2$, $\omega_3 = \omega_1 + \omega_2 = 5.314 \times 10^{15} \text{ Hz}$ at 354.7 nm, $\eta_{e1} = 1.4597$ (at 1064 nm), $\eta_{o2} = 1.5126$ (at 532 nm), $\eta_{e3} = 1.4862$ at 532 nm,⁶⁰

$$d = 1/2 \frac{0.72 \times 10^{-12}}{9 \times 10^{10}} \sin 45^\circ \approx 2.624 \times 10^{-24} \text{ mks}$$

units,⁵⁹ and $\ell = 2.5 \text{ cm}$. The conversion efficiency to the third harmonic is then calculated to be $I_3/I_1 \approx 11\%$ which is in accord with 12% obtained in this work (I_3 was typically $\approx 15 \text{ MW/cm}^2$).

(iii) Fourth Harmonic

The second harmonic was frequency doubled in a KDP type I crystal with

$$d = \frac{0.75 \times 10^{-12}}{9 \times 10^{10}} \sin 78^\circ \approx 8.15 \times 10^{-24} \text{ mks}$$

units.⁵⁹ The equation used assumes the following form:

$$I_2/I_1 \approx 1.07 \times 10^8 \frac{\omega_1^2 d^2 \ell^2}{\eta_o^2 \eta_e} I_1 \quad (51)$$

where $I_1 \approx 45 \text{ MW/cm}^2$ (the power input at the second harmonic 532 nm), $\eta_o = 1.5126$ at 532 nm, $\eta_e = 1.511$ at 266 nm, $\ell = 2.5 \text{ cm}$ and $\omega = 3.54 \times 10^{15} \text{ Hz}$. The conversion efficiency is estimated to be ~29%. About 28% conversion from the second harmonic was obtained (~14 MW/cm^2 was obtained, typically).

D. STIMULATED RAMAN SCATTERING

Stimulated Raman emission in H_2 gas was utilized to generate ultraviolet radiation of different frequency. Here, one of the Nd:YAG laser optical harmonics was used to pump the first Stokes emission of H_2 . This corresponds to the $Q_1(1)$ branch ($v = 1 \rightarrow v = 0, \Delta J = 0$) which happens to have a relatively high Raman scattering cross section.⁶¹ The vibrational frequency corresponding to this level is $\omega_R = 4155 \text{ cm}^{-1}$, so when the fourth harmonic at 266 nm ($\omega_p = 37,590 \text{ cm}^{-1}$) was used as the laser pump, Stokes emission at 299.1 nm was obtained ($\omega_s = \omega_p - \omega_R = 33435 \text{ cm}^{-1}$). A brief analysis of the theory and experimental conditions applied to hydrogen gas is attempted below.

In order to understand the theory of stimulated Raman emission, let us start with the definition of the spontaneous process, whereby, the number of Stokes photons scattered per unit length of the medium and per unit solid angle Ω is given by:⁶²

$$dN_s/dz = NN_p(d\sigma/d\Omega) \quad (52)$$

where N designates the number of molecules in the ground state, N_p is the number of incident photons of the pump beam, z is the path length traversed by the pump beam, and $d\sigma/d\Omega$ is the scattering cross section per unit solid angle Ω .

Stimulated emission occurs however as the molecules in the upper vibrational level with population N_u return to the ground state while a Stokes photon is absorbed and a laser pump photon is emitted. The rate of stimulated emission will therefore be proportional to the number of Stokes photons N_s , the population difference between the

ground and upper levels ($N - N_u$), and a line shape function representing the Stokes transition width $S(\omega_s)$. This rate per unit path length is then given by:

$$dN_s/dz = N_s N_p (N - N_u) \left\{ \frac{4\pi^2 c^3}{\omega_s^2 \eta_s^2} \right\} \frac{d\sigma}{d\Omega} S(\omega_s) \quad (53)$$

where the wavy brackets enclose the total number of states emitting Stokes photons per unit volume per unit frequency (c is the speed of light and η_s is the refractive index for stokes photons). The line shape function $S(\omega_s)$ can be represented by a Lorentzian curve whose full width at half maximum is given by a damping constant according to:

$$S(\omega_s) = \frac{\Gamma}{(\omega_p - \omega_s - \omega_R)^2 + (\Gamma/2)^2} \quad (54)$$

Now, if we assume a resonant Raman process where $\omega_p = \omega_s + \omega_R$, then the line shape function reduces to $4/\Gamma$ and eq. (53) becomes

$$\begin{aligned} dN_s/dz &= \frac{16\pi^2 c^3 (N - N_u)}{\omega_s^2 \eta_s^2 \Gamma} \frac{d\sigma}{d\Omega} N_p \cdot N_s \\ &= g_s \cdot N_s \end{aligned} \quad (55)$$

where g_s is normally called the gain coefficient and is set equal to:

$$g_s = \frac{16\pi^2 c^3 (N - N_u)}{\omega_s^2 \eta_s^2 \Gamma} \frac{d\sigma}{d\Omega} N_p \quad (56)$$

Equation (56) can be transformed into a more familiar form by substituting for

$$N_p = \frac{n_p}{h\omega_p c} I_p$$

where I_p is the pump laser power per cm^2 and n_p is the refractive index for the pump photons within the medium, and also by substituting for $\omega_s = 2\pi c/\lambda_s$ thus we have

$$g_s = \frac{4\lambda_s^2 n_p^2 (N - N_u)}{h\omega_p \eta_s^2} \frac{d\sigma}{d\Omega} I_p \quad (57)$$

The gain coefficient is now given in units of cm^{-1} , and if we integrate eq. (55) we obtain:

$$N_s = N_0 e^{g_s z} \quad \text{or equivalently} \quad I_s = I_0 e^{g_s z} \quad (58)$$

where I_s and I_0 represent the Stokes power at the exit and entrance of the gain medium, and N_s and N_0 are the corresponding number of photons.

It is now apparent from eq. (58) that the gain in stimulated Raman emission grows exponentially with the distance traversed by the pump beam. The gain coefficient is however linearly proportional to the pump laser power as well as the density of the medium. For H_2 gas at room temperature, the spontaneous Raman scattering cross section was measured as

$$\frac{d\sigma}{d\Omega} = 5.30 \times 10^{-30} \text{ cm}^2/\text{Steradian.}^{63}$$

This value corresponds to the Q(1) branch which normally carries the highest polarizability coefficient.⁶⁴ The Raman Stokes linewidth varies with pressure and is dominated by the Doppler width of $\sim 0.2 \text{ cm}^{-1}$ at pressures below one amagat⁶⁵ (amagat is a unit for gas density which corresponds to the density at 1 atmosphere and 0°C). As the H₂ pressure is increased above one amagat, the line width decreases to about 0.05 cm^{-1} at about 12 amagats, an effect related to collisional narrowing where the linewidth becomes inversely proportional to pressure.⁶⁶ Above 12 amagats, the linewidth rises to $\sim 0.2 \text{ cm}^{-1}$ in the vicinity of 100 amagats.⁶⁵ Those measurements were verified for both forward and backward scattering,^{65,66} and it is to be noted here that the linewidth is expected to be higher for backward scattering where it is given by the formula:⁶⁵

$$(\Delta\omega_D)_{\text{backward}} = (\omega_p + \omega_s) \left(\frac{8KT \ln 2}{mc} \right)^{1/2} \quad (59)$$

where ω_p is the pump laser frequency and ω_s is that of the Stokes emission. Other authors indicated linewidths of $\sim 0.1 \text{ cm}^{-1}$ at 32 atm pressure,⁶⁷ and $0.023\text{-}0.030 \text{ cm}^{-1}$ at unreported pressures for a pump laser at 6943Å.⁶⁸

It is obvious from the above discussion that in order to enhance the gain at the Stokes emission, it would be desirable to use gas pressures at which the linewidth will be minimum (eq. (57) shows the gain to be inversely proportional to linewidth Γ). This was not attempted however since we were limited by the pump laser linewidth

of $\sim 0.2 \text{ cm}^{-1}$. For this, and since the gain is proportional to gas density, a H_2 gas pressure of ~ 80 atmospheres was used (at room temperature). This corresponds to a gas density of $N \approx 1.97 \times 10^{21} \text{ molecules/cm}^3$. The refractive indices are calculated to be $n_s \approx 1.0108$,⁶⁹ $n_p \approx 1.0109$, and the gain coefficient is estimated from equation as $g_s/I_p \approx 1.32 \times 10^{-9} \text{ cm}^{-1} \text{ watt}^{-1}$ for a pump laser frequency at 226 nm. The measured gain coefficients for pump frequency at 6943 are in the range $1.25 - 2.0 \times 10^{-9} \text{ cm}^{-1} \text{ watt}^{-1}$.^{67,70} At 1.06μ , Beyer and Herbst reported a gain coefficient of $4 \times 10^{-9} \text{ cm}^{-1} \text{ watt}^{-1}$ at 20 atm of H_2 gas.⁷¹

For the pump laser power of $\sim 100 \text{ MW/cm}^2$ at 266 nm used here (beam diameter of $\sim 1 \text{ mm}$), and at 80 atm of H_2 in a 50 cm long cell, the overall gain calculated according to equation is $g_s \approx 7$. The overall conversion efficiency was $\sim 22\%$ (4.9 mJ/pulse at the Stokes line compared with $\sim 22 \text{ mJ/p}$ at 266 nm pump wavelength).

It was observed that when the pump laser beam was tightly focused at the center of the cell, the first anti-Stokes line as well as higher c.p. Stokes lines gain in intensity at pressures below 4 atmospheres. On the other hand, when the pump beam was reduced in diameter while remaining collimated, only the first Stokes line acquires gain while the others diminish in intensity especially at pressures above 5 atm. This observation may be rationalized on the basis of the pressure dependence of refractive index which tends to put the forward anti-Stokes emission as well as higher Stokes lines out of phase matching at higher gas pressures. Stoicheff, et al.⁷² and Townes, et al.⁷³ have

made an analysis of the phase matching conditions for the Stokes and Anti-Stokes Raman emission which is described briefly below.

Considering stimulated anti-Stokes emission in the forward direction as a result of four-wave mixing, that is, a coherent interaction between two pump laser photons (ω_p), the first Stokes photon ($\omega_s = \omega_p + \omega_R$), and the vibrational phonon (ω_R), then phase matching occurs when the following vector relation is satisfied:

$$\vec{k}_p + \vec{k}_p = \vec{k}_s + \vec{k}_{as} \quad (60)$$

where k_p , k_s and k_{as} are the wave vectors of the pump, first Stoke, and anti-Stoke photons, respectively. General phase matching formulae which apply to higher order anti-Stokes and Stokes emission is given by

$$\vec{k}_0 + \vec{k}_{n-1} = \vec{k}_{-1} + \vec{k}_n \quad \text{anti-Stokes} \quad (61)$$

$$\vec{k}_0 + \vec{k}_{-1} = \vec{k}_{n-1} + \vec{k}_{-n} \quad \text{Stokes} \quad (62)$$

where k_0 , k_{-1} , k_n , and k_{-n} are the wavevectors for the pump, first Stokes, n^{th} order anti-Stokes, and n^{th} order Stokes, respectively. These wavevector relations could then be used to elucidate the cone angles for anti-Stokes as well as Stokes photons scattered in the forward direction. For the n^{th} order anti-stokes, the cone angle θ_n is derived as

$$\theta_n = \beta_n \pm (\beta_n^2 + \delta_n - \gamma_n)^{1/2} \quad (63)$$

where

$$\beta_n = K_{n-1} \theta_{n-1} / (K_{-1} + K_n)$$

$$\delta_n = 2(K_{-1}/K_n)(K_n + K_{-1} - K_0 - K_{n-1}) / (K_{-1} + K_n)$$

$$\gamma_n = (K_{n-1} - K_{-1}) \beta_n \theta_{n-1} / K_n$$

The cone angles for the n^{th} order Stokes are similarly given by

$$\theta_{-1}^{(n)} = (K_{n-1} \theta_{n-1} - K_n \theta_n) / K_{-1} \quad (64)$$

So using eq. (63) and substituting for $K = 2\pi n/\lambda$, the cone angle for the first anti-stokes emission in the forward direction is given by

$$\theta_1 = \frac{\omega_l}{\eta_p} \frac{\omega_p - \omega_R}{\omega_p + \omega_R} \eta_{p+R} - \eta_{p-R} + \frac{\omega_R}{\omega_p} (\eta_{p+R} - \eta_p + \eta_p - \eta_{p-R})$$

Now, for a laser pump at 266 nm, $\omega_p = 7.06 \times 10^{15}$ radians sec^{-1} , and for H_2 , $\omega_R = 7.81 \times 10^{14}$ radians sec^{-1} , thus $\omega_s = 6.28 \times 10^{15}$ radians sec^{-1} and $\omega_{as} = 7.84 \times 10^{15}$ radians sec^{-1} . The refractive indices are derived from the general dispersion formula for gases at 1 atm and 0°C given by⁶⁹

$$(n\lambda - 1) \times 10^6 = A + B\lambda^{-2} + C\lambda^{-4} \quad (66)$$

where λ is the wavelength in microns. Those indices can then be scaled to the particular gas pressure (p) and temperature T ($^\circ\text{K}$) according to⁶⁹

$$(n - 1) = (n\lambda - 1) \left(\frac{p \text{ atm}}{T/273} \right) \quad (67)$$

For H_2 gas at 80 atmospheres and 300°K one obtains the refractive indices

$$\eta_p = 1.01095$$

$$\eta_s = 1.01082$$

$$\eta_{as} = 1.01141$$

$$n_R = 1.00992$$

when these figures are substituted to eq. (65) the first anti-Stokes cone angle is estimated as 0.023 radians or $\sim 1.3^\circ$. The accuracy of this figure is of course limited by the uncertainty of the derived refractive indices. An approximate formula for the first anti-Stokes relates the cone angle to the gain coefficient and the first Stokes wave vector according to:^{68,74}

$$\theta_1 = (2g_s/k_s)^{1/2} \quad (68)$$

which yields for a gain coefficient of $\sim 7 \text{ cm}^{-1}$ a cone angle of $\sim 7.31 \text{ mrad}$ or $\approx 0.42^\circ$. If they indicate anything, the above two figures show that the gain of the anti-Stokes forward emission is reduced by collimating the pump laser beam rather than focusing it. The effect of pressure increase is probably to put the anti-Stokes gain out of phase matching by the greater increase of the gas dispersion to the anti-Stokes over Stokes frequencies.

E. INFRARED FLUORESCENCE DETECTION

Detection of infrared fluorescence was accomplished using a Cu:Ge photoconductive detector provided with a matching amplifier unit (SBRC-A320) which offered a reasonable detectivity over 2 MHz of electrical bandwidth. The detector element was housed in a metal dewar suitable for cooling down to liquid He temperature (4.2°K) and was also equipped with a set of interference filters cooled near liquid

nitrogen temperature (~100°K). To further reduce the background radiation seen by the detector, the detector element was covered with a MgF₂ or BaF₂ window cooled at liquid He temperature. Also, a gold-plated copper radiation shield cooled at liquid N₂ temperature covered the detector-filter assembly except for an aperture sufficiently small to limit the viewing solid angle of the detector to 0.24 π steradians. Most of the design features for this detector have been covered by Finzi,⁷⁵ and a good discussion of the theory of infrared detectors is also found in Finzi's and Wiesenfeld's theses^{75,76} and several other sources.^{77,87} The most relevant parameters that determine the signal response of a photoconductive detector are only very briefly discussed below.

1. Detectivity

A photoconductive detector such as Cu:Ge is normally characterized by many parameters, one of which is its detectivity (D^{*}). This is defined in terms of the noise equivalent power (NEP) normalized to one unit of the detector surface area (A in cm²) and one unit of the electrical bandwidth (B in Hz) according to:⁷⁷⁻⁸⁷

$$D^* = (AB)^{1/2}/NEP \quad \text{cm Hz}^{1/2}/\text{watt} \quad (69)$$

The noise equivalent power (in units of watt) is simply defined as the root mean square value of signal required to produce a signal to noise ratio (S/N) of unity. Although there exist many sources of noise, one could nevertheless rigorously disregard most of them for a cooled detector and consider only those which contribute the most, namely: the thermal (Johnson) noise and the background black body

noise. For a detector cooled at temperature (T_D) with a resistance R_D and coupled to an amplifier unit with load resistance R_L at temperature T , the noise equivalent power could be defined according to:⁷⁷

$$\begin{aligned}
 (\text{NEP})^2/B &= 4 K T_D R_D / \mathcal{R}^2 + 4 K T R_L / \mathcal{R}^2 + \\
 &\frac{4A(KT)^5}{c^2 h^3} \sin^2 \theta / 2 \int_{x_1}^{x_2} \frac{x^4 e^x}{(e^x - 1)^2} \eta(x) f(x) dx \quad (70)
 \end{aligned}$$

where the first term on the right represents the thermal noise contribution of the detector element, the second term is that of the amplifier unit, and the third term characterizes the background contribution to the noise. Here, K is the Boltzmann constant, \mathcal{R} is the detector responsivity in volts/watt, c is the speed of light, h is Planck's constant, θ is the view angle of the detector, $x = h\nu/KT$, $\eta(x)$ is the quantum efficiency of the detector, and $f(x)$ is the spectral responsivity which could be set equal to unity for a small spectral range. The limits of the integral are determined by the lower and upper values of wavelengths to which the detector is exposed.

An inspection of the above equation shows clearly that in order to minimize the noise equivalent power, it is desirable to reduce the detector temperature (T_D) as well as the background temperature (T). Furthermore, a reduction in both the view angle (θ) and the spectral range ($x_1 \rightarrow x_2$) to which the detector is exposed will also lead to a decrease in the noise equivalent power. This is perhaps better understood if one tries to estimate the relative contribution of each term in eq. (70) to the total or rather equivalent noise power. For example, considering the Ge:Cu detector used in this work with

$T_D = 4.2^{\circ}\text{K}$, $R_D \approx 10 \text{ M}\Omega$, and the responsivity $\mathcal{R} = 4 \times 10^3 \text{ volts/watt}$, the first term yields a value $4 KT_D R_D / \mathcal{R}^2 \approx 1.45 \times 10^{-22} \text{ watt}^2 \text{ Hz}^{-1}$. The second term is evaluated similarly with $T = 300^{\circ}\text{K}$ and $R_L = 10^5$ thus giving a value of $4 KTR_L / \mathcal{R}^2 \approx 1.03 \times 10^{-22} \text{ watt}^2 \text{ Hz}^{-1}$. To evaluate the third term, we consider first the conditions under which the detectivity was evaluated earlier as follows:⁸⁸ $T = 500^{\circ}\text{K}$, $\theta = 60^{\circ}$, and the limits of the integral are set to the spectral frequency range determined by the window material and the detector spectral response, that is: $x_1 = h\nu_1/KT$ corresponding to the window (KRS-5) cutoff wavelength of 0.6μ , and $x_2 = h\nu_2/KT$ is that of the detector cutoff wavelength of 30μ . The detector quantum efficiency $\eta(x)$ is typically 0.6 ,⁸⁷ and the spectral response function $f(x)$ is set approximately equal to unity. With the above considerations, the integral in eq. (70) is evaluated from references 80 through 91 by taking the difference between those values obtained for the limits $0 \rightarrow x_2$ and $0 \rightarrow x_1$ thus yielding

$$\int \frac{x^4 e^x}{(e^x - 1)^2} (x) f(x) dx = 25.71$$

The total value of the third term under the conditions mentioned above is calculated to be $4.61 \times 10^{-22} \text{ watt}^2 \text{ Hz}^{-1}$. At a post detection electrical bandwidth of 2 MHz , the sum of the above three terms give a noise equivalent power $\text{NEP} \approx 3.76 \times 10^{-8} \text{ watt}$. This value substituted to eq. (69) yield a detectivity of $D^* = 2.06 \times 10^{10} \text{ cm Hz}^{1/2}/\text{watt}$. This is very close to the experimentally measured detectivity of $1.5 \times 10^{10} \text{ cm Hz}^{1/2}/\text{watt}$,⁸⁸ with the difference attributed to the assumption of constant spectral response over the wavelength range

2 to 30 μ , as well as a constant quantum efficiency of 0.6 which is a crude approximation.

It should be emphasized however that under normal operating conditions, the background noise is cut down significantly through the use of interference filters with a spectral bandwidth in the range 0.3 to 0.5 μ . Those filters are also cooled down to 77°K thus reducing the background blackbody radiation flux falling on the detector surface by more than two orders of magnitude. The view angle of the detector could also be decreased thus decreasing the background noise contribution by a factor proportional to $\sin^2(\theta_1/2)/\sin^2(\theta_2/2)$ where θ_1/θ_2 . For the detector mentioned above, the view angle was reduced from 60° to 42° thus lowering background contribution to the noise by an extra factor of 2. To illustrate that quantitatively, the third term is evaluated for an interference filter centered at 4.663 μ with a spectral bandwidth of 0.5 μ , and cooled down to 77°K, the third term yields a value of 1.51×10^{-27} watt²/Hz. This gives a noise equivalent power of NEP = 2.22×10^{-8} watt and the detectivity will therefore be $D^* \approx 3.5 \times 10^{10}$ cm Hz^{1/2}/watt; a factor of two improvement over the earlier conditions.

2. Infrared Filters

In experiments designed to measure the time resolved fluorescence intensity of CO at 4.663 μ , a set of two interference filters was used. One, a narrowband filter centered at 4.7 μ (N04701-9 OCLI 84% peak transmission)⁹² with a bandpass of 0.3 μ , was placed inside the detector dewar and cooled at 77°K. The second one was a wideband filter centered at 4.74 μ (W04741-8 OCLI, 80% peak transmission)⁹² with

a band pass of $\sim 2\mu$ placed in a black anodized filter-holder outside the detector, and secured next to the salt window in order to cut down on scattered light. This arrangement allowed almost complete elimination of scattered light viewed by the detector. There were two other filters placed inside the detector dewar, namely: a wide band filtered centered at 3.4μ (W03423-9 OCLI, 72% peak transmission)⁹² and used to look for possible C-H stretching fluorescence from H_2CO at 3.5μ , and a narrowband filter centered at 5.3μ (N05256-8) OCLI, 79% peak transmission)⁹² and used primarily to look for C = O stretching fluorescence from HCO radicals.

A gas filter was also used to isolate fluorescence from vibrational levels of CO higher than $v = 1$. This consisted of a glass cylinder 5 cm long and fitted with two NaCl windows with epoxy resin. This cell was filled with CO at 1 atm pressure which allowed complete attenuation of CO ($v = 1$) fluorescence since the absorptance at 5 cm atm is 50 cm^{-1} .⁹³

F. SIGNAL PROCESSING ELECTRONICS

As mentioned before, a Ge:Cu photoconductive detector was used to convert the infrared fluorescence signal into an electrical current. The current was converted into a corresponding voltage and amplified through an amplifier unit with an overall gain of 40 db. The voltage output of the detector-amplifier was filtered through an RC filter set at an electrical bandwidth of 2 MHz and then fed into a transient digitizer (Biomation 8100) at 10 nsec intervals for a total of 2048 channels. The Biomation system was interfaced with a signal averaging device (Northern NS-575) thus allowing the digital output to be transferred to the Northern at a rate of $10 \mu\text{s}/\text{channel}$. Since the laser source

was normally operated at 10 pps or less, the Northern allowed averaging up to 16,000 pulses. It should be noted here that the signal-to-noise (S/N) ratio was typically 0.02 and never exceeded 0.1 single shot. So, it was necessary to average roughly 10,000 times for each experiment, with the result of an improvement in the S/N ratio by the square root of that number (this is the case since the signal adds up linearly with the number of averages, where as the noise, being random, increases only with the square root of that number).

The signal averager was in turn interfaced with an x-y plotter (HP-7004) which was used to plot the output of the Northern point-by-point to be analyzed later. The exponential rise and decay curve thus obtained was later plotted semilogarithmically in order to calculate the appearance and decay rates as will be shown later.

G. GAS HANDLING SYSTEM

All gases used in this work were handled using a standard glass vacuum system fitted with teflon stopcocks and metering valves to regulate gas flow through the fluorescence cell.

1. Vacuum Line

This consisted of a glass manifold maintained under vacuum by two vacuum pumps: an oil pump capable of reducing the pressure down to a millitorr, and a mercury diffusion pump to bring the pressure below a microtorr. The two pumps were connected to the main manifold through two liquid nitrogen traps in order to prevent oil or mercury from diffusing back through the vacuum system. The pressure was read using a standard ionizing Phillips gauge sensitive to better than 0.1 microtorr, and the combined degassing and leak rate was tested

and maintained at about one tenth of a millitorr per hour. Gas preparation and mixing were handled within the vacuum manifold, and gas flow through the fluorescence cell was accomplished according to the following description.

2. Gas Flow System

The fluorescence cell was connected to the glass manifold through two glass arms, one on each side. One arm served as the gas input source with a system of teflon stopcocks and a metering valve to regulate the gas flow into the cell, and the other served as the gas pump outside leading through another system of teflon stopcocks and a metering valve into the main manifold. (Both metering valves were supplied by Nupro Company, Cleveland, Ohio, Model 55-4MA).

The gas source was connected to the input arm and was isolated from the glass manifold during photolysis by a teflon stopcock. The output arm led directly through the manifold into the liquid nitrogen traps so that the gas was continuously pumped out. The gas flow rate was regulated using both metering valves situated on either side of the fluorescence cell. The output valve was normally adjusted to allow a steady flow out of the cell with the input valve regulated such that the gas sample will be continuously replenished at constant pressure. For example, in case of H_2CO photolysis at 354.7 nm with a laser pulse energy of 20 mJ/p at 10 pps pulse repetition rate, the flow rate necessary to replenish the gas sample in a cell of 90 cm^3 volume traversed by the beam four times (path length = 100 cm) was calculated to be roughly $1.5 \text{ cm}^3/\text{sec}$. This was achieved by opening the output metering valve almost fully while adjusting the input valve

to allow for constant pressure. The above flow rate corresponds to a linear gas flow of 0.5 cm/sec across the fluorescence cell. Now, since a complete fluorescence signal sweep was normally completed in less than 10 ms, no correction was necessary for the effect of gas flow on the fluorescence decay rates. This was also confirmed by the insensitivity of decay rates when the flow rate was increased or decreased by a factor of two about the value mentioned above (1.5 cm³/sec).

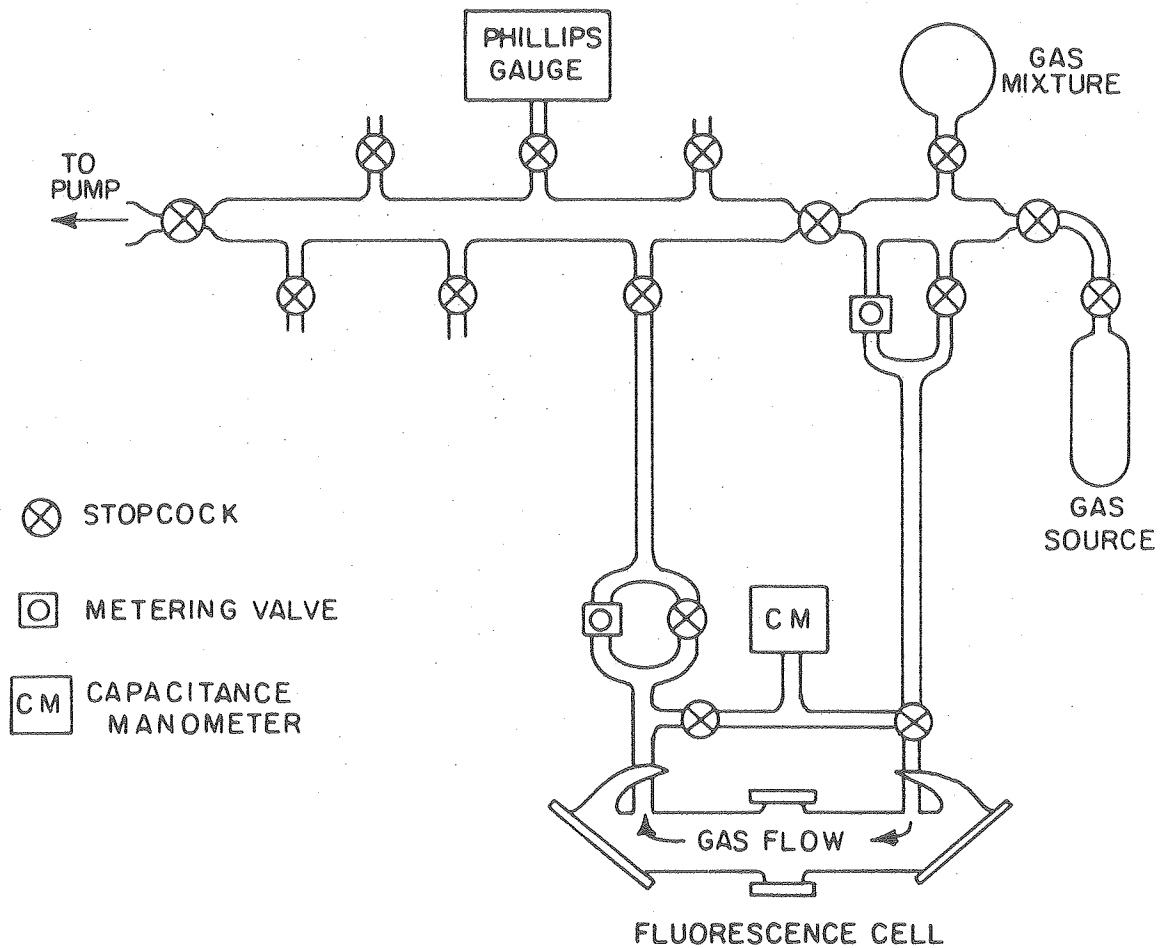
The gas pressure was measured using a capacitance manometer (Validyne DP7) coupled to a carrier demodulator (Validyne CD15) sensitive in the pressure range 0.05 to 5.0 torr. The manometer was connected to either side of the fluorescence cell through a system of teflon stopcocks. Figure 8 shows a schematic of the vacuum manifold, flow system and fluorescence cell.

3. Fluorescence Cell

Figure 8 shows a schematic of the fluorescence cell which was made out of glass tubing 25 cm long and 2.5 cm in diameter. Two quartz flats were sealed at Brewster's angles to the ends with epoxy resin (Torr Seal, Varian, Palo Alto), and two salt windows were similarly sealed on opposite sides of the center of the cell for infrared fluorescence transmission. Opposite to the quartz windows two Wood's horns served as traps for Ultraviolet scattered light.

The cell length was chosen to allow for multiple passes of the UV laser beam without introducing an effective delay of the laser pulse upon repeated reflections through the cell.

Figure 8. Schematic of the vacuum line and gas flow system used.
The fluorescence cell is also shown.



XBL 788-5615

Fig. 8.

H. GAS PREPARATION

All gases used for photolysis were prepared through a system of two traps while under continuous pumping. The first trap was normally kept at dry ice temperature in order to trap water vapor, while the second was used to collect the gas under preparation at liquid nitrogen temperature. After preparation, the gas was distilled from a methanol or n-butanol slush cooled by liquid nitrogen into a trap at liquid nitrogen temperature. The procedure was repeated twice, and the gas was finally stored at liquid nitrogen temperature.

Prior to each photolysis, the gas was warmed up to a temperature just above the melting point and maintained at that temperature throughout. (Normally, a methanol or n-butanol slush cooled with liquid N_2 was used for this purpose).

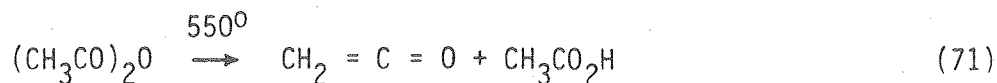
1. Formaldehyde

Three isotopic species of formaldehyde, namely, H_2CO , $HDCO$, and D_2CO were prepared according to the procedure described by Spence and Wild⁹⁴ (the same procedure mentioned above). In all cases, para-formaldehyde, in powder form or as flakes, was left under vacuum overnight, then heated to just above its melting point ($130^\circ C$ for H_2CO , $180^\circ C$ for $HDCO$, and $210^\circ C$ for D_2CO), and the gaseous monomer was finally prepared as above. The polymer of H_2CO was purchased from Matheson Coleman and Bell Company (Cincinnati, Ohio) where as those of $HDCO$ and D_2CO were supplied by Merck Sharp and Dohme Limited (Montreal, Canada), with purity better than 95% each.

2. Ketene ($\text{CH}_2 = \text{C} = \text{O}$)

Ketene was prepared from acetic anhydride by pyrolysis at 550°C .⁹⁵ The apparatus was constructed from a 250 cm^3 round flask sealed through a teflon stopcock to 1 meter long quartz tubing which was connected to the system of two traps mentioned above through an O-ring joint. A nichrome wire (20-gauge) was wound around the quartz tubing to an effective length of 80 cm, and then covered with glass wool for insulation. A variac provided the voltage source (90 V). Temperature was measured using a chromel-Alumel thermocouple (28-gauge).

The procedure consisted of introducing the acetic anhydride liquid into the flask and leaving it to outgas under vacuum for a couple of hours. The electric oven was then heated to 550°C followed by a slow distillation of acetic anhydride at 130°C using a heating mantle. Acetic anhydride decomposes into ketene and acetic acid according to the following equation



After preparation, the ketene monomer was distilled twice from an n-pentane slush to a liquid nitrogen trap and finally stored in liquid nitrogen.

3. Acrolein ($\text{CH}_2 = \text{CHCHO}$)

Acrolein was prepared from a hydroquinone-stabilized sample furnished by Aldrich Chemical Company. The mixture was heated to 55°C thus distilling the vapor into the same system of traps described before. Acrolein vapor was then distilled twice as in the case of ketene and finally stored at liquid nitrogen temperature.

4. Propynal ($\text{CH} \equiv \text{CCHO}$)

A propynal sample was obtained from Professor J. Robert Huber from the Department of Chemistry, University of Konstanz, West Germany. This is a yellow liquid (B.P. 55°C) usually prepared from propargyl alcohol through chromic acid oxidation, a method described by Wille and Safer.⁹⁶ Propynal was always stored at liquid nitrogen temperature.

5. Cyclobutanone

Cyclobutanone was obtained from Aldrich Chemical Company as a colorless liquid (B.P. 37°C) and stored under liquid nitrogen. No further purification was attempted aside from outgassing at liquid N_2 temperature.

6. Other Gases

Cis-2-butene (99.9%), carbon monoxide(99.99%), carbon dioxide (99.99%), nitric oxide (99.0%), oxygen (99.99%), He (99.999%), Ar (99.998%), and Xe (99.9%) gases were all furnished by Matheson Gas Products and used without further purification. Hydrogen gas used for the Raman cell was grade A (99.5%) and used as such.

V. EXPERIMENTAL SET UP

Below is a brief description of the experimental setup used to measure the appearance as well as decay rates of photochemical products in formaldehydes and other small carbonyl compounds. It includes an outline of the procedure followed in generating ultraviolet laser light at 354.7, 266 and 299.1 nm. The steps followed in aligning the various optics in order to optimize the fluorescence signal are also mentioned.

1. Set up for Photolysis at 354.7 nm

Figure 9 is a schematic of the optical arrangement used in generating the Nd:YAG third harmonic, its subsequent alignment with the fluorescence cell, and also the detection electronics. The third harmonic was obtained according to the procedure discussed early in this chapter, namely; a KD^*P type I crystal produced the second harmonic at 532 nm, and another KD^*P type II crystal mixed the fundamental with the second harmonic thus generating the third harmonic at 354.7 nm. A 60° quartz prism was used to disperse the three beams, and with the third harmonic isolated, it was reduced in diameter to about 1.5 mm through a telescope. The telescope consisted of two lenses, a positive ($f = 1 \text{ m}$) and a negative lens ($f = -50 \text{ cm}$) placed 50 cm apart. The collimated beam was then directed through the fluorescence cell close to the top of the Brewster windows. The beam was reflected back and fourth through the cell using a system of two right angle quartz prisms as indicated in Figure 9. It should be noted here that in this arrangement for an effective multiple pass of the beam, the prisms should be aligned such that the beam edge barely touches the prism back edge each time so that a better reflection is obtained. As many as 10 passes were possible in the vertical plane with an overall improvement of the fluorescence signal by a factor of 3 to 4.

The power output at the third harmonic was continuously monitored on an oscilloscope using a trigger photodiode. With both frequency doubling and mixing crystals properly angle tuned, the shot-to-shot stability of the third harmonic was typically 5 to 10%. The second

Figure 9. Experimental set up for the Nd:YAG third harmonic.

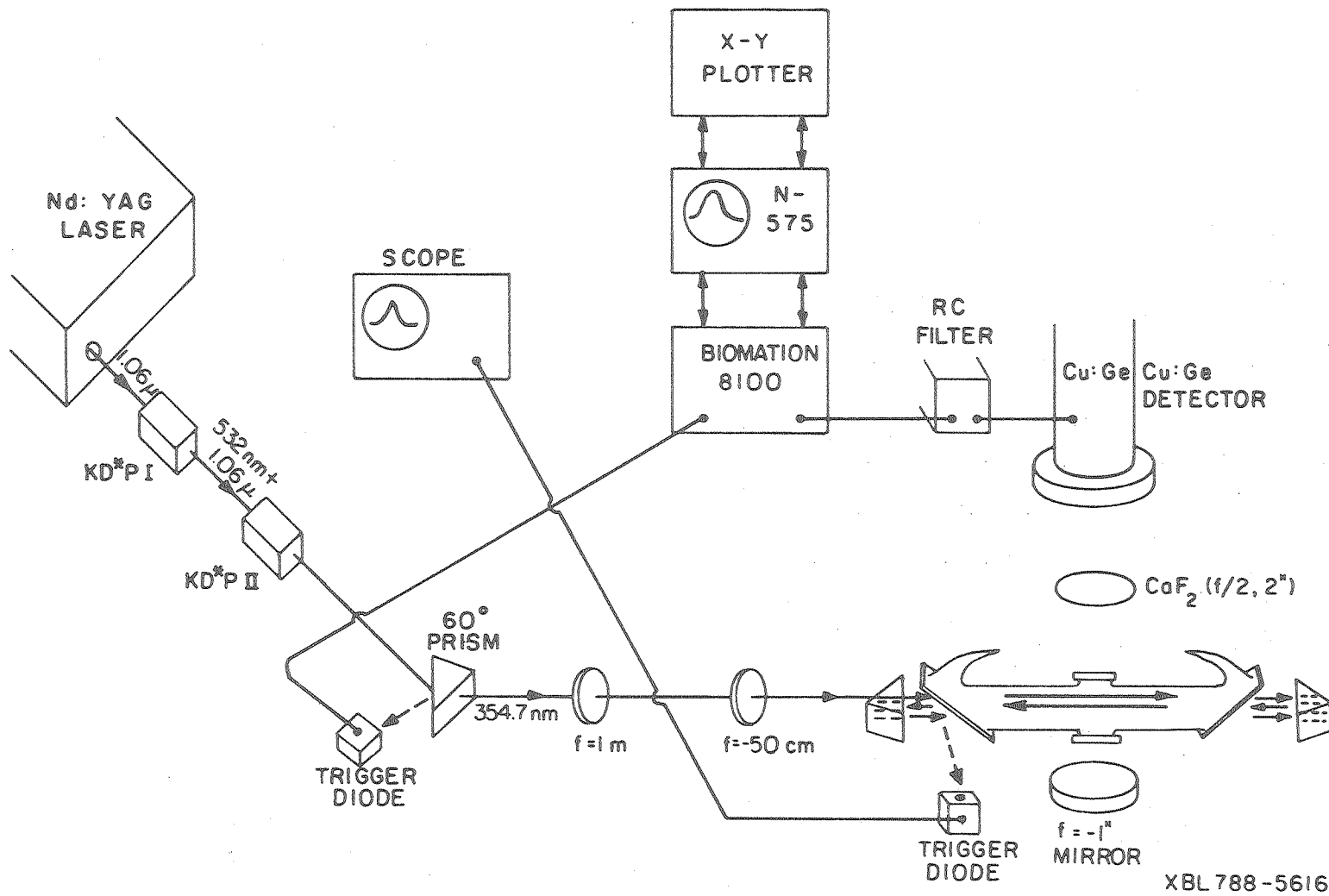


Fig. 9.

harmonic was stable within 3 to 5% whereas the fundamental was better than 1 to 2%.

The photoconductive detector was normally aligned with the center of the fluorescence cell using a He-Ne laser as will be discussed later.

2. Set Up for Photolysis at 266 and 299.1 nm

Here the Nd:YAG second harmonic at 532 nm was obtained through a KD^{*}P type II crystal as described earlier in this chapter. After being dispersed from the fundamental beam through a 60° quartz prism, the second harmonic was frequency doubled through a KDP type I crystal thus generating the fourth harmonic at 266 nm. This was subsequently dispersed from the second harmonic through another prism, collimated and directed through the fluorescence cell.

The ultraviolet source at 299.1 nm was the first Stokes stimulated Raman scattering line in H₂ gas using the fourth harmonic as the laser pump source. Figure 10 is a schematic of the optical layout used to generate these two light sources as described above.

The Raman cell consisted of a stainless steel tube 50 cm long and 1.5 in. in diameter. Two quartz windows 1 in. in diameter and 1 cm thick were sealed to both ends of the cell through O-ring flanges tightened with screws. The cell was filled with H₂ gas at 80 atmospheres after being flushed with H₂ a few times and then aligned with the beam at 266 nm. The beam was reduced in diameter using two positive lenses ($f = 50$ cm and $f = 25$ cm) placed about 24.5 cm apart. This allowed a very little focusing of the beam through the Raman cell with maximum output at the first Stokes line (4.9 mJ/p. It was found

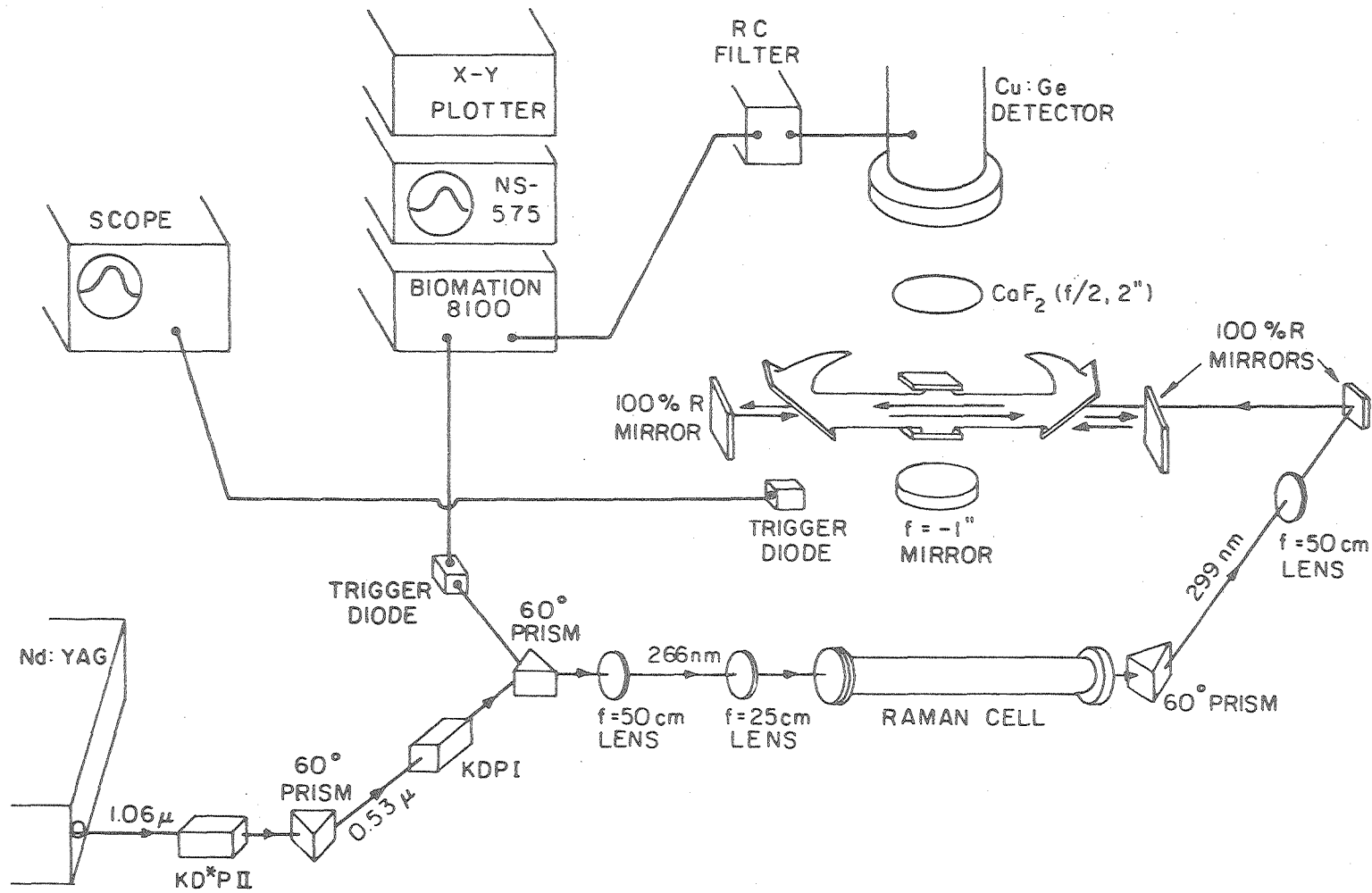
out that in order to get the best shot-to-shot stability at the fourth harmonic and consequently the first Stokes line, the laser should be used at 6 Hz repetition rate. This probably was due to nonsteady thermal heating of the second doubling crystal at higher repetition rates. The power stability was within 10% at best and frequent angle tuning of the second crystal was necessary throughout. A third 60° quartz prism was used to disperse the output at 299.1 nm from the pump beam, and then a quartz lens ($f = 50$ cm) was used to collimate if for the Stokes output comes out normally diverging.

As seen in figure 10, two flat mirrors with 99% reflectivity at 300 nm were used to reflect the beam through the fluorescence cell. It was not possible to use the two-prism arrangement as in figure 9 because it was very difficult to reduce the Raman beam diameter while remaining collimated. The two mirrors allowed about 4 effective passes through the cell.

3. Detector Optical Alignment and Signal Optimization

The Detector (0.3 x 1 cm) was aligned with the center of the fluorescence cell parallel to the beam traversing the cell using a He-Ne laser. A flat mirror placed opposite the bottom salt window at 45° reflected the He-Ne beam through the center of both salt windows onto the center of detector element in the vertical plane. Next a CaF₂ lens 2 in. in diameter ($f/1$) was placed halfway between the detector element and the center of fluorescence cell (4 in. away from each) and then adjusted such that the He-Ne beam traversed the same path. Another concave aluminum mirror 2 in. in diameter ($f/1$) was placed facing the lower salt window 2 in. away from the center of fluorescence.

Figure 10. Schematic of the experimental set up used in photolysis using the Raman shifted fourth harmonic at 299.1 nm.



XBL 788-5617

Fig. 10.

This lens-mirror combination was necessary to enhance the fluorescence solid angle subtended by the detector for the fluorescence signal was normally very small.

Final signal optimization was done with 5 torr ketene or cyclobutanone flowing through the fluorescence cell. This was done by fine tuning of the CaF_2 lens and aluminum mirror while monitoring the fluorescence signal on a scope.

IV. RESULTS

Experimental data on the appearance and decay rates of carbon monoxide have been obtained following laser photolysis of formaldehyde and some other small carbonyl compounds. Among the carbonyls studied are the three formaldehyde isotopic species: H_2CO , HDCO and D_2CO , and also propynal, acrolein, ketene and cyclobutanone. The pressure dependence of CO appearance rates in H_2CO was also studied as a function of added foreign gases such as He, Ar, Xe and NO. All results presented in this chapter were obtained at room temperature.

A. FORMALDEHYDE

1. H_2CO (354.7 nm)

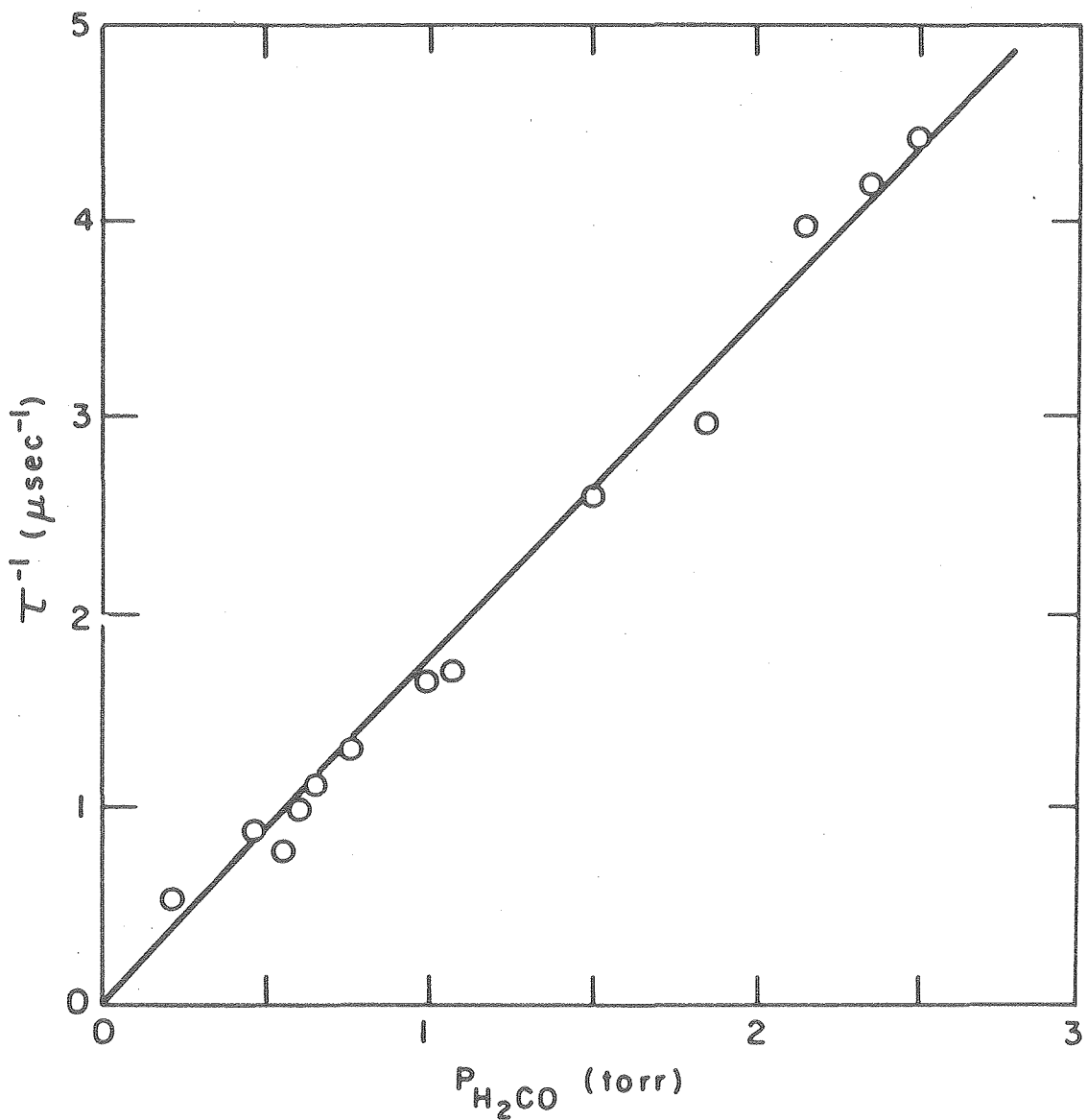
Appearance rates of carbon monoxide produced following photolysis of H_2CO at 354.7 nm were measured as a function of gas pressure and the results are listed in Table I. A plot of those rates against gas pressure is shown in figure 11 where the straight line represents a least-squares fit of data yielding a bimolecular rate constant of $1.72 \pm 0.22 \mu\text{sec}^{-1} \text{ torr}^{-1}$. The uncertainty in the rate thus obtained is calculated from the standard deviation of data about the least-squares fit.

The rates were determined from the variation of CO ($v = 1$) fluorescence intensity as a function of time; the time resolution was always limited by the detector-amplifier system rise time of 100 nsec. The fluorescence detected was essentially that of the first vibrational level of CO. Under the experimental conditions used to obtain those rates, the population of higher vibrational levels was determined to be less than 5% of $v = 1$ as verified by a cold CO gas filter.

Table 1. CO appearance rates in H₂CO following photolysis at 354.7 nm.

$P_{\text{H}_2\text{CO}}$ (torr)	τ^{-1} (μsec^{-1})	$(p\tau)^{-1}$ ($\mu\text{sec}^{-1} \text{ torr}^{-1}$)
0.21	0.42	2.00
0.46	0.88	1.91
0.55	0.79	1.44
0.60	0.98	1.63
0.65	1.12	1.72
0.76	1.32	1.73
1.00	1.65	1.65
1.08	1.69	1.56
1.50	2.60	1.73
1.85	2.94	1.59
2.15	3.96	1.84
2.35	4.18	1.77
2.5	4.40	1.66

Figure 11. CO appearance rates against H₂CO gas pressure measured following photolysis at 354.7 nm. The straight line is a least-squares fit of data yielding a rate constant of $1.72 \pm 0.22 \mu\text{sec}^{-1} \text{ torr}^{-1}$.



XBL 788-5618

Fig. 11.

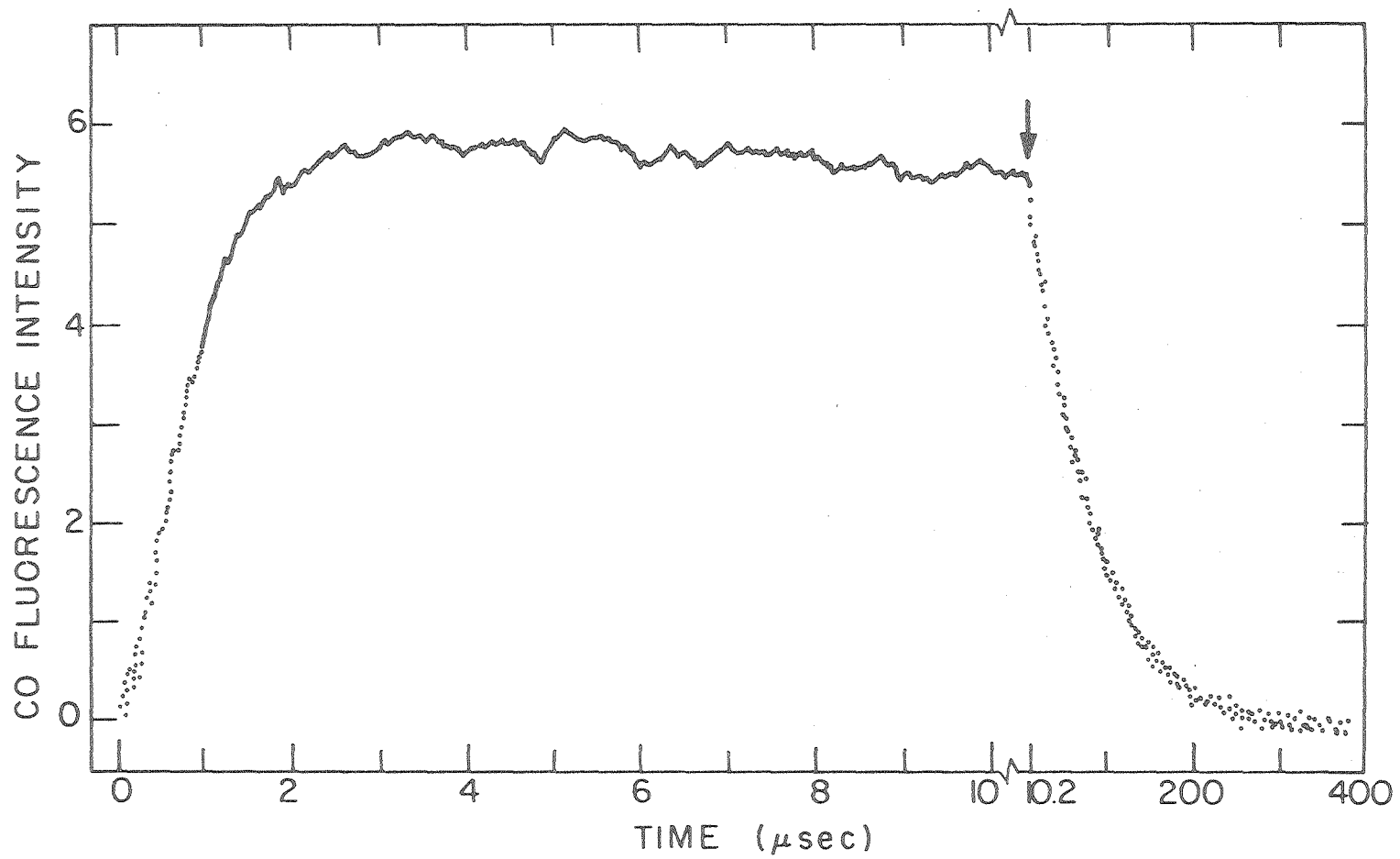
Figure 12 shows a typical CO fluorescence trace obtained for 0.85 torr H₂CO. A blow up of the fluorescence rise portion of the trace is shown in figure 13.

A study of the CO fluorescence intensity dependence on laser power revealed the following:

- (i) The fluorescence intensity varied linearly with laser power up to 24 MW/cm². This is shown in figure 14 for gas pressures of 1.1 and 1.8 torr.
- (ii) At laser powers beyond 25 MW/cm², the fluorescence intensity appeared to vary nonlinearly with laser power. This is also indicated for an H₂CO pressure of 3.09 torr in figure 14. For 31 MW/cm² laser power, the fluorescence intensity was almost twice as much as that for power below 24 MW/cm². No such nonlinearity was found for a gas pressure of 0.675 torr, however.
- (iii) The nonlinearity of fluorescence intensity at higher laser power appears to be due to fluorescence from vibrational levels higher than $v = 1$. This was verified using a cold CO gas filter which completely attenuated $v = 1$ fluorescence. The results for 3.09 torr of H₂CO are shown in figure 15. Here, if we compensate for the 20% attenuation of fluorescence due to reflection and transmission losses through the gas filter, the intensity contribution of higher vibrational levels would account to 50% of the total emission.

An examination of the vibrational level distribution of CO as a function of excitation energy of H₂CO published by Houston²⁵ indicates

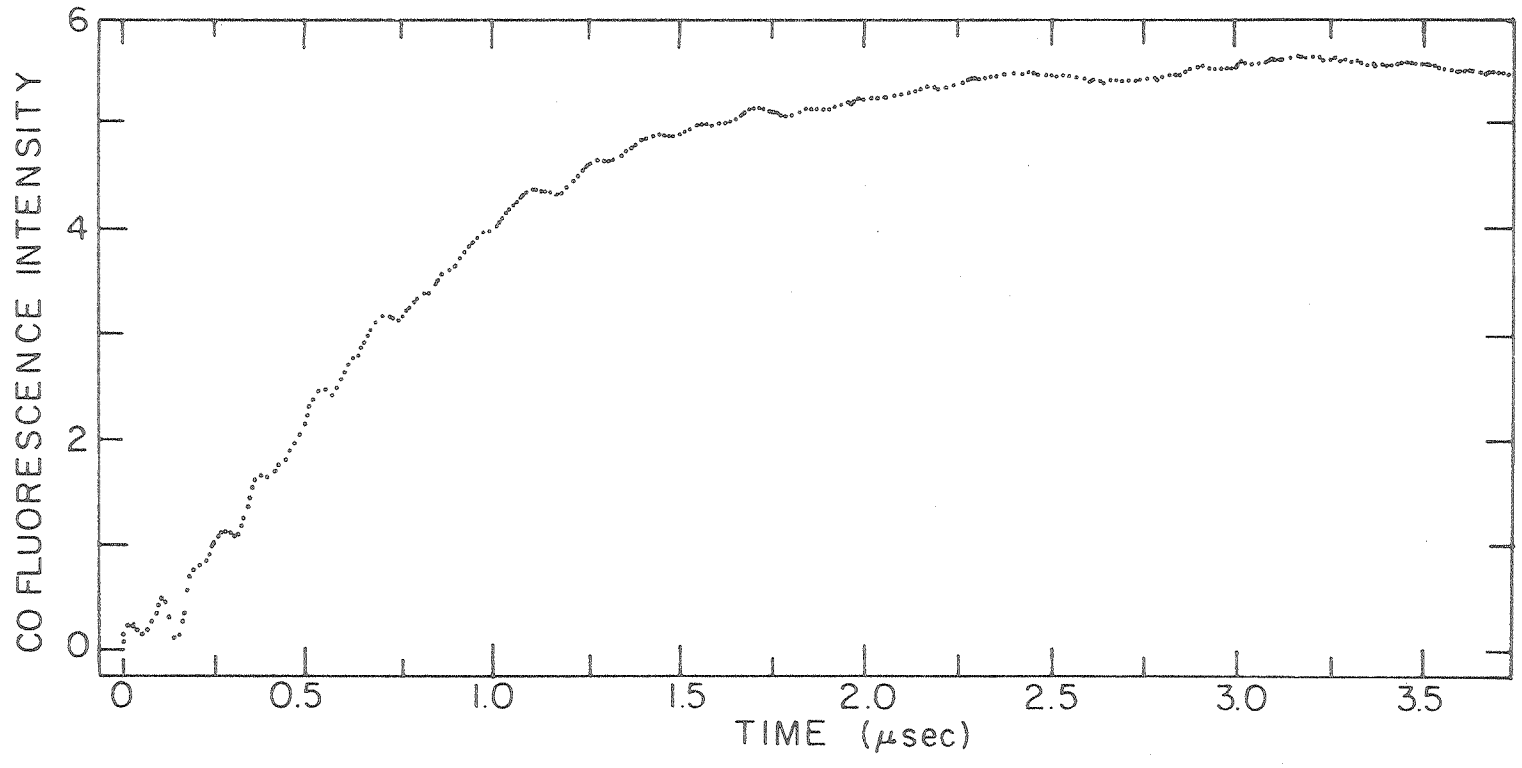
Figure 12. CO fluorescence trace following photolysis of H₂CO at 354.7 nm. The trace is an average of 1024 laser shots for an H₂CO pressure of 0.85 torr.



XBL 788-5619

Fig. 12.

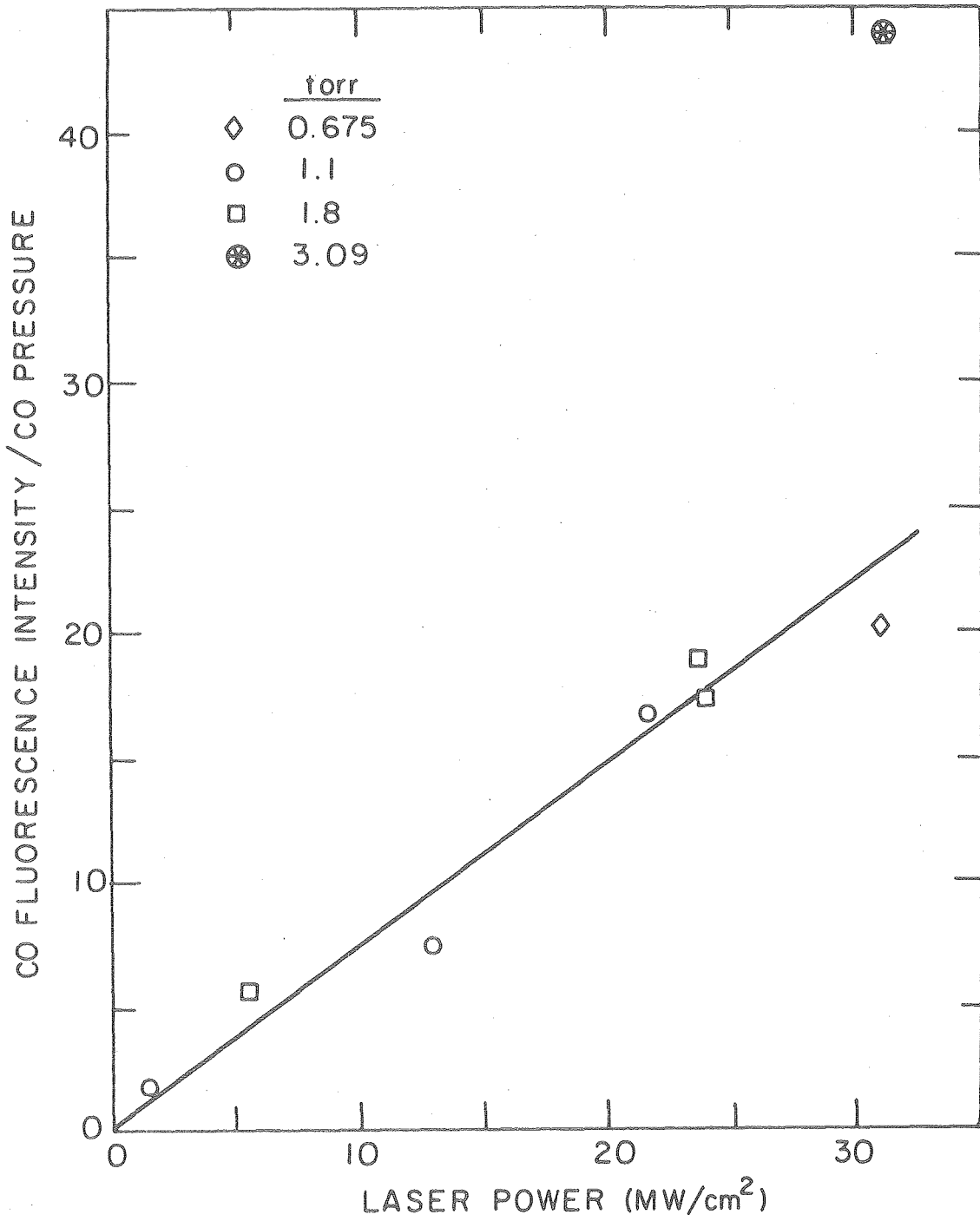
Figure 13. CO fluorescence trace showing the rise portion of the fluorescence signal in H₂CO photolysis at 354.7 nm. The gas sample is the same as in figure 12.



XBL 788-5620

Fig. 13.

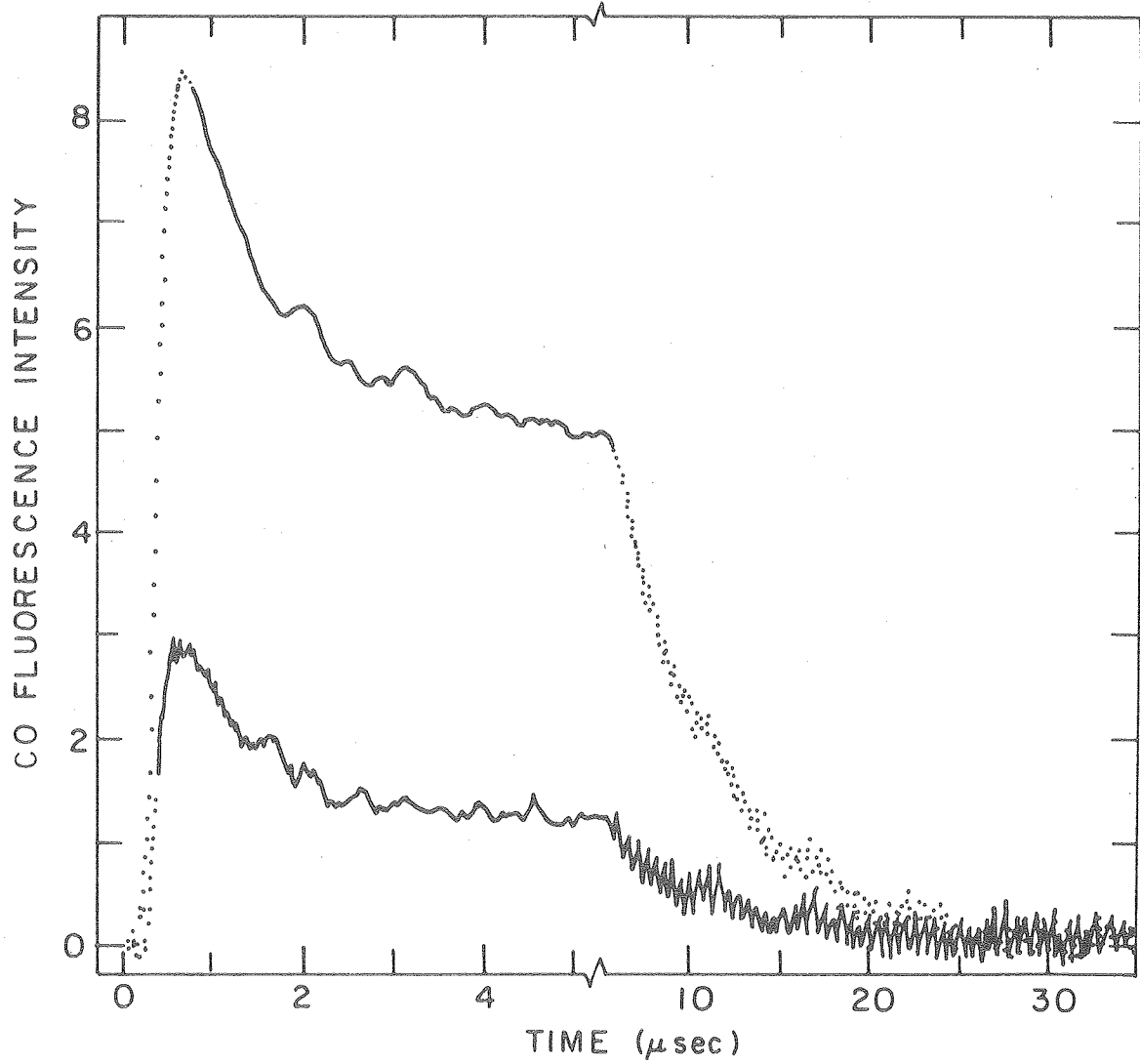
Figure 14. Power dependence of CO fluorescence intensity measured following photolysis of H_2CO at 354.7 nm. Intensities were normalized to 1 torr gas pressure. The actual pressures used are indicated by different symbols as shown in the figure.



XBL788-5621

Fig. 14.

Figure 15. CO fluorescence intensity as a function of time obtained for 3.09 torr H₂CO at 354.7 nm and 31 MW/cm² laser power. Curve (a) represents total fluorescence emission whereas curve (b) is that of $v > 1$ measured through a CO gas filter. Each trace was an average of 512 laser shots.



XBL 788-5622

Fig. 15.

that up to the highest excitation energy used at 294 nm, the population of higher vibrational levels of CO ($v = 1$) never exceeds two thirds that of $v = 1$. At the lower excitation energy corresponding to 347.2 nm, the relative population is only one ninth that of $v = 1$. Since the excitation energy used here was still lower at 354.7 nm, one would expect the population of $v > 1$ to be still lower than 10% of that of $v = 1$ as is found for laser powers below 24 MW/cm^2 . The fact that the population of $v > 1$ increases substantially at the higher laser powers may therefore indicate two photon excitation of H_2CO . This study could not be pursued further, however, due to the limitation on available laser power and, also, to the difficulty of handling formaldehyde at pressures higher than 5 torr since it tends to polymerize quickly.

The decay rates of CO ($v = 1$) produced following photolysis of H_2CO at 354.7 nm are listed in Table II. A plot of those rates against gas pressure is shown in figure 16 with the straight line representing a least-squares fit for the data. The rate constant thus obtained is $(1.75 \pm 0.32) \times 10^3 \text{ sec}^{-1} \text{ torr}^{-1}$. Figure 17 shows a fluorescence trace obtained for 5.00 torr of H_2CO .

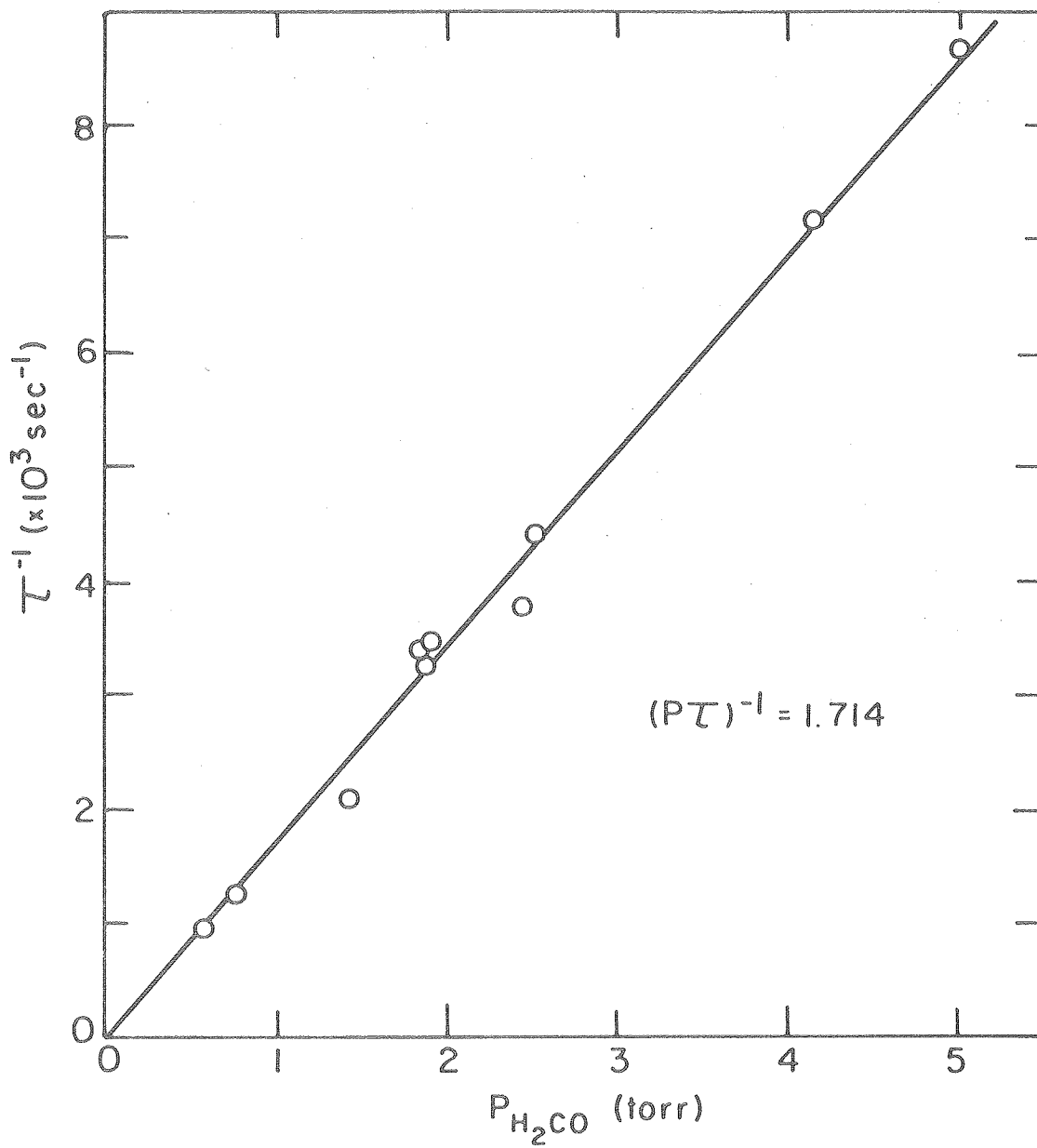
2. H_2CO + Foreign Gases

The effect of foreign gases on the rate of appearance of CO following photolysis at 354.7 nm was examined for He, Ar, Xe and NO. The appearance rates were measured for a fixed pressure of H_2CO and variable pressure of the foreign gas. The results for He gas are listed in Table III and figure 18 shows a plot of those rates against He

Table II. CO ($v = 1$) decay rates in H₂CO following photolysis at 354.7 nm.

$P_{\text{H}_2\text{CO}}$ (torr)	(τ^{-1}) $\times 10^3 \text{ sec}^{-1}$	$(p_{\tau})^{-1}$ $\times 10^3 \text{ sec}^{-1} \text{ torr}^{-1}$
0.55	0.97	1.76
0.76	1.25	1.65
1.41	2.10	1.49
1.85	3.40	1.84
1.87	3.26	1.74
1.90	3.42	1.81
2.43	3.79	1.56
2.50	4.42	1.77
4.12	7.19	1.75
5.00	8.70	1.74

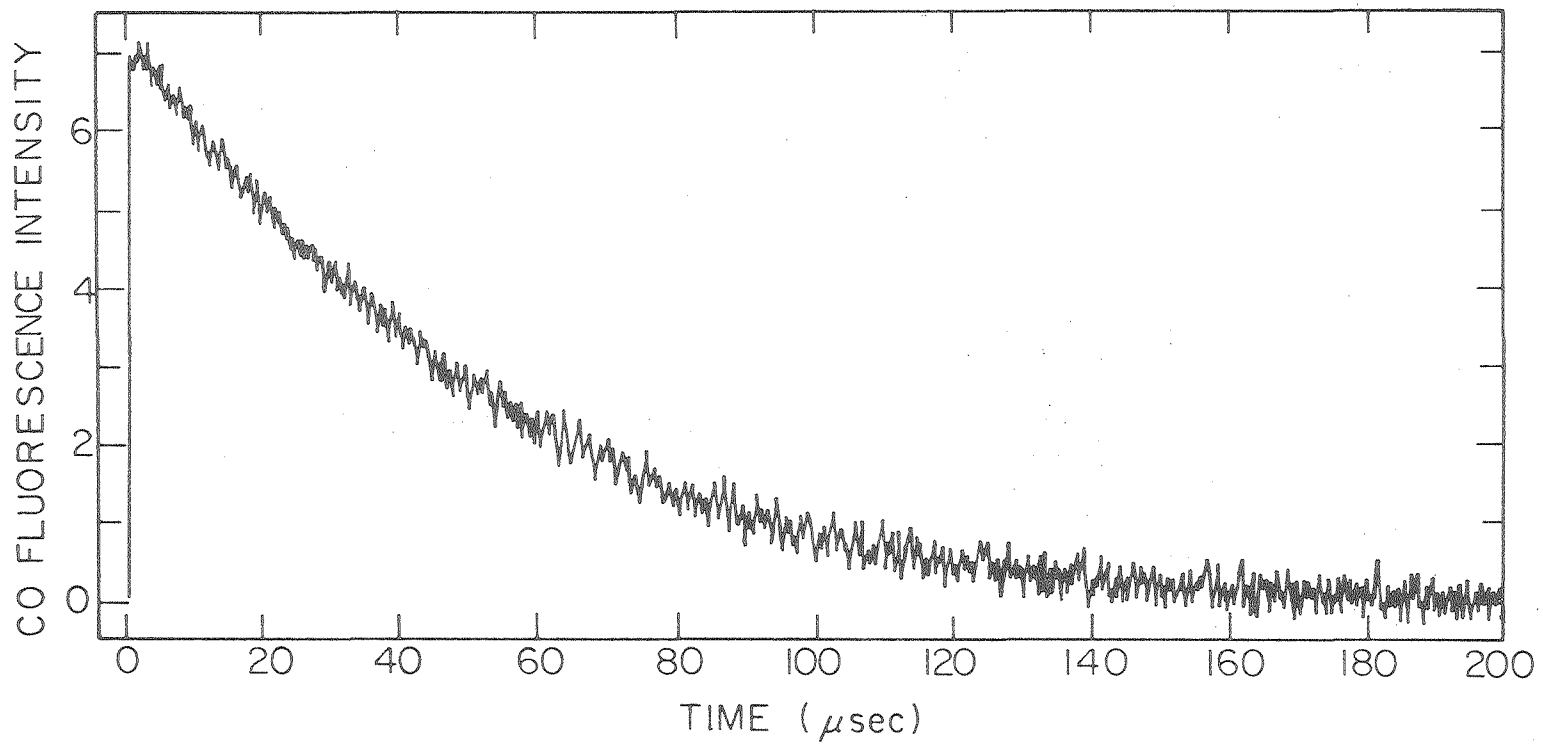
Figure 16. Decay rates of CO ($v = 1$) against H₂CO pressure following photolysis at 354.7 nm. The straight line is a least-squares fit of data yielding a rate constant of $(1.75 \pm 0.32) \times 10^3 \text{ sec}^{-1} \text{ torr}^{-1}$.



XBL788-5623

Fig. 16.

Figure 17. CO ($v = 1$) fluorescence decay trace obtained following photolysis of 5.00 torr H_2CO at 354.7 nm. The trace is an average of 512 laser shots.



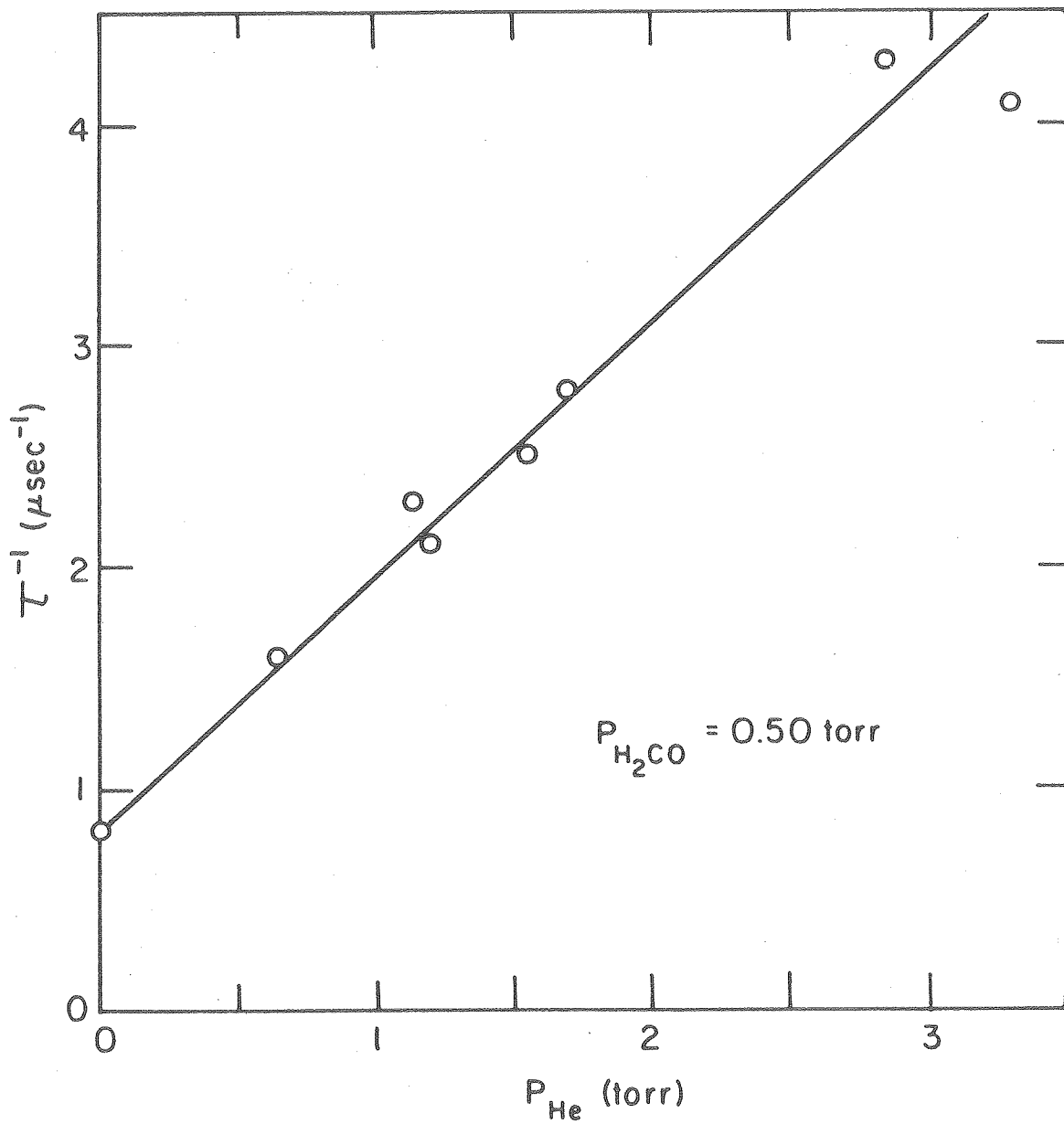
XBL788-5624

Fig. 17.

Table III. CO appearance rates in H₂CO + He gas mixtures following photolysis at 354.7 nm.

P _{H₂CO} (torr)	P _{He} (torr)	(τ ⁻¹) (sec ⁻¹)
0.50	0.65	1.60
0.50	1.15	2.32
0.50	1.20	2.14
0.50	1.55	2.53
0.50	1.70	2.81
0.50	2.85	4.34
0.50	3.30	4.13

Figure 18. CO appearance rates against He gas pressure in H₂CO + He gas mixtures containing 0.50 torr H₂CO. Photolysis wavelength was 354.7 nm. The rate constant obtained is $1.04 \pm 0.26 \text{ sec}^{-1} \text{ torr}^{-1}$.



XBL 7 88-5625

Fig. 18.

pressure. From the least-squares fit for data one obtains a rate constant of $1.04 \pm 0.26 \mu\text{sec}^{-1} \text{ torr}^{-1}$.

Table IV lists the results for added Ar gas. A plot of the rates against Ar gas pressure is shown in figure 19. The rate constant obtained from a least-squares fit of data is $1.28 \pm 0.20 \mu\text{sec}^{-1} \text{ torr}^{-1}$.

The appearance rates measured for $\text{H}_2\text{CO} + \text{Xe}$ gas mixtures are listed in Table V. Figure 20 is a plot of the rates against Xe gas pressure yielding a rate constant of $1.45 \pm 0.24 \mu\text{sec}^{-1} \text{ torr}^{-1}$.

The results for $\text{H}_2\text{CO} + \text{NO}$ gas mixtures is listed in Table VI and a plot of the appearance rates against NO gas pressure is shown in figure 21. The data fit a straight line yielding a rate constant of $1.40 \pm 0.48 \mu\text{sec}^{-1} \text{ torr}^{-1}$.

3. H_2CO (299.1 nm)

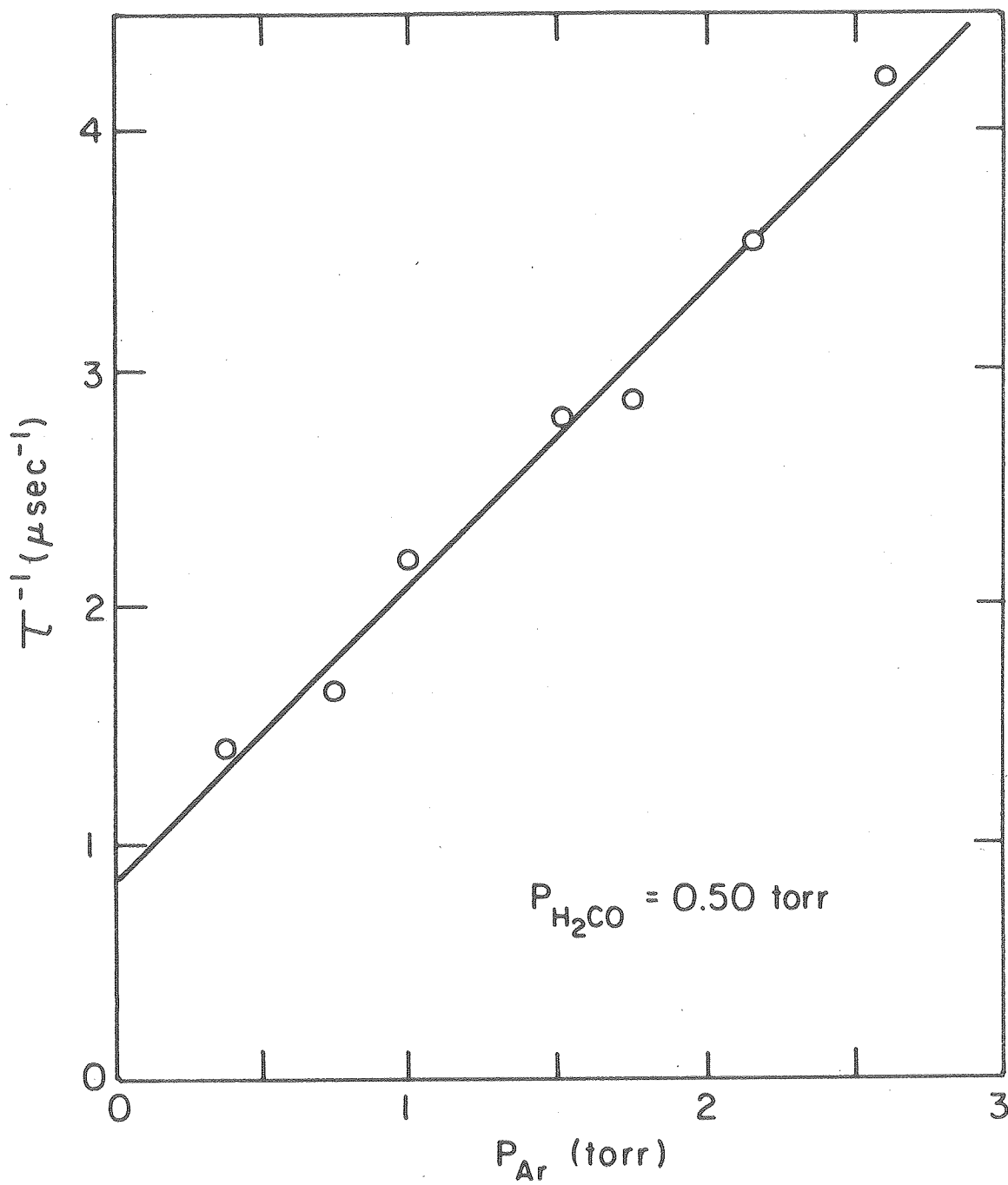
The CO appearance rates measured following photolysis of H_2CO at 299.1 nm were faster than those at 354.7 nm. It was very difficult though to measure the rates below a gas pressure of 0.18 torr due to the relatively low signal-to-noise ratio at the shorter wavelength.

At pressures of 0.30 and 0.18 torr the apparent rates were $16 \pm 7 \mu\text{sec}^{-1} \text{ torr}^{-1}$, and it was not possible to ascertain whether these represent the actual rates or not. This was the case since the times measured were very close to the rise time of the detection system of ~ 120 nsec. So a rate constant of $16 \pm 7 \mu\text{sec}^{-1} \text{ torr}^{-1}$ could only be set as a lower limit at the present stage. Table VII lists the measured rates for the three pressures 0.52, 0.30 and 0.18 torr of H_2CO . The three fluorescence traces obtained for these gas pressures are shown in figure 22 for comparison.

Table IV. CO appearance rates in H₂CO + Ar gas mixtures following photolysis at 354.7 nm.

P _{H₂CO} torr	P _{Ar} torr	(τ ⁻¹) (μsec ⁻¹)
0.50	0.38	1.40
0.50	0.75	1.65
0.50	1.00	2.20
0.50	1.52	2.80
0.50	1.75	2.90
0.50	2.15	3.55
0.50	2.60	4.25

Figure 19. CO appearance rates against Ar gas pressure in H₂CO + Ar gas mixtures containing 0.50 torr H₂CO. Photolysis wavelength was 354.7 nm. The rate constant obtained is $1.28 \pm 0.20 \mu\text{sec}^{-1} \text{ torr}^{-1}$.



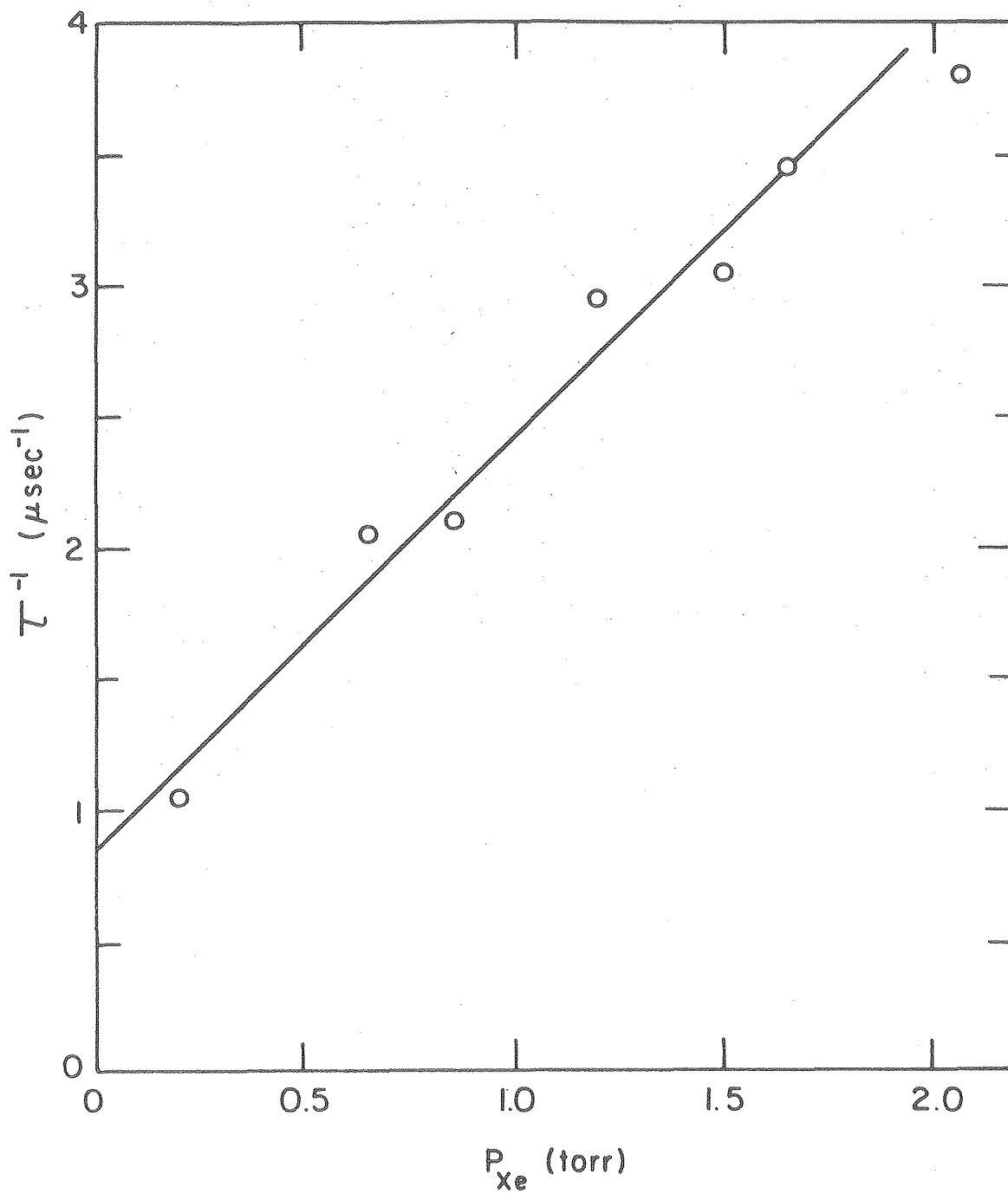
X BL 788- 5626

Fig. 19.

Table V. CO appearance rates in H₂CO + Xe gas mixtures following photolysis at 354.7 nm.

P _{H₂CO} (torr)	P _{Xe} (torr)	τ^{-1} (μsec^{-1})
0.50	0.20	1.05
0.50	0.65	2.05
0.50	0.85	2.10
0.50	1.20	2.95
0.50	1.50	3.05
0.50	1.65	3.45
0.50	2.05	3.75

Figure 20. CO appearance rates against $\text{H}_2\text{CO} + \text{Xe}$ gas mixtures containing 0.50 torr H_2CO . Photolysis wavelength was 354.7 nm. The rate constant obtained is $1.54 \pm 0.24 \mu\text{sec}^{-1} \text{ torr}^{-1}$.



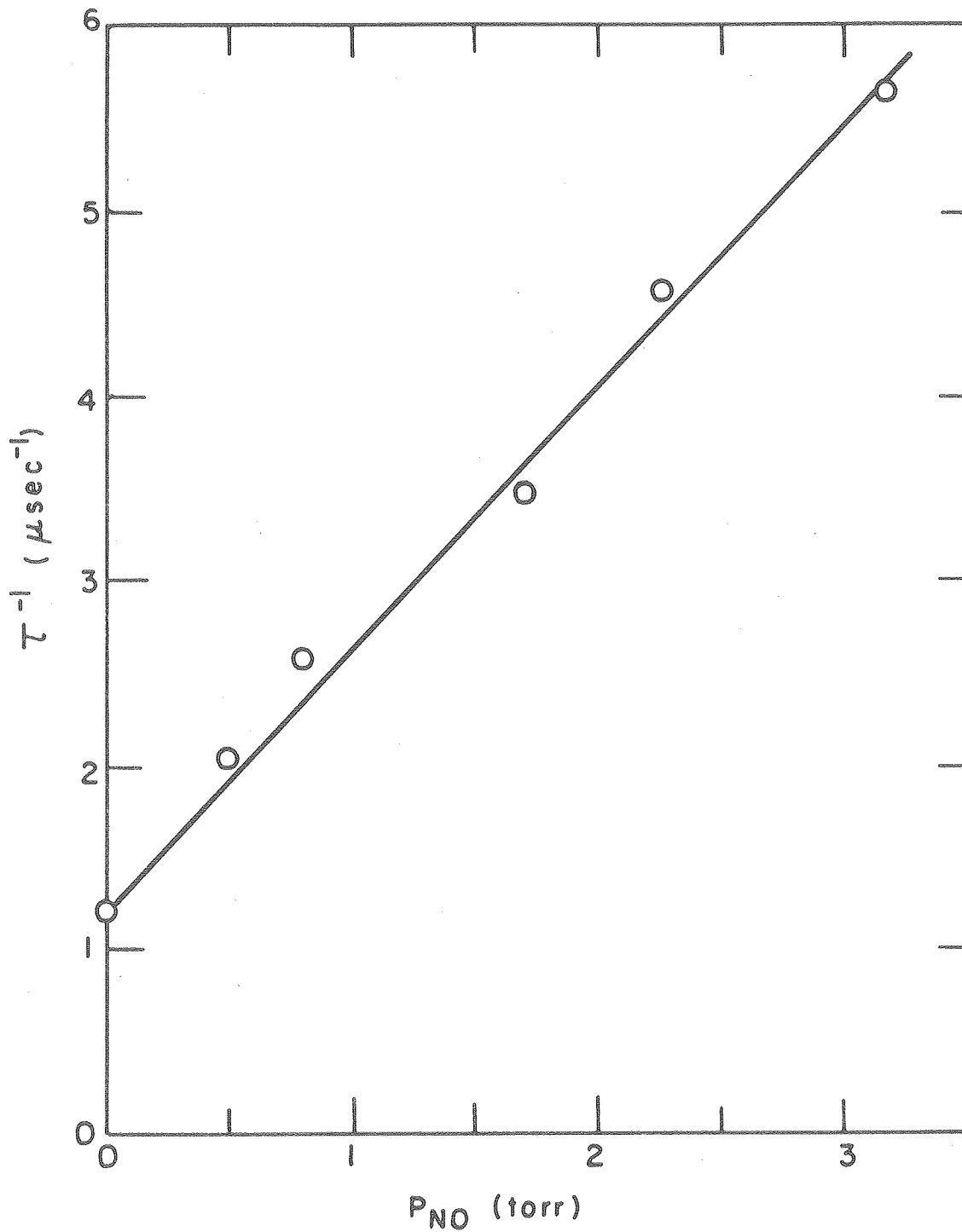
XBL 788-5627

Fig. 20.

Table VI. CO appearance rates in H₂CO + NO gas mixtures following photolysis at 354.7 nm.

P _{H₂CO} (torr)	P _{NO} (torr)	τ^{-1} (μsec^{-1})
0.76	0	1.21
0.76	0.50	2.02
0.76	0.79	2.56
0.76	1.73	3.45
0.76	2.23	4.57
0.76	3.14	5.64

Figure 21. CO appearance rates against NO gas pressure in H₂CO + NO gas mixtures containing 0.76 torr H₂CO. Photolysis wavelength was 354.7 nm. The rate constant obtained is $1.40 \pm 0.48 \mu\text{sec}^{-1} \text{ torr}^{-1}$.



XBL 788-5628

Fig. 21.

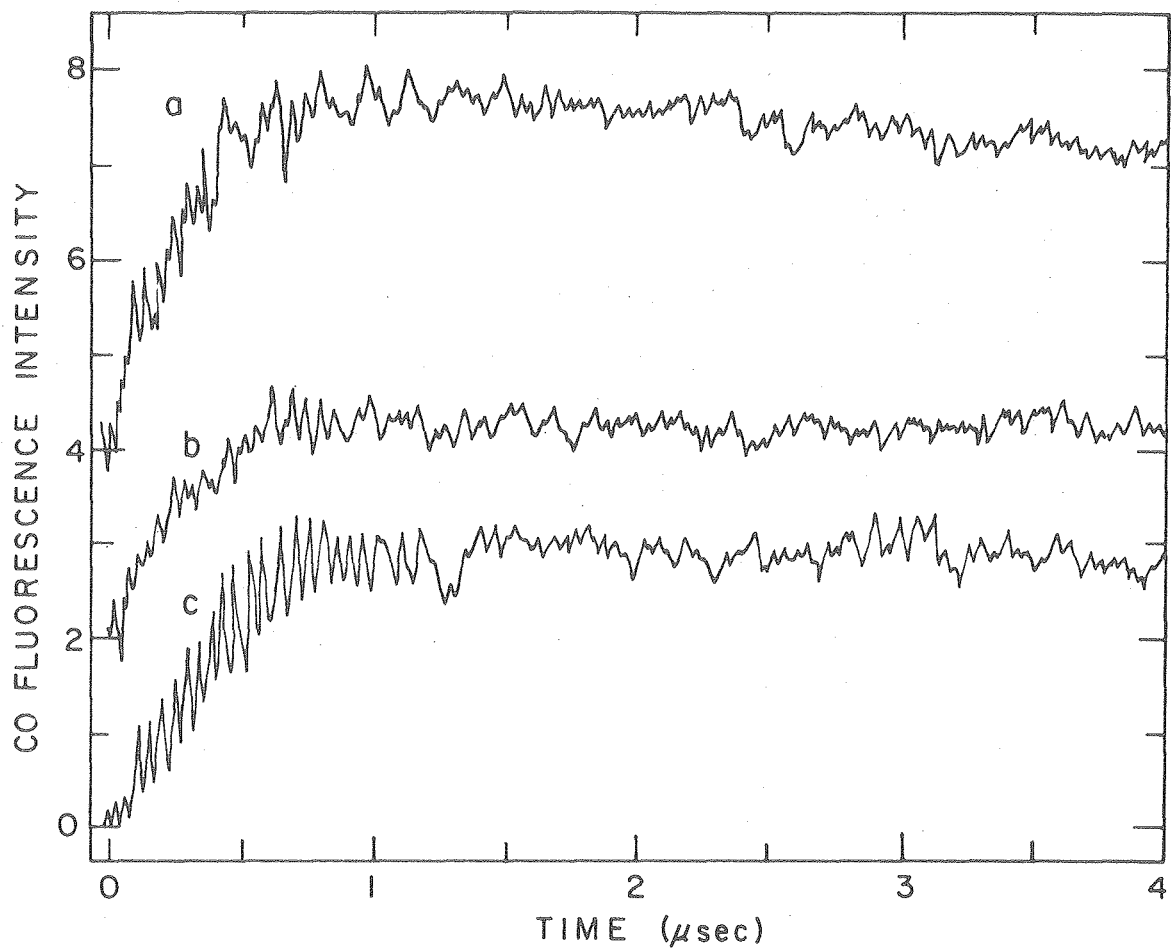
Table VII. CO appearance rates measured following H₂CO photolysis at 299.1 nm.

P _{H₂CO} (torr)	τ^{-1} (μsec^{-1})	$(p\tau)^{-1}$ ($\mu\text{sec}^{-1}\text{ torr}^{-1}$)
0.52	4.2 ± 0.5^a	8 ± 1
0.30	4.2 ± 0.5^a	14 ± 2
0.18	2.8 ± 1.5^b	16 ± 7

^aCO fluorescence rise times measured for 0.52 and 0.30 torr appear to be detector limited. The detector rise time was measured as 120 nsec.

^bCO fluorescence rise time appears to be longer than the detector rise time, but the fluorescence signal was terribly noisy at this low pressure.

Figure 22. CO fluorescence traces following photolysis of H₂CO at 299.1 nm. Curve (a) is a trace obtained for 0.52 torr H₂CO; curve (b) is that of 0.30 torr; and curve (c) is a trace obtained for 0.18 torr. Each trace was an average of 4096 laser shots.



XBL788-5629

Fig. 22.

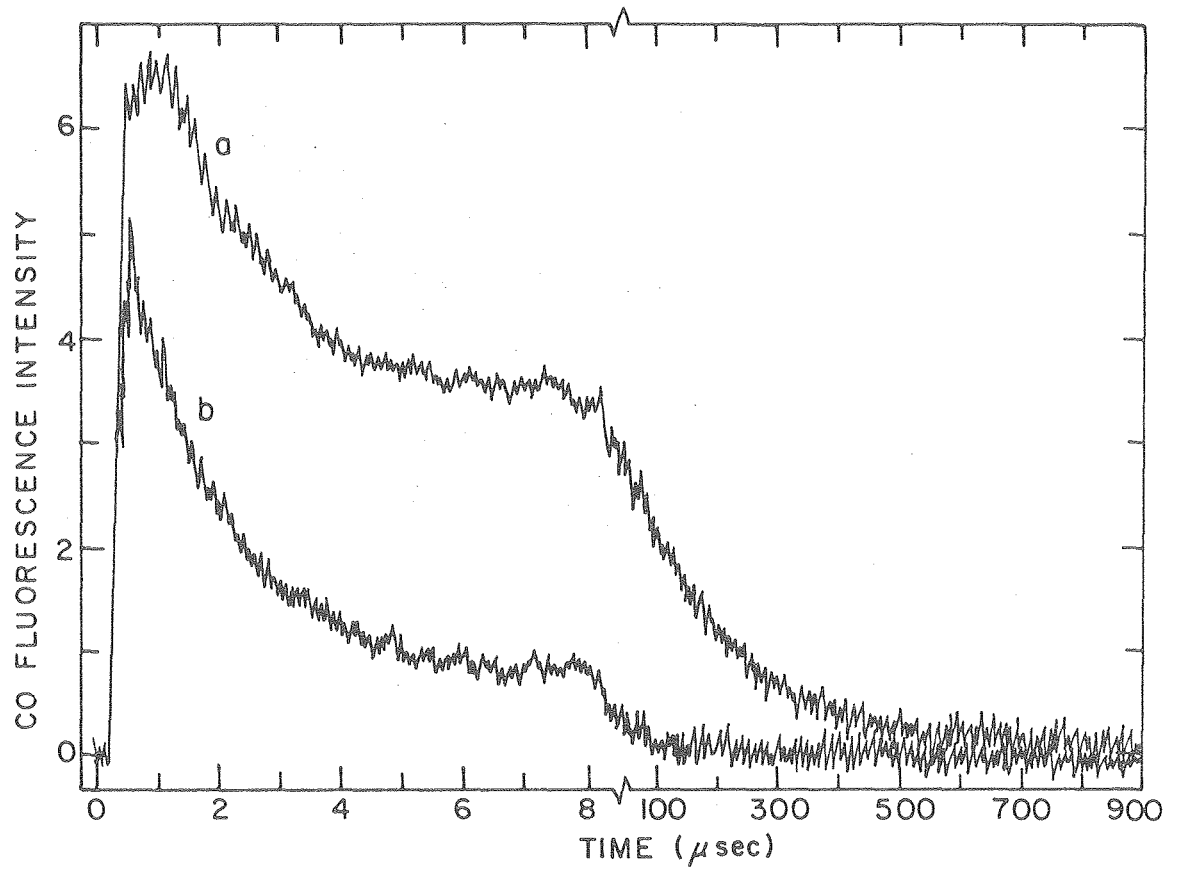
Figure 23. CO fluorescence emission following photolysis of 2.55 torr of H_2CO at 299.1 nm. Curve (a) represents total emission whereas curve (b) is that of CO ($v = 1$) obtained through a cold CO gas filter. Each trace was an average of 1024 laser shots.

The relative fluorescence emission from CO ($v > 1$) to total emission was measured for 2.55 torr H₂CO to be 64%. This is in agreement with Houston²⁵ results of 60% for excitation wavelength at 295.0 nm. Figure 23 shows the two fluorescence traces obtained for 2.55 torr H₂CO which demonstrate the relative emission from CO ($v > 1$) to total emission.

4. D₂CO (354.7 nm)

The CO fluorescence intensity following photolysis of D₂CO at 354.7 nm was extremely low compared with H₂CO. This is apparently due to the low CO quantum yields of 0.1 ± 0.05 in D₂CO compared with 0.71 ± 0.05 in H₂CO measured at 353.5 nm.²⁰ The signal-to-noise ratio did not allow any measurement of appearance rates for pressures below 1.0 torr of D₂CO. The results obtained for the higher pressures are listed in Table VIII giving an approximate rate constant of $0.7 \pm 0.2 \mu\text{sec}^{-1}$ torr.

Figure 24 shows a fluorescence trace obtained for 2.5 torr D₂CO.



XBL 788-5630

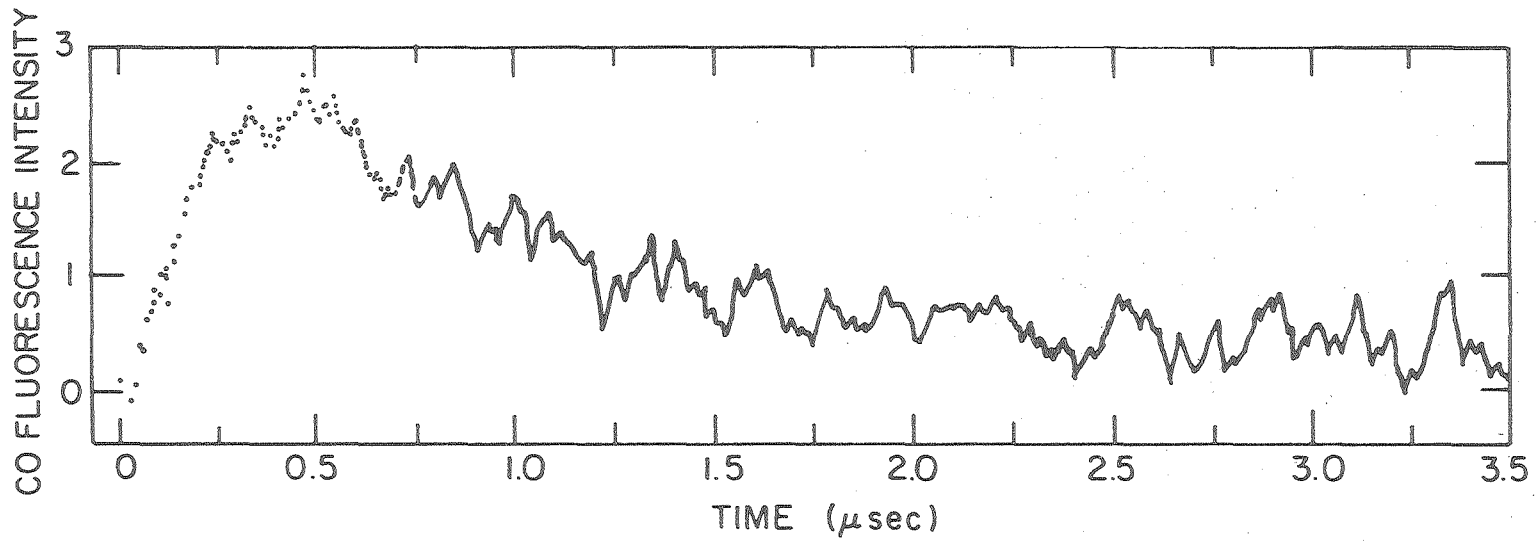
Fig. 23.

Table VIII. CO appearance rates following photolysis of D₂CO at 354.7 nm.

P _{D₂CO} (torr)	τ^{-1} (μsec^{-1})	$(p\tau)^{-1}$ ($\mu\text{sec}^{-1} \text{ torr}^{-1}$)
1.0	0.71 \pm 0.2	0.7 \pm 0.2
2.5	1.70 \pm 0.2	0.7 \pm 0.2
5.0	4.54 \pm 0.2 ^a	0.9 \pm 0.2

^aCO fluorescence rise time obtained for 5.0 torr D₂CO is very close to detector rise time. So a rate constant of 0.9 appears to be highly uncertain.

Figure 24. CO fluorescence trace following photolysis of 2.5 torr D_2CO at 354.7 nm. The trace is an average of 2048 laser shots.



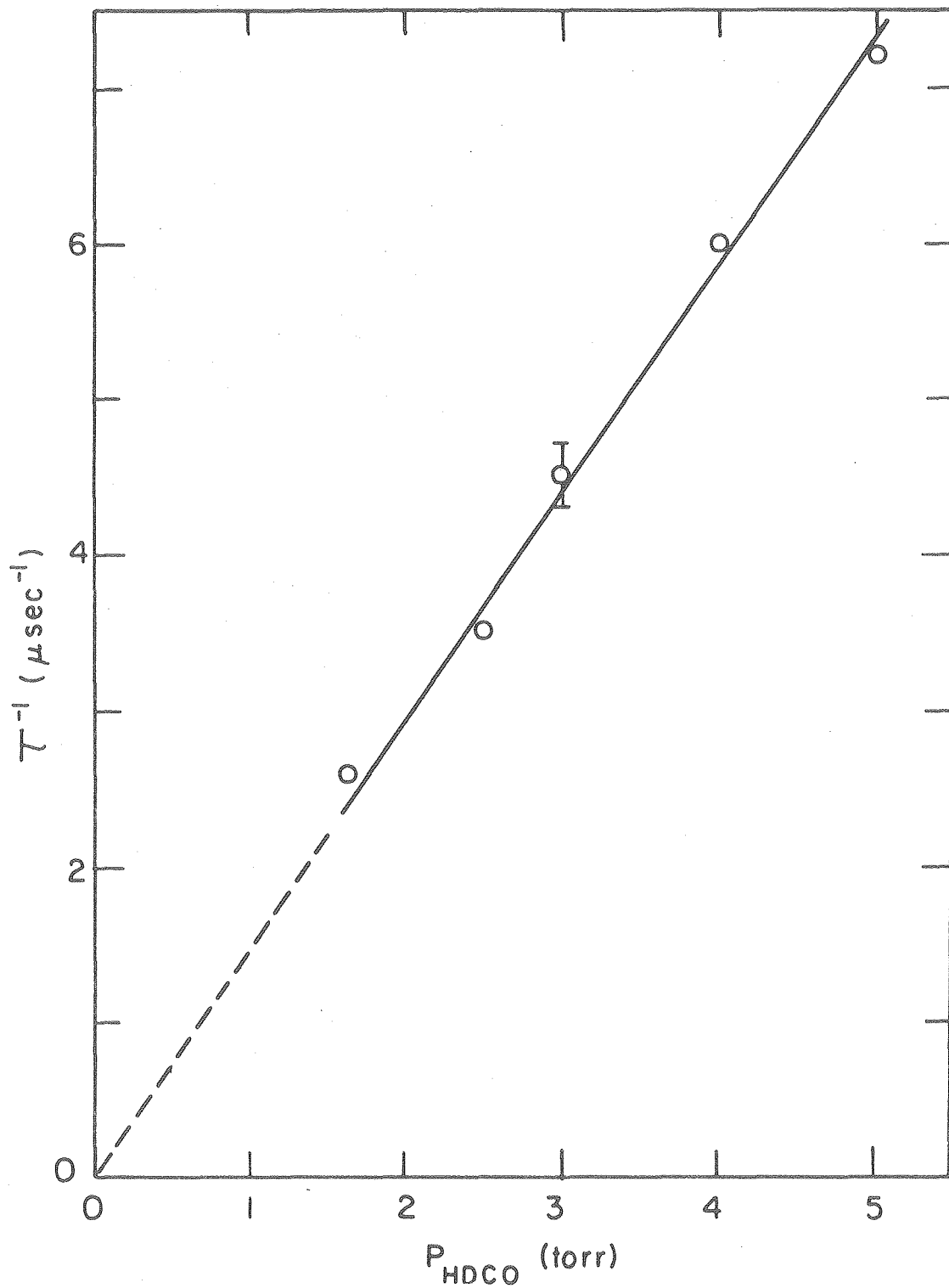
XBL 788-5631

Fig. 24.

Table IX. CO appearance rates following photolysis of HDCO at 354.7 nm.

P_{HDCO} (torr)	τ^{-1} ($\mu \text{ sec}^{-1}$)	$(p\tau)^{-1}$ ($\mu \text{ sec}^{-1} \text{ torr}^{-1}$)
1.65	2.6	1.6
2.50	3.5	1.4
3.01	4.5	1.5
4.01	6.0	1.5
5.00	7.2	1.4

Figure 26. CO appearance rates against HDCO gas pressure following photolysis at 354.7 nm. The straight line represents a least-squares fit of data yielding a rate constant of $1.41 \pm 0.41 \mu\text{sec}^{-1} \text{ torr}^{-1}$.



XBL 788-5632

Fig. 26.

5. HDCO (354.7 nm)

Table IX lists the CO appearance rates measured following photolysis of HDCO at 354.7 nm. The results are plotted against HDCO gas pressure in figure 26 yielding a rate constant of $1.41 \pm 0.41 \mu\text{sec}^{-1} \text{ torr}^{-1}$. A CO fluorescence trace obtained for 1.65 torr HDCO is also shown in figure 27.

The decay rates of CO ($v = 1$) in HDCO are listed in Table X. Figure 28 is a plot of the rates against HDCO gas pressure. A least squares fit of data yields a decay rate constant of $(7.3 \pm 0.3) \times 10^4 \text{ sec}^{-1} \text{ torr}^{-1}$. A fluorescence trace showing the decay of CO ($v = 1$) in 5.0 torr HDCO is given in figure 29.

B. PROPYNAL ($\text{CH} \equiv \text{CCHO}$)

Photolysis of propynal at 354.7 nm produced no measurable CO fluorescence signal at pressures below 0.40 torr. The single shot signal-to-noise ratio was typically ~ 0.03 at 1 torr gas pressure. At 0.40 torr the CO appearance rate was certainly detector limited and amounted to 120 nsec. One can therefore set a lower limit of $\sim 20 \mu\text{sec}^{-1} \text{ torr}^{-1}$ for propynal.

Figure 30 shows a CO fluorescence trace of the rise portion obtained for 0.40 torr at 354.7 nm.

C. ACROLEIN ($\text{CH}_2 = \text{CHCHO}$)

CO appearance rates following photolysis of acrolein at 354.7 nm were also detector limited. The lowest pressure for which the rate was measured was 0.089 torr and appeared to have a rise time of ~ 150 nsec. A lower limit of $\sim 75 \mu\text{sec}^{-1} \text{ torr}^{-1}$ could only be set for the rate constant in acrolein.

Figure 27. CO fluorescence trace showing the rise of fluorescence signal following photolysis of 1.65 torr HDCO at 354.7 nm. The trace is an average of 4096 laser shots.

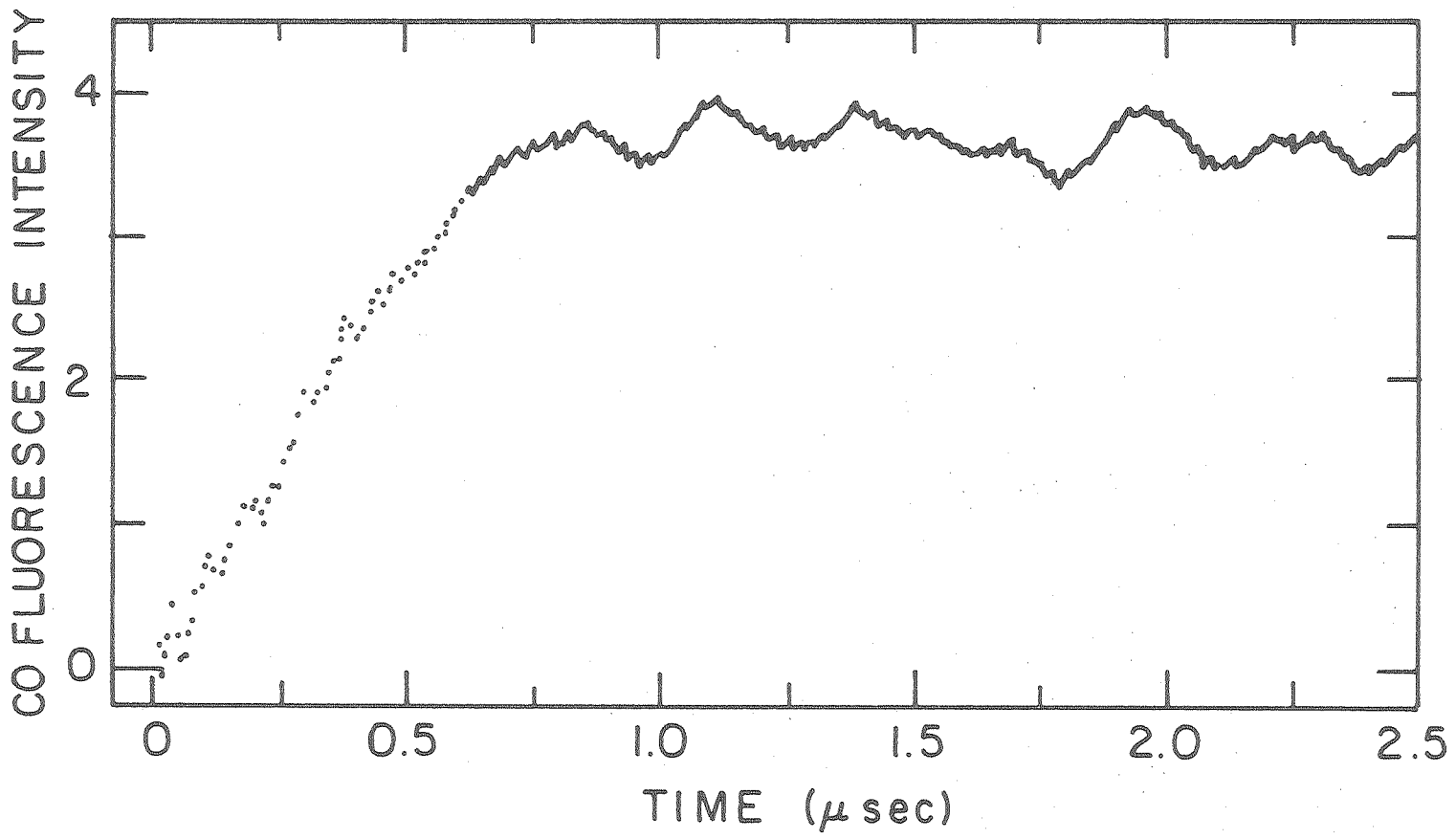


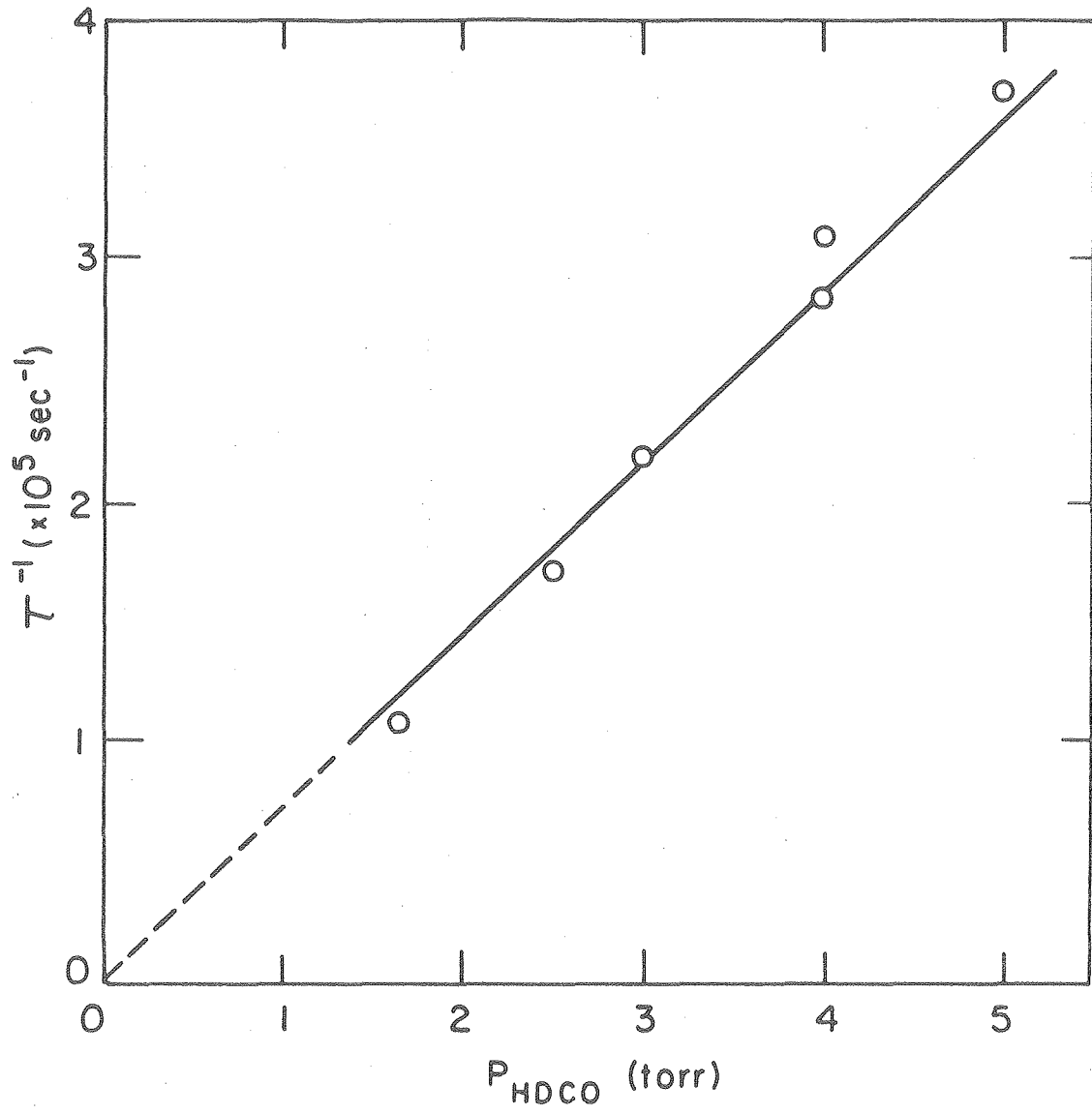
Fig. 27.

XBL788-5633

Table X. CO ($v = 1$) decay rates in HDCO gas following photolysis at 354.7 nm.

P_{HDCO} (torr)	τ^{-1} ($\times 10^5 \text{ sec}^{-1}$)	$(p\tau)^{-1}$ ($\times 10^4 \text{ sec}^{-1} \text{ torr}^{-1}$)
1.65	1.1	6.6
2.50	1.7	6.9
3.01	2.2	7.2
4.01	3.1	7.7
4.03	2.8	7.0
5.00	3.7	7.4

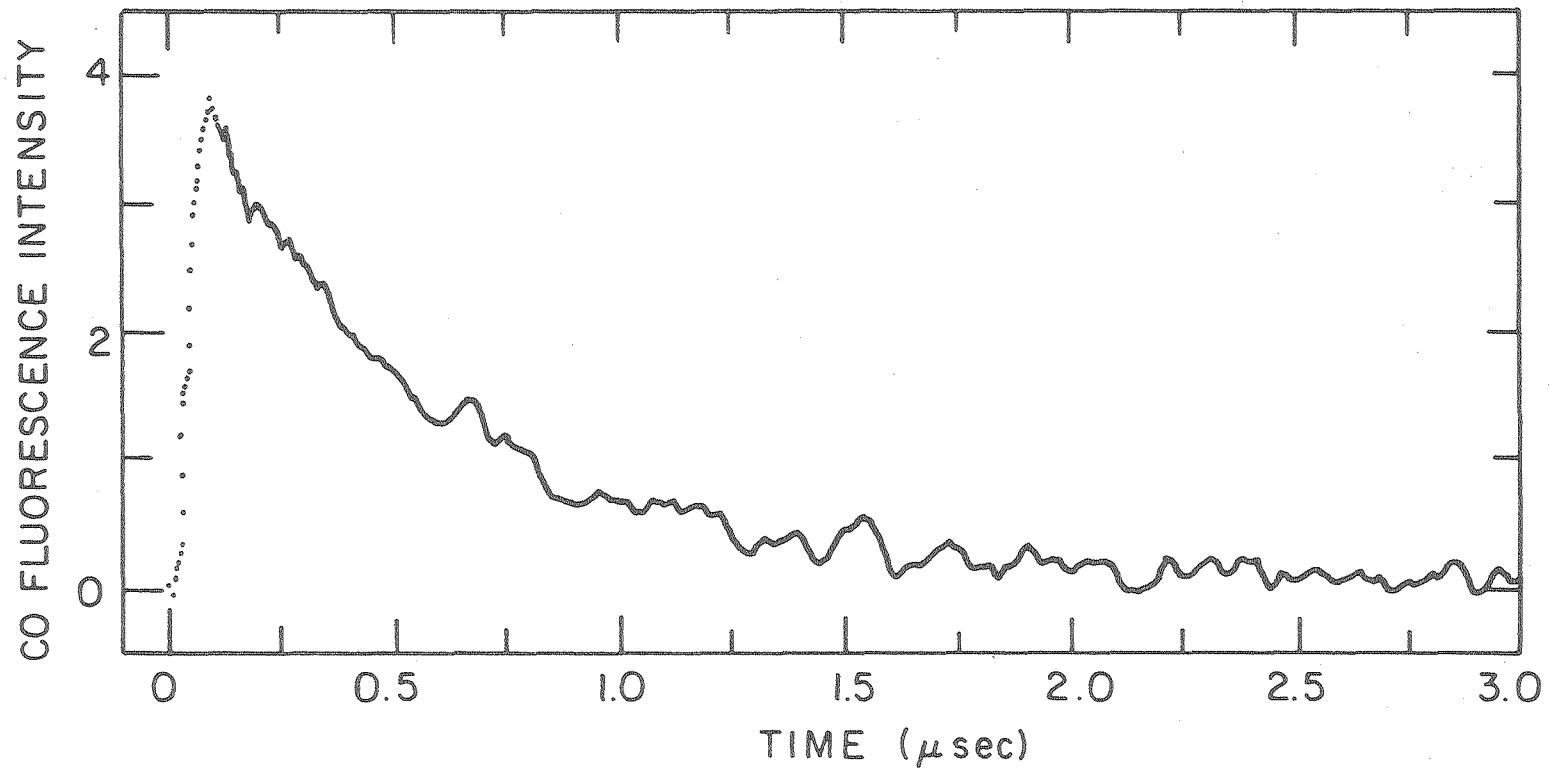
Figure 28. CO ($v = 1$) decay rates against HDCO gas pressure following photolysis at 354.7 nm. The straight line represent a least-squares fit of data yielding a rate constant of $(7.3 \pm 0.3) \times 10^4 \text{ sec}^{-1} \text{ torr}^{-1}$.



XBL 788 - 5634

Fig. 28.

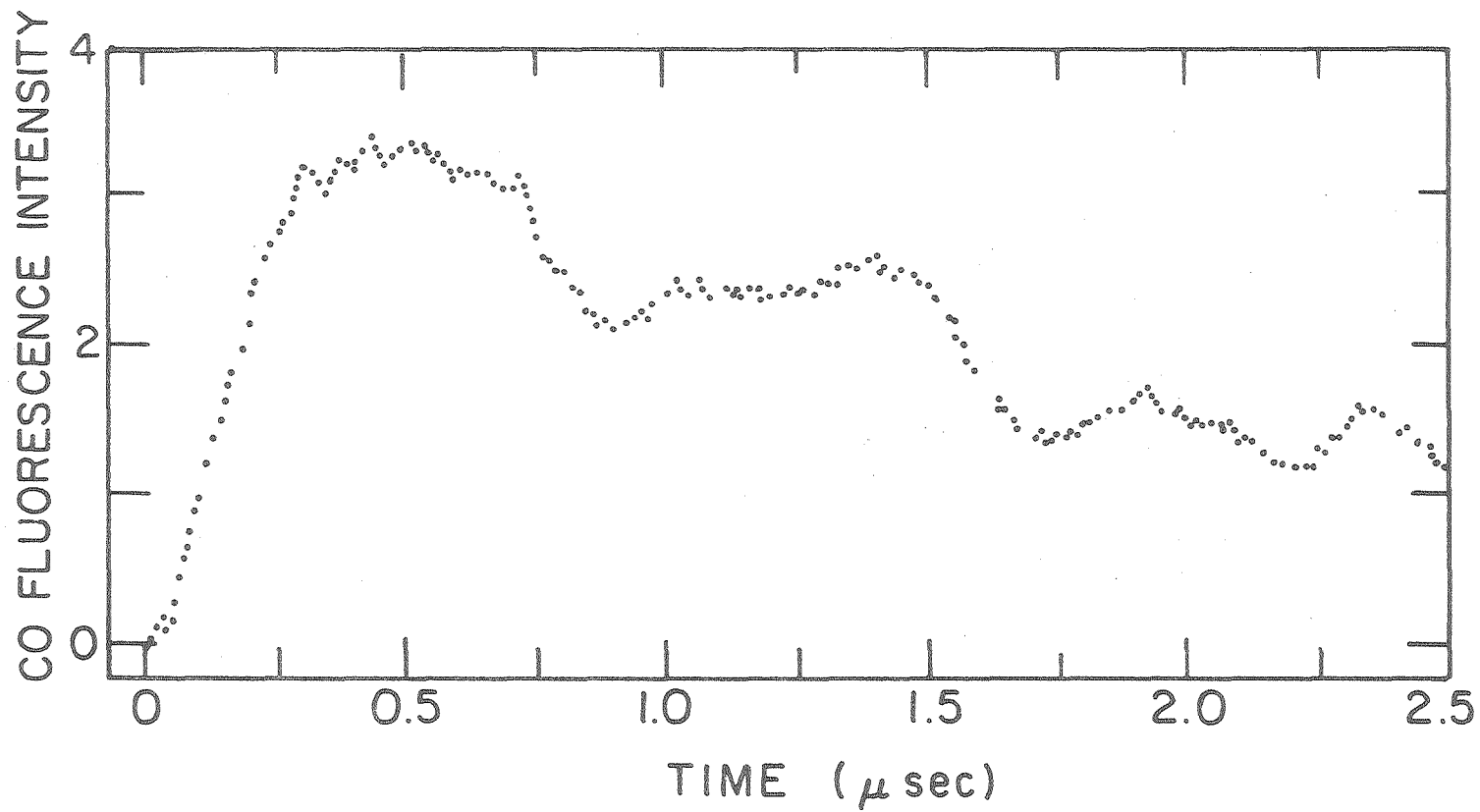
Figure 29. CO ($v = 1$) fluorescence decay trace obtained following photolysis of 5.00 torr HDCO at 354.7 nm. The trace is an average of 2048 laser shots.



XBL 788-5635

Fig. 29.

Figure 30. CO fluorescence trace showing the rise of fluorescence signal following photolysis of 0.40 torr propynal at 354.7 nm. The trace is an average of 2048 laser shots.



XBL 788-5636

Fig. 30.

A CO fluorescence trace showing the rise of fluorescence signal is given in figure 31 for 0.089 torr acrolein.

Table XI lists the data obtained for CO ($v = 1$) decay rates and a plot of those rates against gas pressure is shown in figure 32. A least-squares fit of data yields a rate constant of $2.02 \pm 0.22 \mu\text{sec}^{-1} \text{ torr}^{-1}$. Figure 33 shows a CO ($v = 1$) fluorescence decay trace obtained for 0.217 torr of acrolein.

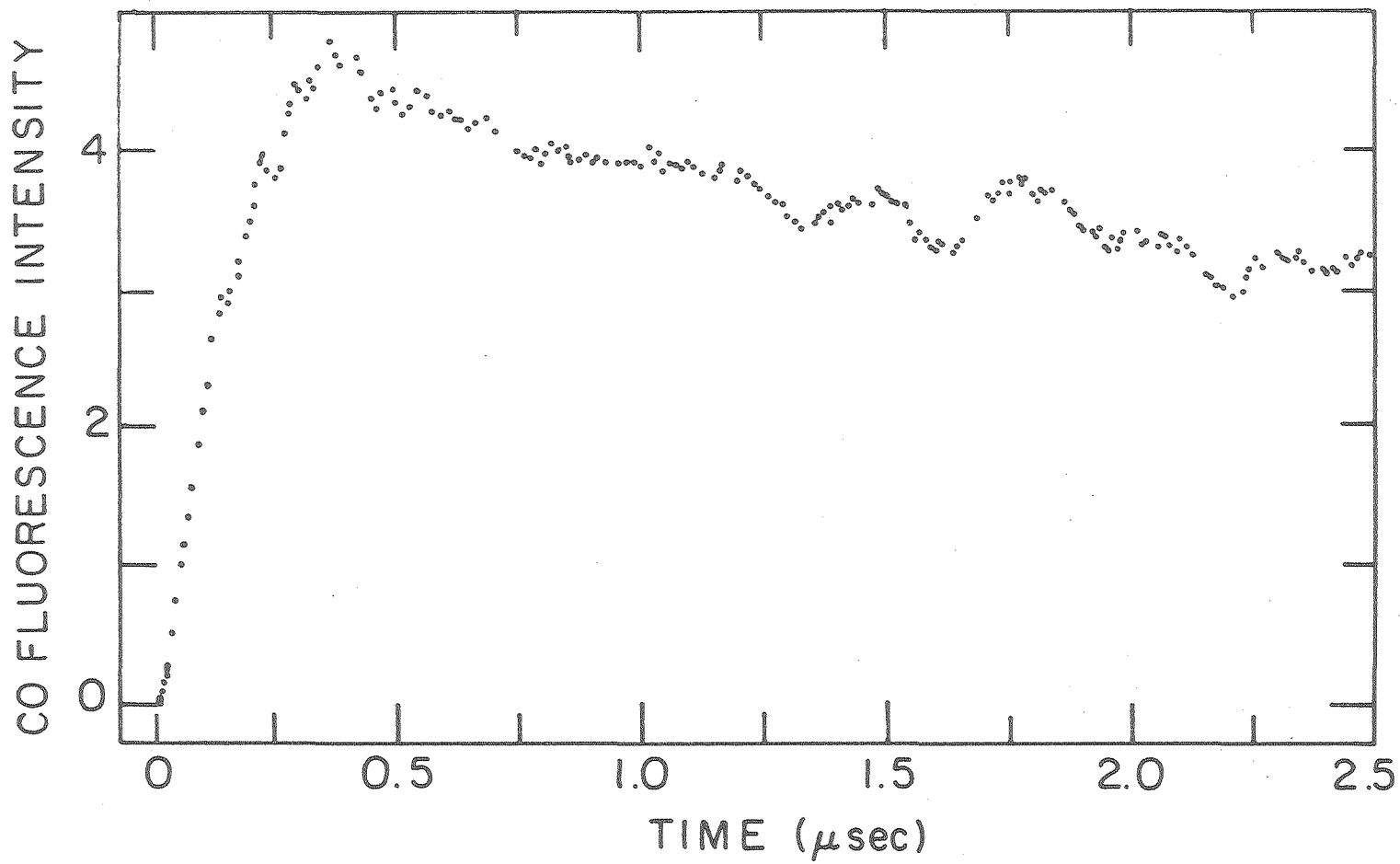
D. KETENE ($\text{CH}_2 = \text{C} = \text{O}$)

The rise time of the CO fluorescence signal following photolysis of ketene at 354.7 nm appears quite fast and is detector limited at the lowest pressure of 0.12 torr. A lower limit for the primary photodissociation rate into CO and CH_2 : would therefore be set as $80 \mu\text{sec}^{-1} \text{ torr}^{-1}$. Figure 34 shows a CO fluorescence trace depicting the rise of the fluorescence signal obtained for 0.12 torr ketene.

At pressures higher than 0.12 torr, the fluorescence signal exhibits some complicated structure, possibly due to secondary reactions that produce vibrationally hot carbon monoxide. This is clearly shown in figure 35 which is a typical trace obtained for 1.00 torr ketene.

Secondary reactions between singlet or triplet methylene produced in the primary process and ground state ketene are known to produce more carbon monoxide.⁹⁷⁻¹⁰⁰ Therefore in an attempt to check whether the complex structure is primarily due to CO fluorescence, cis-2-butene was added to ketene as a possible quenching agent for methylene radicals. Typical results are shown in figure 36 which is a CO fluorescence trace obtained for a mixture of 1.00 torr ketene + 1.81 torr cis-2-butene. It is apparent that cis-2-butene does remove part of the

Figure 31. CO fluorescence trace showing the rise of fluorescence signal following photolysis of 0.089 torr acrolein at 354.7 nm. The trace is an average of 1024 laser shots.



-142-

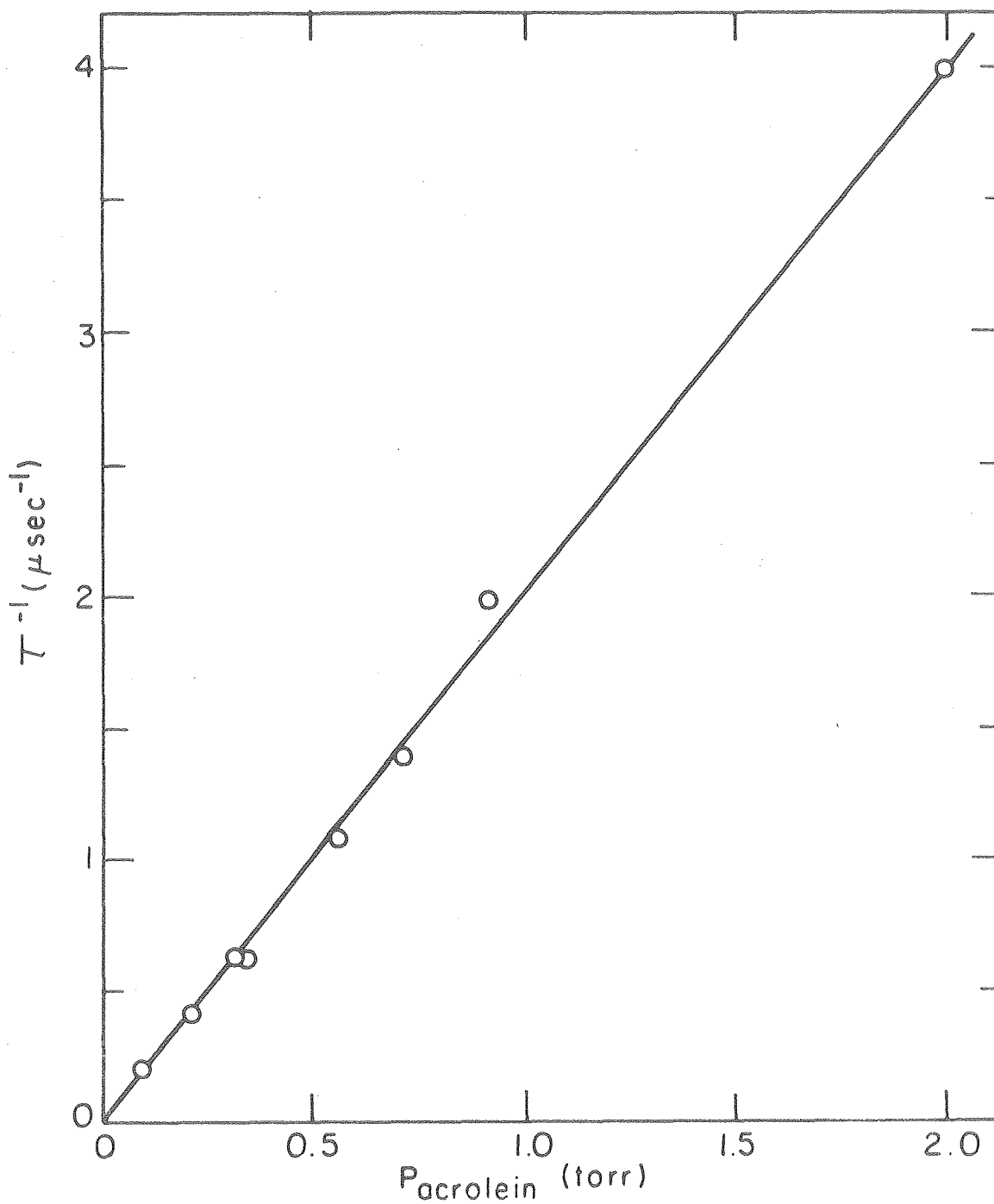
XBL 788-5637

Fig. 31.

Table XI. CO ($v = 1$) decay rates in acrolein following photolysis at 354.7 nm.

Acrolein (torr)	τ^{-1} (μsec^{-1})	$(p\tau)^{-1}$ ($\mu\text{sec}^{-1} \text{ torr}^{-1}$)
0.089	0.20	2.20
0.217	0.40	1.86
0.325	0.61	1.87
0.335	0.62	1.87
0.55	1.07	1.95
0.72	1.38	1.93
0.94	1.98	2.11
1.99	3.97	2.00

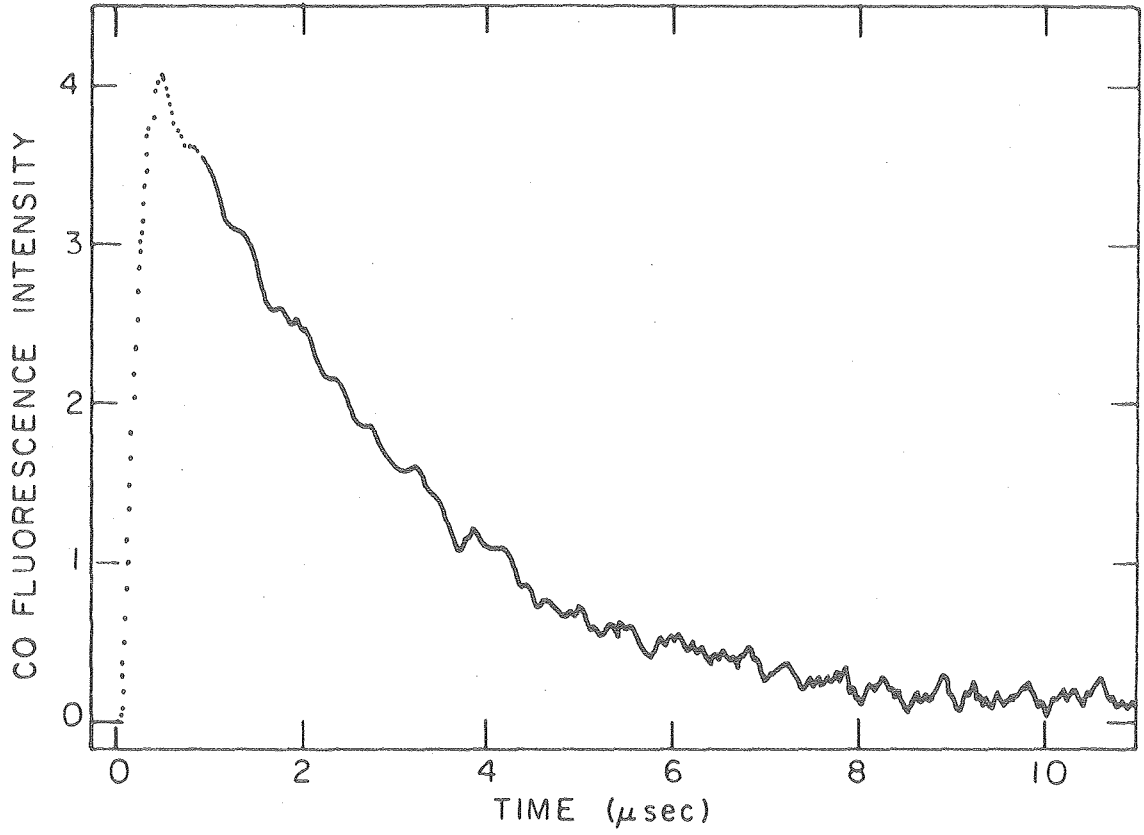
Figure 32. CO ($v = 1$) decay rates against acrolein gas pressure following photolysis at 354.7 nm. The rate constant obtained from a least-squares fit of data is $2.02 \pm 0.22 \mu\text{sec}^{-1} \text{ torr}^{-1}$.



XBL788-5638

Fig. 32.

Figure 33. CO ($v = 1$) fluorescence decay trace following photolysis of 0.217 torr acrolein at 354.7 nm. The trace is an average of 1024 laser shots.



XBL 788-5639

Fig. 33.

Figure 34. CO fluorescence trace showing the rise of fluorescence signal following photolysis of 0.12 torr ketene at 354.7 nm. The trace is an average of 1024 laser shots.

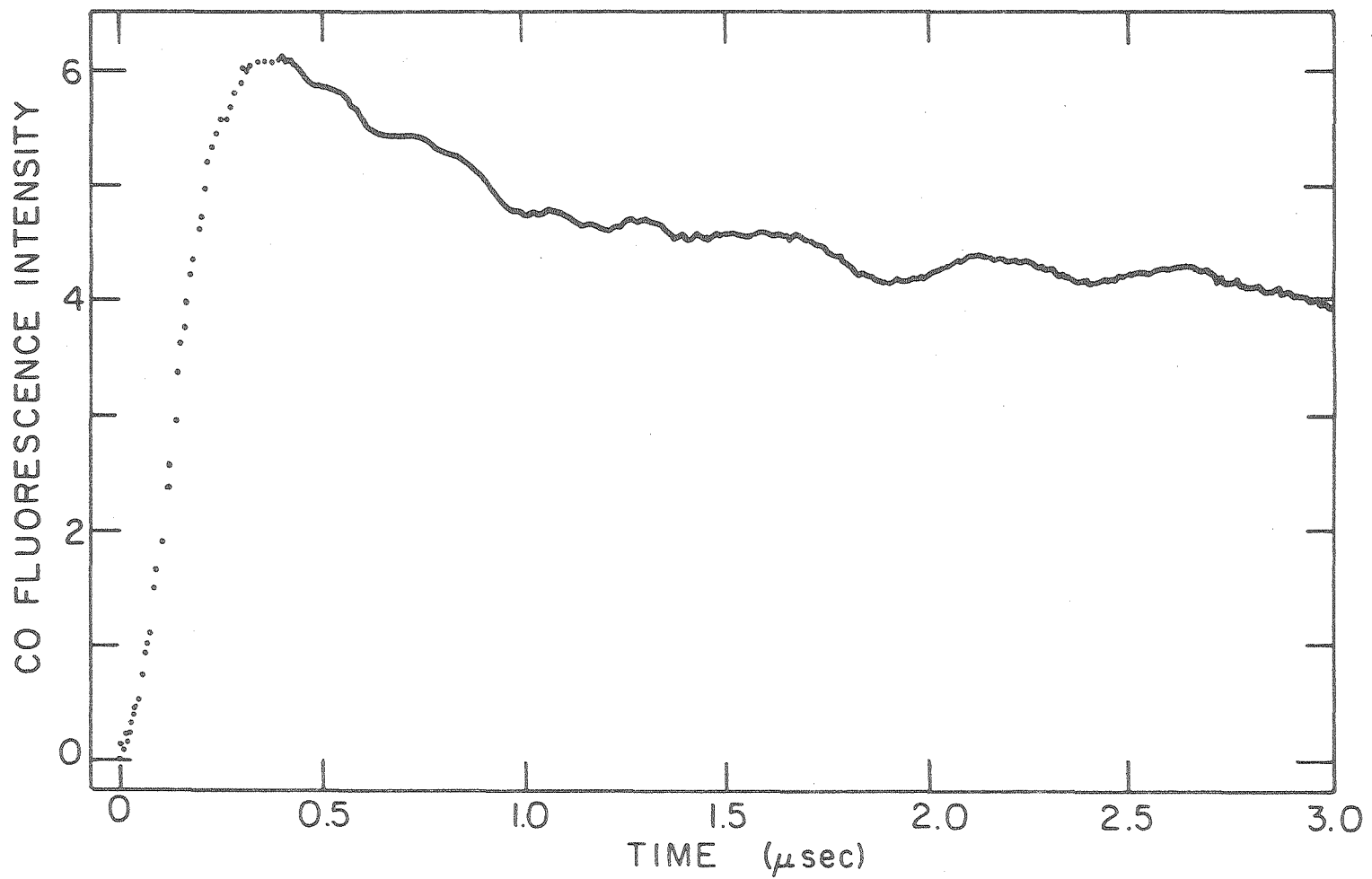
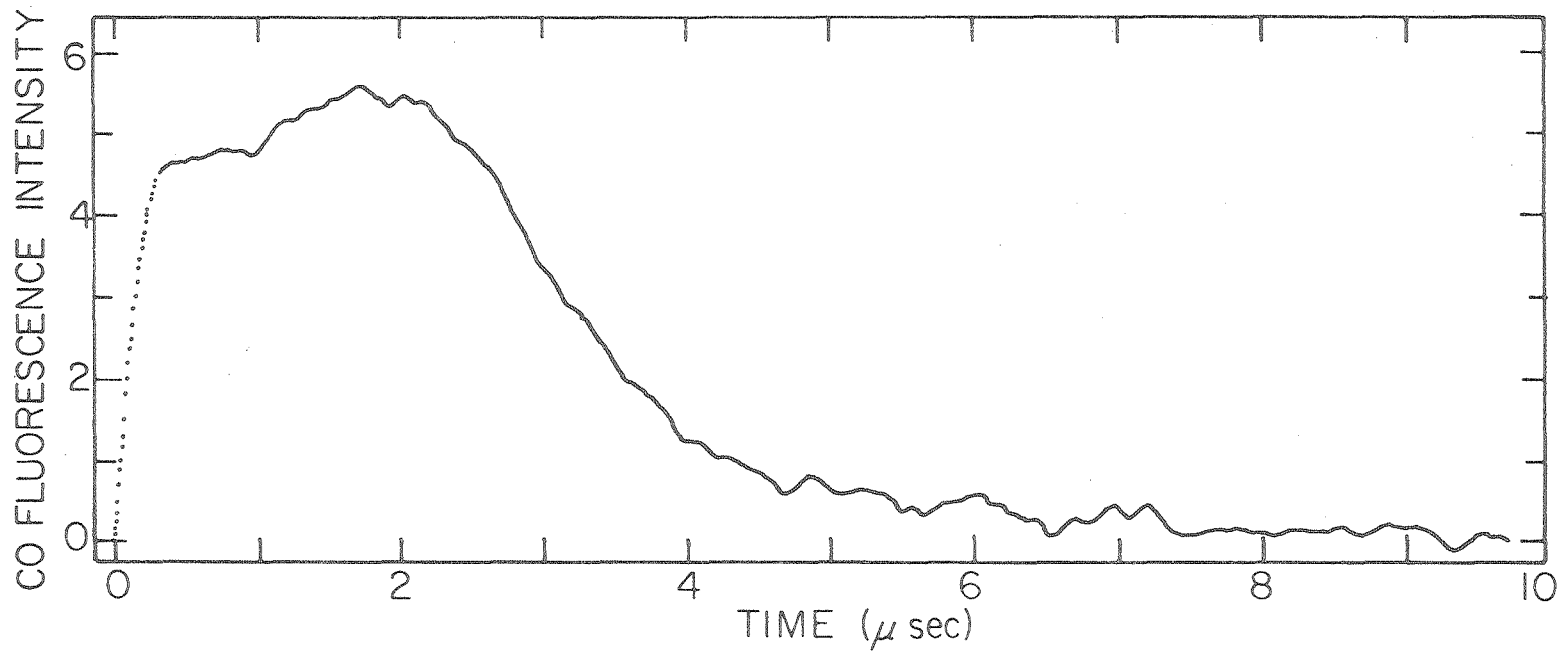


Fig. 34.

XBL 788-5640

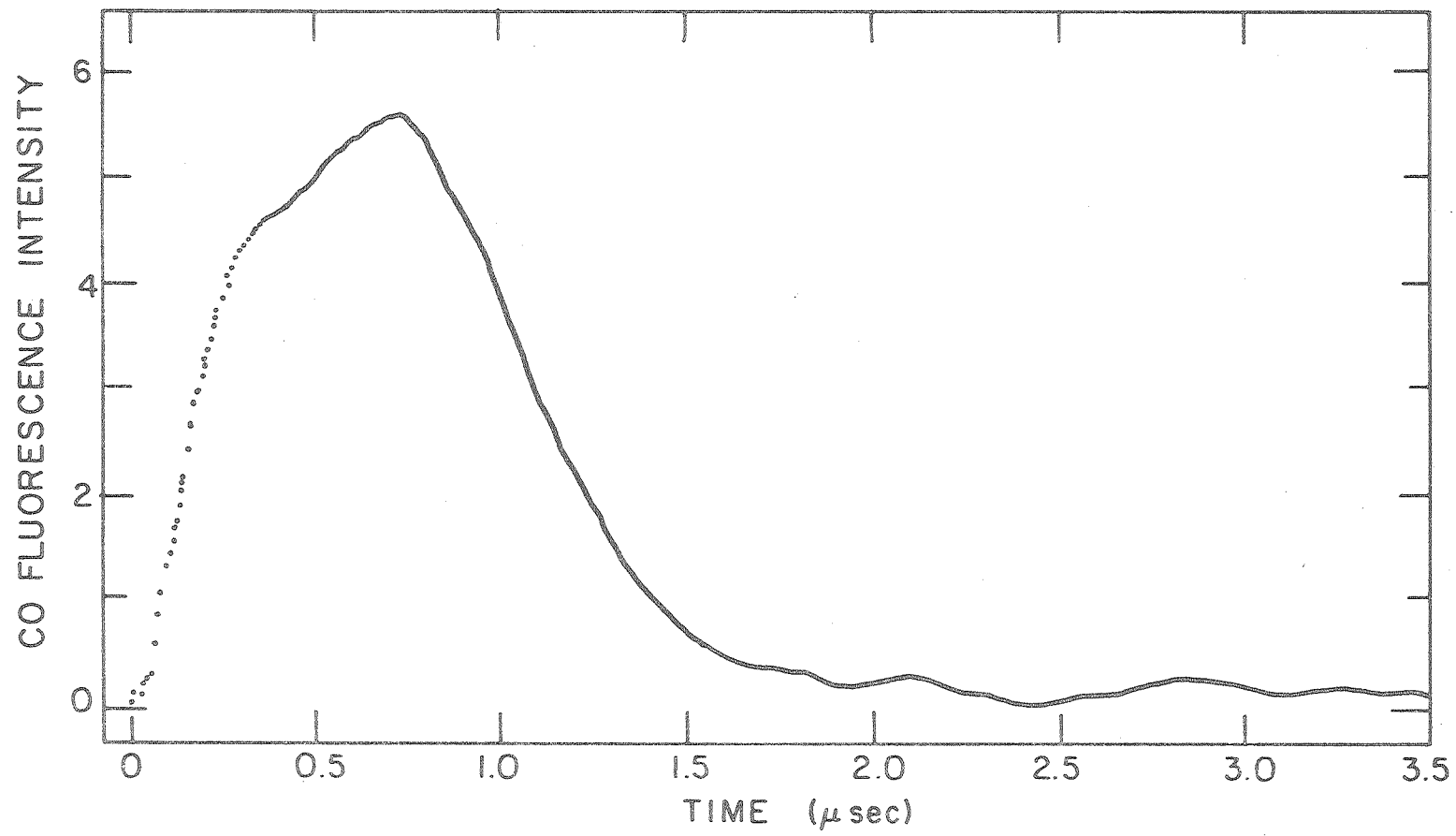
Figure 35. CO fluorescence trace obtained following photolysis of 1.00 torr ketene at 354.7 nm. The trace is an average of 1024 laser shots.



XBL 788-564I

Fig. 35.

Figure 36. CO fluorescence trace obtained for 1.00 torr ketene + 1.81 torr cis-2-butene gas mixture following photolysis at 354.7 nm. The trace is an average of 1024 laser shots.



XBL788-5642

Fig. 36.

complex structure seen in pure ketene. Further study of the pressure dependence of the rise portion of the signal on cis-2-butene proved difficult for it was necessary to use very low ketene pressure to attain reasonable time resolution. This was impractical however due to the lower signal-to-noise ratio obtained thus making the analysis inadequate.

The pressure dependence of CO ($v = 1$) decay rates in ketene is shown in Table XII. Figure 37 is a plot of those rates against ketene gas pressure yielding a rate constant of $1.14 \pm 0.20 \mu\text{sec}^{-1} \text{ torr}^{-1}$.

Table XIII lists the decay rates in ketene + cis-2-butene mixtures and the rates plotted against cis-2-butene gas pressure are shown in figure 38. The rate constant thus obtained is $1.35 \pm 0.26 \mu\text{sec}^{-1} \text{ torr}^{-1}$.

E. CYCLOBUTANONE

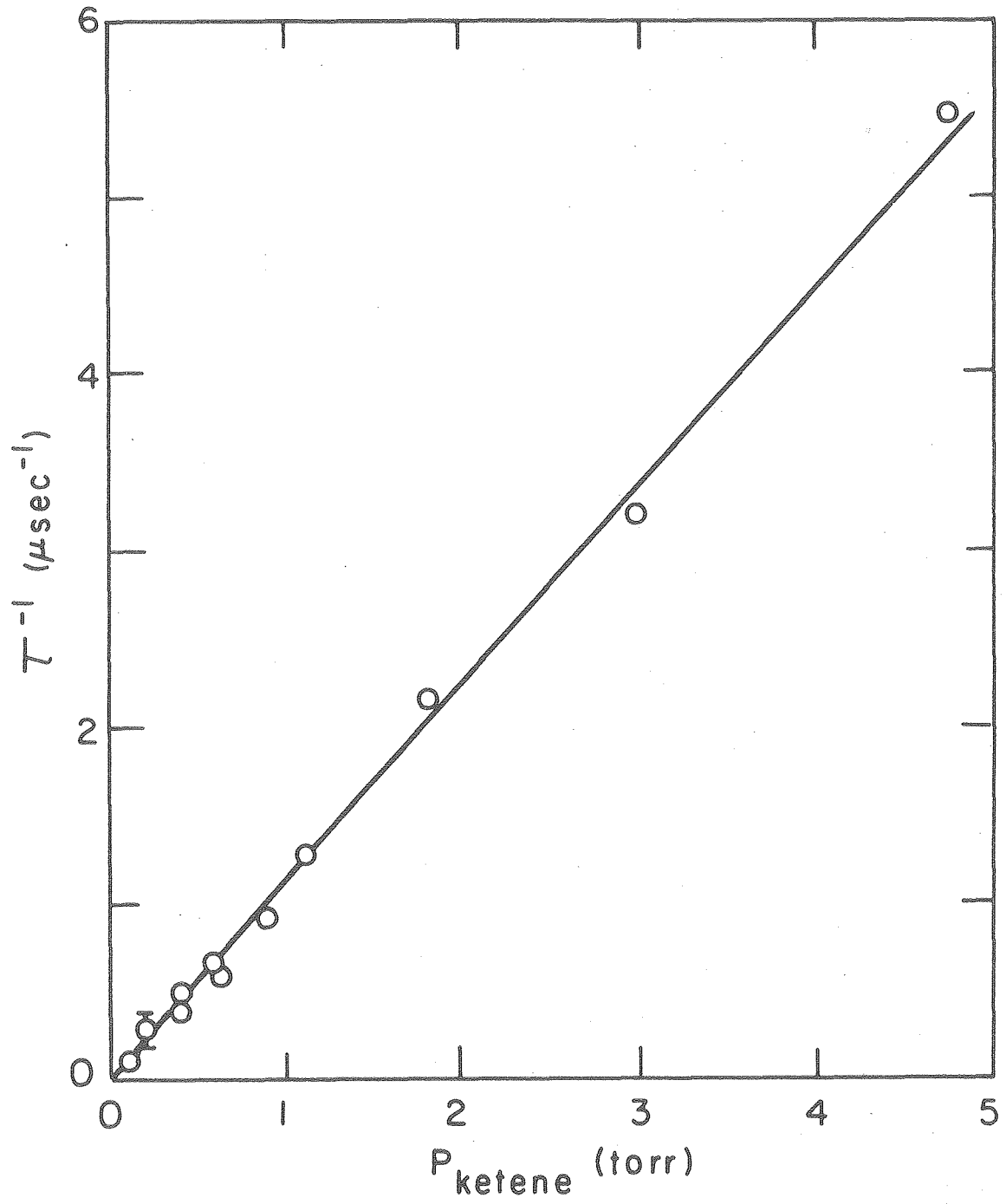
The CO appearance rates were also studied in photolysis of cyclobutanone at 299.1 nm. The measured rates were also fast and at the lowest gas pressure (0.26 torr) appeared to be detector limited. A lower limit for the rate of appearance of CO is therefore set at $38 \mu\text{sec}^{-1} \text{ torr}^{-1}$. Figure 39 shows a CO fluorescence trace obtained following photolysis of 0.40 torr cyclobutanone at 299.1 nm.

The CO ($v = 1$) decay rates are listed in Table XIV and figure 40 show a plot of those rates against gas pressure. The CO decay rate constant in cyclobutanone is therefore calculated as $1.38 \pm 0.24 \mu\text{sec}^{-1} \text{ torr}^{-1}$.

Table XII. CO ($v = 1$) decay rates in ketene following photolysis at 354.7 nm.

P_{ketene} (torr)	τ^{-1} (μsec^{-1})	$(p\tau)^{-1}$ ($\mu\text{sec}^{-1} \text{ torr}^{-1}$)
0.12	0.11	0.92
0.21	0.29	1.41
0.38	0.38	1.00
0.40	0.53	1.32
0.59	0.67	1.15
0.64	0.58	0.91
1.00	1.10	1.10
0.88	0.89	1.01
1.12	1.32	1.18
1.78	2.16	1.22
2.99	3.2	1.07
4.75	5.47	1.15

Figure 37. CO ($v = 1$) decay rates against ketene gas pressure following photolysis at 354.7 nm. The straight line which is a least-squares fit for data yields at a rate constant of $1.14 \pm 0.20 \mu\text{sec}^{-1} \text{ torr}^{-1}$.



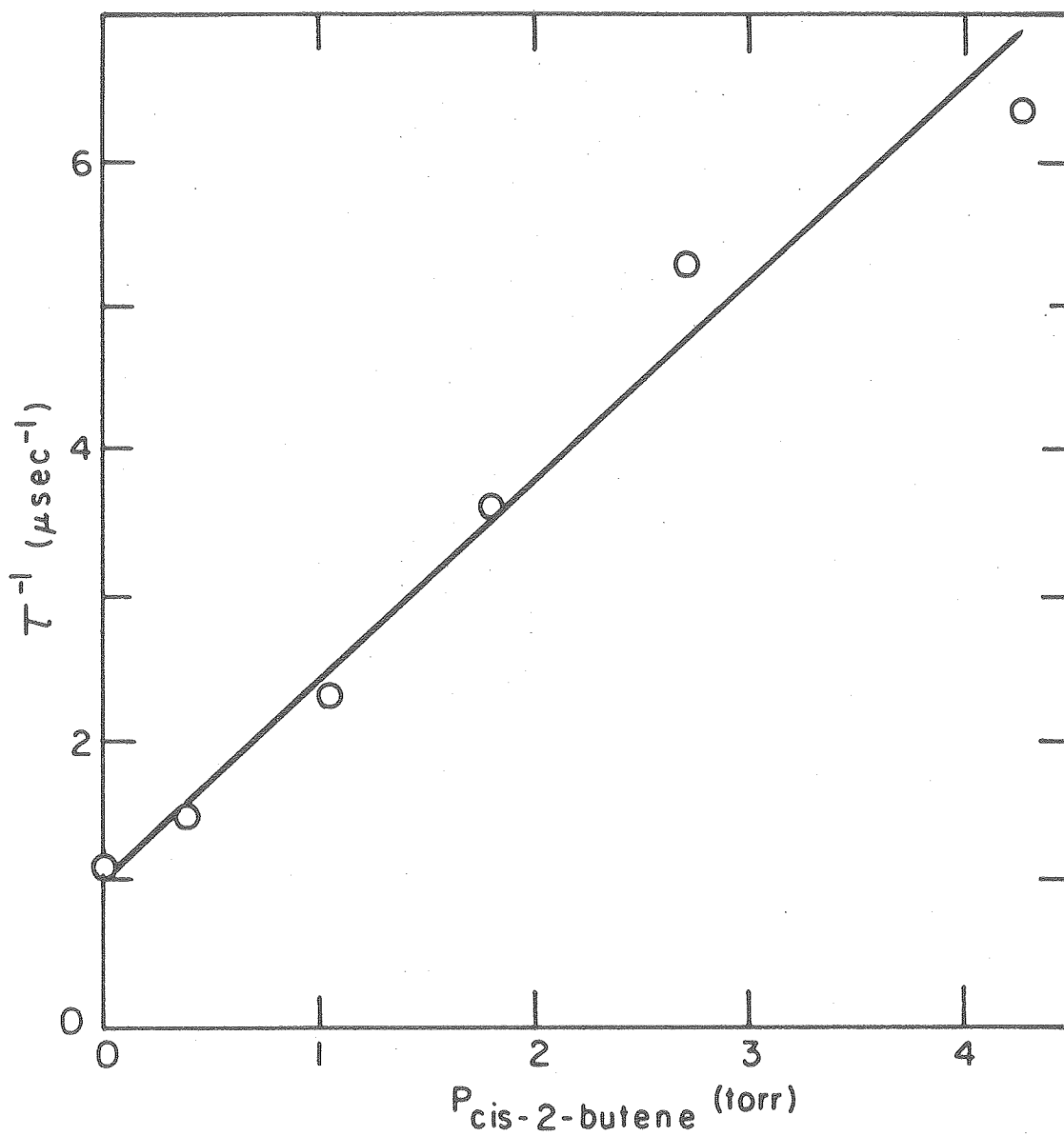
XBL 788-5643

Fig. 37.

Table XIII. CO ($v = 1$) decay rates following photolysis of ketene + cis-2-butene gas mixtures at 354.7 nm.

P_{ketene} (torr)	$P_{\text{cis-2-butene}}$ (torr)	τ^{-1} (μsec^{-1})
1.00	0	1.10
1.00	0.40	1.44
1.01	1.12	2.30
1.00	1.81	3.61
1.00	2.71	5.29
1.01	4.19	6.34

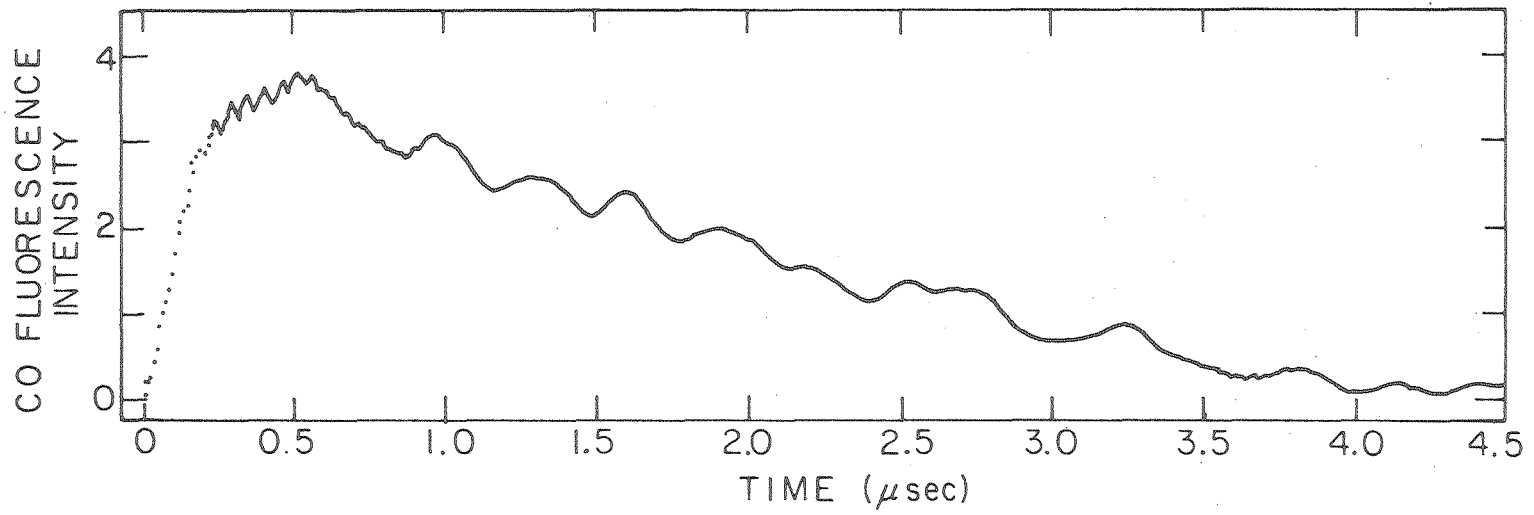
Figure 38. CO ($v = 1$) decay rates against cis-2-butene gas pressure following photolysis of ketene + cis-2-butene gas mixtures at 354.7 nm. the rate constant obtained from the least-squares fit of data is $1.35 \pm 0.26 \mu\text{sec}^{-1} \text{ torr}^{-1}$.



XBL 788-5644

Fig. 38.

Figure 39. CO fluorescence trace obtained following photolysis of 0.40 torr cyclobutanone at 299.1 nm. The trace is an average of 1024 laser shots.



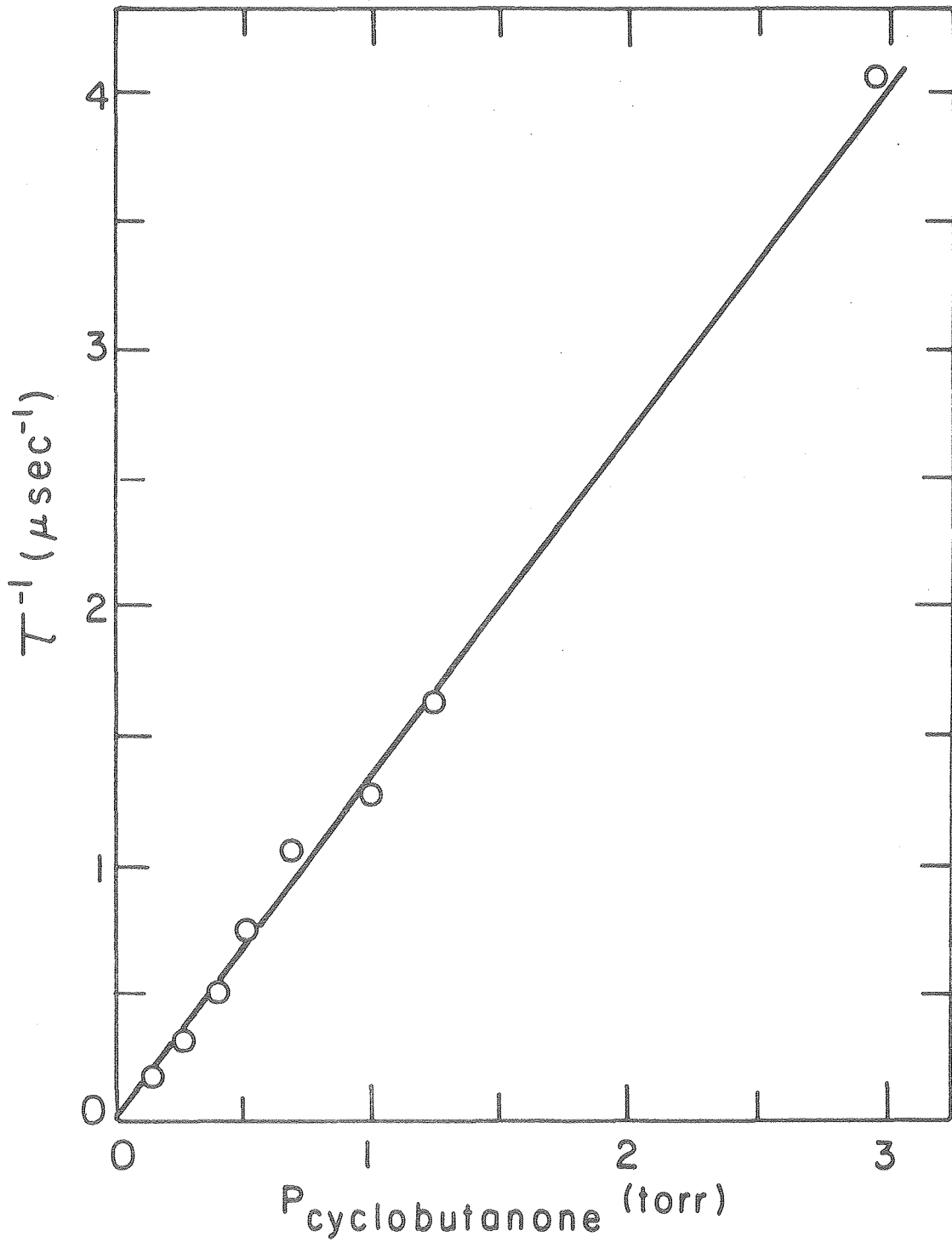
XBL788-5645

Fig. 39.

Table XIV. CO ($\nu = 1$) decay rates in cyclobutanone following photolysis at 299.1 nm.

$P_{\text{cyclobutanone}}$ (torr)	τ^{-1} (μsec^{-1})	$(p\tau)^{-1}$ ($\mu\text{sec}^{-1} \text{ torr}^{-1}$)
0.14	0.16	1.18
0.27	0.31	1.16
0.40	0.49	1.22
0.51	0.75	1.48
0.68	1.06	1.57
1.00	1.26	1.26
1.24	1.63	1.32
2.95	4.07	1.38

Figure 40. CO ($v = 1$) decay rates in cyclobutanone following photolysis at 299.1 nm. The rate constant obtained is $1.38 \pm 0.24 \mu\text{sec}^{-1} \text{ torr}^{-1}$.



XBL 788-5646

Fig. 40.

F. SUMMARY OF RESULTS

The results obtained on the CO appearance rates for the carbonyl compounds studied in this work are listed in Table XV. The effect of foreign gases on those rates are also included. Table XVI lists the results obtained on the decay rates of CO ($v = 1$) for the various collision partners studied.

Table XV. Summary of results on CO appearance rates.

Molecule Excited	λ (nm)	Collision Partner	$(p\tau)^{-1}$ ($\mu \text{ sec}^{-1} \text{ torr}^{-1}$)
H ₂ CO	354.7	H ₂ CO	1.72 ± 0.22
H ₂ CO	337.1	H ₂ CO	1.65 ± 0.12*
H ₂ CO	299.1	H ₂ CO	16 ± 7
H ₂ CO	354.7	He	1.04 ± 0.26
H ₂ CO	354.7	Ar	1.28 ± 0.20
H ₂ CO	354.7	Xe	1.45 ± 0.24
H ₂ CO	354.7	NO	1.40 ± 0.48
H ₂ CO	337.1	NO	1.9 ± 0.5*
HDCO	354.7	HDCO	1.4 ± 0.4
D ₂ CO	354.7	D ₂ CO	0.7 ± 0.2
D ₂ CO	337.1	D ₂ CO	0.96 ± 0.07*
D ₂ CO	337.1	Ar	0.10 ± 0.01*
CH CCHO	354.7	CH CCHO	20
CH ₂ = CHCHO	354.7	CH ₂ = CHCHO	75
CH ₂ = C = O	354.7	CH ₂ = C = O	80
Cyclobutanone	299.1	Cyclobutanone	38

*Reference 25.

Table XVI. Summary of results on CO ($v = 1$) decay rates.

Molecule Excited	Excitation Wavelength (nm)	Collision Partner	$(p\tau)^{-1}$ ($\mu \text{ sec}^{-1} \text{ torr}^{-1}$)
H ₂ CO	354.7	H ₂ CO	$(1.75 \pm 0.32) \times 10^3$
H ₂ CO	337.1	H ₂ CO	$(1.31 \pm 0.11) \times 10^{3*}$
HDCO	354.7	HDCO	$(7.8 \pm 0.3) \times 10^4$
HDCO	337.1	HDCO	$(6.5 \pm 0.7) \times 10^{4*}$
D ₂ CO	337.1	D ₂ CO	$(1.15 \pm 0.18) \times 10^{5*}$
CH ₂ = CHCHO	354.7	CH ₂ = CHCHO	$(2.02 \pm 0.22) \times 10^6$
CH ₂ = C = O	354.7	CH ₂ = C = O	$(1.14 \pm 0.20) \times 10^6$
CH ₂ = C = O	354.7	cis-2-butene	$(1.35 \pm 0.26) \times 10^6$
Cyclobutanone	299.1	Cyclobutanone	$(1.38 \pm 0.24) \times 10^6$

*Reference 25.

V. HYDROGEN ATOM DETECTION

A. GENERAL DESCRIPTION

Three different methods were tried in order to measure the rates of appearance of H-atoms following laser photolysis of formaldehyde in the ultraviolet. The first two utilized the resonance fluorescence and resonance absorption of Hydrogen Lyman- α (H_{α}) radiation at 1215.7Å using a resonance lamp as an excitation source. This corresponds to the dipole allowed single photon 1S-2P transition. The third method used was based on the resonantly enhanced Doppler-free two-photon excitation of the 1S-2S transition followed by detection of the collision-induced fluorescence emission of H_{α} photons from the 2P state.

Before discussing the experimental procedures used, a brief theoretical background will be given below on resonance trapping and collisional quenching effects on detection of H_{α} radiation, and also on calculation of the transition rates for two-photon absorption and three-photon ionization in H-atoms.

B. RESONANCE TRAPPING OF H_{α} FLUORESCENCE

The repeated absorption of emitted resonance radiation may present a serious limitation on the accuracy of measured excited state lifetimes. This phenomenon, known as resonance trapping or imprisonment, normally manifests itself in longer measured lifetimes of excited atoms due to repeated absorption and emission of resonance fluorescence prior to escape from the fluorescence cell. In cases where collisional quenching of fluorescence becomes significant, longer lifetimes lead to attenuation of the overall emission thus adding a further limitation on detection, especially when the fluorescence signal is critically

low to begin with. In absorption spectroscopy, resonance trapping always causes broadening of the spectrally resolved absorption lines coupled with a reversal of the line center.

A rigorous treatment of resonance trapping is rather complicated and would have to consider several parameters such as the state of polarization of the exciting radiation, the detection cell geometry as well as the emitting layer geometry. For polarization effects and detection geometry, reference is made here to articles by Deech and Baylis,¹⁰¹ D'yakonov and Perel,¹⁰² and also Barrat.¹⁰³⁻¹⁰⁵ The two classical articles by Holstein^{106,107} treat in detail the emitting layer geometry effects and will be used as a basis for the following analysis.

The decay of trapped resonance fluorescence in atoms whose excited state has a natural lifetime $\tau = 1/\gamma$ generally assumes the exponential form $e^{-\gamma t}$ where g is the escape factor; g is normally considered as the reciprocal of number of times resonant photons are reabsorbed and emitted prior to escape from the fluorescence cell. For Doppler-broadened absorption lines of atoms in a cylindrical enclosure of radius R , the g factor is given by

$$g = 1.60/K_0 R (\pi \log K_0 R)^{1/2} \quad (72)$$

where K_0 is the absorption coefficient at the center of the absorption line which is given by the formula¹⁰⁸

$$K_0 = \frac{\lambda_0^3}{8\pi} \frac{N}{g_1} \frac{g_2}{\pi^{1/2}} \frac{1}{v_0 \tau} \quad (73)$$

where λ_0 is the wavelength at the center of absorption line, N is the number of atoms per unit volume, g_2/g_1 is the ratio of excited to ground state statistical weights which is equal to 3 for H_α transition, and v_0 is the most probable atomic velocity given by

$$v_0 = \left(\frac{2RT}{M} \right)^{1/2}$$

where R is the gas constant, T is the absolute temperature and M is the gram-atomic weight.

At 1 torr pressure of H-atoms, for example, the absorption coefficient is calculated as $K_0 = 1.10 \times 10^4 \text{ cm}^{-1}$. If the H-atoms are enclosed in a cylindrical geometry with radius of 0.05 cm, the g factor is estimated as $g = 10^{-3}$, the reciprocal of which is thus 10^3 and the effective lifetime of H_α photons would be increased from that of the 2P state ($\tau = 1.6 \text{ nsec}$)¹⁰⁹ to 1.6 μsec , which is quite appreciable. It should be noted however that, under normal experimental conditions, the H-atom pressure within the enclosure mentioned above may not exceed 10^{-2} torr thus increasing the effective lifetime to only 10 nsec. This was the case for the two-photon excited H_α fluorescence experiment to be discussed later.

In experiments carried out to detect H-atoms through resonance fluorescence using an H_α lamp as the excitation source, a rectangular geometry was used for which the g factor assumes the following form:¹⁰⁷

$$g = 1.875/K_0 L (\pi \log 1/2 K_0 L)^{1/2} \quad (74)$$

where L is the depth of H-atom enclosure subtended by the detector and was equal to 0.9 cm. In such arrangement the H-atom pressure within the enclosure corresponded to 10^{-3} torr at most and the effective H-Ly- α fluorescence lifetime is increased to 16 nsec. This small increase in the effective lifetime may not be of importance in so far as time resolution is concerned, nevertheless, it will prove to be detrimental for detection when collisional quenching becomes significant as will be demonstrated in the following section.

C. COLLISIONAL DEACTIVATION OF H₂(²S, ²P) STATES

Since collisional quenching cross sections of the H(2S) or (2P) states by formaldehyde have not been measured, an estimate could perhaps be obtained through a comparison with some closely related molecules. McCusker and co-workers¹¹⁰ have recently measured quenching cross sections for the H(2S) state by various gases using the beam-attenuation method in conjunction with a time-of-flight technique. The results indicate a relatively high cross sections for polar molecules such as 1964 Å² for CH₃OH, 2500 Å² for NH₃, and 5003 Å² for acetone - where these values are normalized to thermal velocities at room temperature. The corresponding cross sections for quenching by the rare gases and non polar molecules were almost an order of magnitude lower, namely; He:141 Å², Ne:118 Å², Ar:163 Å², Kr:251 Å², Xe:422 Å², H₂:149 Å², and N₂:320 Å².¹¹⁰

Although the method used above does not indicate the mode of decay of the 2S state, the authors assume that it proceeds almost exclusively via fluorescence emission of H α radiation from the 2P

state populated through collisionally-induced 2S-2P transition. The assumption here was based on theoretical arguments presented earlier by Slocumb, Miller, and Schaefer¹¹¹ in which they predict very low quenching cross sections for the 2P states ($\sim 1 \text{ \AA}^2$); the reason is again based on the absence of resonant energy transfer processes with the quenching molecules, and also, the relatively short lifetime of the 2P state (1.6 nsec) compared with the typical duration between collisions (≥ 100 nsec).

There are several experimental studies, however, which show that collisional quenching of the radiative 2P state is almost as efficient as that of the metastable 2S state. Comes and Wenning^{112,113} measured quenching cross sections for the 2S state in H_2 which result in H_α emission of 60 \AA^2 , and 48 \AA^2 for the nonradiative process. Mentall and Gentieu¹¹⁴ measured the ratio of radiative to non radiative quenching cross sections to be ~ 2.0 at room temperature, with the ratio slightly increasing with temperature. Young, et al.^{115,116} measured cross sections for quenching of the 2P state in H_2 and D_2 in the range $84\text{-}91 \text{ \AA}^2$. So it is apparent that collisional quenching of the metastable 2S state does not necessarily lead exclusively to H_α fluorescence emission. Furthermore, collisional quenching of the 2P state is efficient even in the absence of resonant energy transfer processes. For example, in the case of H_2 , where no electronic energy transfer process is obvious since electronic absorption occurs at (1050 \AA), an energy higher than that of H_α photons, and photoionization is still much higher (850 \AA),¹¹⁷ collisional quenching appears to be efficient.

Thus it seems reasonable to assume that polar molecules will quench the 2P state even more efficiently.

Since the measured 2S collision quenching cross sections by polar molecules are high, namely; 1000-1810 Å² for H₂O,^{118,119} 1000 Å² for CH₃I,¹²⁰ 1964 Å² for CH₃OH, 2500 Å² for NH₃, and 5003 Å² for acetone, the corresponding value for H₂CO would probably be in the range 1000-3000 Å². If quenching of the ²P state is as high, then this will cause a drastic attenuation of H_α fluorescence in a dilute mixture of H in H₂CO.

To illustrate this, let us assume that the quenching cross section for the 2P state is 1000 Å² or 10⁻¹³ cm². Then for H-atoms with a relative thermal velocity $v = 2.56 \times 10^5$ cm/sec in 1 torr of H₂CO ($N = 3.24 \times 10^{16}$ molecules/cm³), the overall transmission of H_α photons would be given by

$$I/I_0 = (1 + \sigma v N \tau_{\text{eff}})^{-1}$$

where τ_{eff} is the effective lifetime of fluorescence emission calculated according to section B above. So for $\tau_{\text{eff}} = 16$ nsec, only ~7% of fluorescence emission will be transmitted.

D. DOPPLER-FREE TWO-PHOTON 1S-2S EXCITATION

The two photon excitation of the 1S-2S transition and the subsequent spectroscopic detection of H_α fluorescence has been successfully demonstrated by Hansch and co-workers.^{121,122} In this case, the relatively low transition probability is greatly enhanced through cancellation of Doppler broadening by reflecting the excitation beam onto itself,

thus making a standing wave field in which all atoms absorb regardless of their thermal velocities.¹²³

The output of a N₂ laser-pumped dye laser at 4862.8 was frequency doubled and pressure tuned to coincide with half the 1S-2S transition frequency, and the excited atoms were then detected through collision-induced H_α fluorescence from the 2P state.¹²¹⁻¹²³

1. 1S-2S Transition Rate

The theory of two-photon absorption has been treated by Goppert-Mayer¹²⁴ and recently applied to 1S-2S transitions by several other workers.^{123,125-127} The transition probability is derived using second order time-dependent perturbation theory with the transition rate for the H(1S-2S) transition given by^{128,129}

$$R_{12} = \frac{\tau}{\hbar^2} \left| \sum_K \frac{\langle 1S | H_1 | K \rangle \langle K | H_2 | 2S \rangle + \text{c.c.}}{\hbar \Delta \omega_K} \right|^2 \quad (76)$$

where K runs over all intermediate states connected to 1S and 2S states through electric-dipole allowed transitions. In the equation above, H₁ and H₂ stand for the interaction Hamiltonian between the two photons of frequencies ω₁ and ω₂ with the atomic states, τ is the photon pulse duration, Δω_K is the frequency mismatch between the photon and the intermediate state, and c.c. is the complex conjugate.

The interaction Hamiltonian between the radiation field and the atomic states is given by

$$H_i = -(e/mc) \vec{A} \cdot \vec{p} + \left(\frac{e^2}{2mc^2} \right) \vec{A} \cdot \vec{A} \quad (77)$$

where \vec{A} is the vector potential and \vec{p} is the momentum, e is the electron charge, m its mass and c is the speed of light. In the long wavelength (dipole) approximation where the vector potential is given as

$$\vec{A} = \left(\frac{2\pi\hbar n}{\omega V} \right)^{1/2} \cdot \hat{\epsilon} \quad (78)$$

the second term in the interaction Hamiltonian containing the product $\vec{A} \cdot \vec{A}$ does not change the state of the atom and equation (77) assumes the form

$$H_i = -e/m \left(\frac{2\pi\hbar n}{\omega V} \right)^{1/2} \hat{\epsilon} \cdot \vec{p} \quad (79)$$

Here, n indicates the photon occupation number, V the volume, and $\hat{\epsilon}$ the polarization vector of the photons. Substituting for H_1 and H_2 into equation (76) we obtain

$$R_{12} = \frac{4\tau}{\hbar^2} \frac{e^4}{m^4} \left(\frac{2\pi\hbar n_1}{\omega_1 V} \right) \left(\frac{2\pi\hbar n_2}{\omega_2 V} \right) \times \left| \sum_K \frac{\langle 1S | \hat{\epsilon} \cdot \vec{p} | K \rangle \langle K | \hat{\epsilon} \cdot \vec{p} | 2S \rangle}{\hbar \Delta\omega_K} \right|^2$$

If the laser bandwidth ($\Delta\omega$) is near Fourier-transfer limited, then τ is replaced by $\Delta\omega^{-1}$, and substituting for the laser intensity

$$I = \frac{n\hbar\omega c}{\omega V}$$

the transition rate becomes

$$R_{12} = 16\pi^2 \frac{e^4}{\hbar^2 c^2} (m\omega)^{-4} \frac{I_1 I_2}{\Delta\omega} \left| \sum \frac{\langle 1S | \hat{\epsilon} \cdot p | K \rangle \langle K | \hat{\epsilon} \cdot p | 2S \rangle}{\hbar \Delta\omega K} \right|^2 \quad (79)$$

The matrix elements on the right side of eq. (79) were evaluated by Gontier and Trahin¹³⁰ as 0.276 at. units, where an atomic unit corresponds to p^2/E , $p = me^2/\hbar = 1.99 \times 10^{-19}$ g cm·sec⁻¹ and $E = e^2/a = 4.36 \times 10^{-11}$ erg. In Gaussian (cgs) units, the matrix element would therefore be equal to $0.276 \times 9.08 \times 10^{-28}$ gm or 2.51×10^{-28} gm. Substituting for all known constants in cgs units the transition rate would therefore be

$$R_{12} = 21.2 (I_1 I_2 / \Delta\omega) \quad (80)$$

where I_1 and I_2 are given in watt/cm² and $\Delta\omega$ in sec⁻¹.

2. Photoionization of the 2S State

The photoionization cross section from the 2S state by photons of frequency ν has been derived by Stobbe¹³¹ and also Bethe and Salpeter¹³² and is given by

$$\sigma_{2S} = \frac{2\pi e^2}{3mc} \frac{\nu_2^3}{\nu^4} \left(1 + 3 \frac{\nu_2}{\nu} \right) \frac{e^{-4n \arccot n/2}}{1 - e^{-2\pi n}} \quad (81)$$

where e and m are the electron charge and mass in esu units, respectively, and $\hbar\nu_2$ is the ionization energy from the 2S state which is equal to $1/4$ in terms of the ionization potential from the ground state of the H-atom. The value of n is given in terms of ν and ν_2 according to the

expression¹³² $n = \sqrt{2} \nu_2 / (\nu - \nu_2)$. For photons at 2431.4 Å, the energy given in terms of a unit ionization potential would be $h\nu = 3/8$ and n is therefore equal to $\sqrt{8}$. Substituting for

$$\nu_2/\nu = \frac{n^2}{n^2 + 4}$$

into equation (81), the photoionization cross section would be given as

$$\sigma_{2S} = \frac{213\pi e^2}{3mc} \frac{n^6(1 + n^2)}{(n^2 + 4)^4} \frac{e^{-4n \arccot n/2}}{1 - e^{-2\pi n}}$$

or $\sigma_{2S} = 1.23 \times 10^{-17} \text{ cm}^2$.

If the photon flux at frequency ν equals N photons per cm^2 per sec, then the transition rate becomes

$$\Gamma = N\sigma_{2S} \text{ sec}^{-1}$$

Since the laser power used in this work was $2 \times 10^5 \text{ W/cm}^2$, $N = 4.8 \times 10^{23} \text{ photons/cm}^2/\text{sec}$. The two beams at 2431.4 Å will yield a photoionization rate $\Gamma = 1.2 \times 10^7 \text{ sec}^{-1}$. For a 5 nsec pulse, the number of photoionized atoms will therefore be ~6% of those atoms in the 2S state.

3. Two-Photon Laser Excitation Source

A N_2 laser-pumped dye laser system modeled after that of Hansch^{133,134} was used to pump the 1S-2S transition in H-atoms. The dye laser consisted of an oscillator and two amplifier stages pumped with the output of a N_2 laser delivering 10 mJ pulses of 10 nsec duration (Molelectron, UV-1000). Frequency selection of the oscillator was

obtained through a 1200 ℓ/mm grating blazed at 1.4μ and housed together with an internal etalon in a stainless steel chamber. Pressure tuning of the dye laser output was obtained through N_2 gas over 2\AA . For more details on the dye laser system and pressure tuning the reader is referred to Hansch and co-workers.¹³³⁻¹³⁵

With a dye solution of 2 gm/ ℓ of 7-diethylamino-4-trifluoromethyl coumarin in dioxane, the dye laser output at 4863\AA was frequency doubled in a lithium formate monohydrate crystal (Lasermetrics, $1 \times 1 \times 1 \text{ cm}$) which produced about $2 \mu\text{J}$ pulses of 5 nsec duration (FWHM). The line width was about 0.5 cm^{-1} (0.12\AA) which corresponds to $\Delta\omega = 1.5 \times 10^{10} \text{ sec}^{-1}$. When the beam was focused to about 0.5 mm waist diameter inside the fluorescence cell, the intensity approximated 0.2 MW/cm^2 . Substituting for $\Delta\omega$ and $I_1 = I_2 = 2 \times 10^5 \text{ W/cm}^2$ into eq. (80) we obtain for the transition rate $R_{12} = 56 \text{ sec}^{-1}$.

An order of magnitude of the fluorescence signal could then be estimated knowing that in the volume traversed by the two beams ($\sim 2 \times 10^{-3} \text{ cm}^3$), the number of H-atoms produced by a 3 mJ/pulse laser beam at 299.1 nm in 1 torr H_2CO is 1×10^{12} atoms. The number of atoms excited per 5 nsec pulse is therefore $56 \times 5 \times 10^{-9} \times 10^{12} \approx 2.8 \times 10^5$ atoms. With an overall detection efficiency of 1×10^{-4} , one should be able to detect 28 photons per pulse.

E. H_α DETECTION AND ELECTRONIC PROCESSING SYSTEM

Two solar blind photomultiplier tubes (PMT) were used to detect H_α photons at 1215.7\AA . The first one used throughout experiments on resonance fluorescence detection and spectroscopy was an EMI PMT (model G26E315) with a B25FV radiation shield. This has a C_5I

photocathode and LiF window 7/8 in. wide with a typical rise time of 10 nsec and ~15% quantum efficiency at 1215.7 Å. The second PMT was an EMR (model 542G-09-18) with a CsI photocathode and MgF₂ window also 7/8 in. wide; the typical risetime was 10 nsec and measured quantum efficiency ~19% at 1215.7Å. This PMT was used in experiments on resonance absorption and two-photon excited H_α fluorescence detection. Both PMT's offer a current amplification of 10⁶ at 3 kV applied bias voltage.

Reduction of scattered light was achieved using one or sometimes two Lyman-α interference filters supplied by ARC (model 122-VN). These filters have 8-9% transmission at 1215.7Å with 150Å bandwidth (FWHM).

The current output of the PMT was converted to a voltage through a load resistor, and then digitized by a Tektronix R-7912 transient digitizer with 512x512 channels. A PDP-11 computer equipped with WDI software was then used for signal averaging and analysis. The H_α fluorescence or absorption traces were then plotted on an x-y plotter interfaced with the computer.

F. GAS HANDLING SYSTEM

A standard glass vacuum line similar to the one shown in figure 10 was used for gas handling and for evacuating the fluorescence and absorption cells. Another glass vacuum line with a mechanical pump was separately used to evacuate the H_α resonance lamp and the copper tubing leading to the He/H₂ gas mixture source. A liquid N₂ trap between the mechanical pump and the glass manifold prevented oil back diffusion.

The resonance lamp and the tubing leading to the gas source were typically kept under vacuum when not in use, and a system of a metering valve and a flow meter were used to control gas pressure and flow rate. The flow rate was measured using a Tri-Flat (1/16 in.) flow meter with a stainless steel float calibrated in the range 20-300 std. cc/min. The pressure was read using a capacitance manometer as described in Chapter III.

G. RESONANCE FLUORESCENCE CELL

This was made out of a cubic aluminum block 10 cm wide and drilled on five sides. Two opposite sides were sealed with Torr-Seal epoxy resin to quartz windows at Brewster angles for the UV laser excitation beam, and a third side was sealed to the H α resonance lamp while the opposite side was sealed to a Wood's horn connected to the vacuum line for cell evacuation. The Wood's horn was painted black in order to trap the vacuum UV radiation. The fifth side at right angles to both radiation sources was sealed to the PMT tube through an O-ring flange and served as the fluorescence detection port. A MgF₂ window was sealed very close to the center of the cell in order to minimize the attenuation of H α fluorescence by the gas flowing through the cell (formaldehyde has an absorption coefficient $\alpha = 0.4 \text{ cm}^{-1}\text{torr}^{-1}$ at 1215.7Å which is quite appreciable). The volume between the PMT tube and the MgF₂ window was suitable for placing baffles with variable hole dimensions which were used to reduce scattered light. This volume was always kept under vacuum ($\sim 10^{-6}$ torr) in order to minimize any further attenuation of H α fluorescence by water vapor. The aluminum cell and the baffles were all anodized black.

H. RESONANCE ABSORPTION CELL

The absorption cell was made out of 15 cm long glass tubing 1 in. O.D. and sealed on both ends to quartz windows at Brewster's angles to the UV excitation beam. At the center and perpendicular to that two MgF₂ windows were sealed ~2.5 cm apart, one of them was sealed to the H_α resonance lamp and the other served as the detection window. Two glass tubes connected the cell into the vacuum line thus serving as entrance and exit for the gas.

A black cylinder 5 cm in diameter and 15 cm long enclosed a system of baffles and an H_α interference filter was placed between the MgF₂ window and the PMT and was continuously flushed with dry N₂. The baffles were cut with parallel rectangular holes whose dimensions varied as their distance from the center of the absorption cell, thus allowing the detector to view the volume traversed by the UV laser beam only. This was necessary in order to enhance the absorption signal and also to cut down UV scattered light which proved to be rather severe.

I. TWO-PHOTON EXCITATION CELL

This was the same as the fluorescence cell used for subsequent work on IR detection and is described in Chapter III. The only difference is the use of MgF₂ instead of NaCl windows for H_α line transmission.

J. H_α RESONANCE LAMP

The lamp was modeled after that of Davis and Braun¹³⁶ and was basically a pyrex glass tubing (18 cm long and 13 mm O.D.) with two side arms serving as entrance and exit for the H₂/He gas mixture flowing through. One end was sealed through a MgF₂ window into an O₂-gas

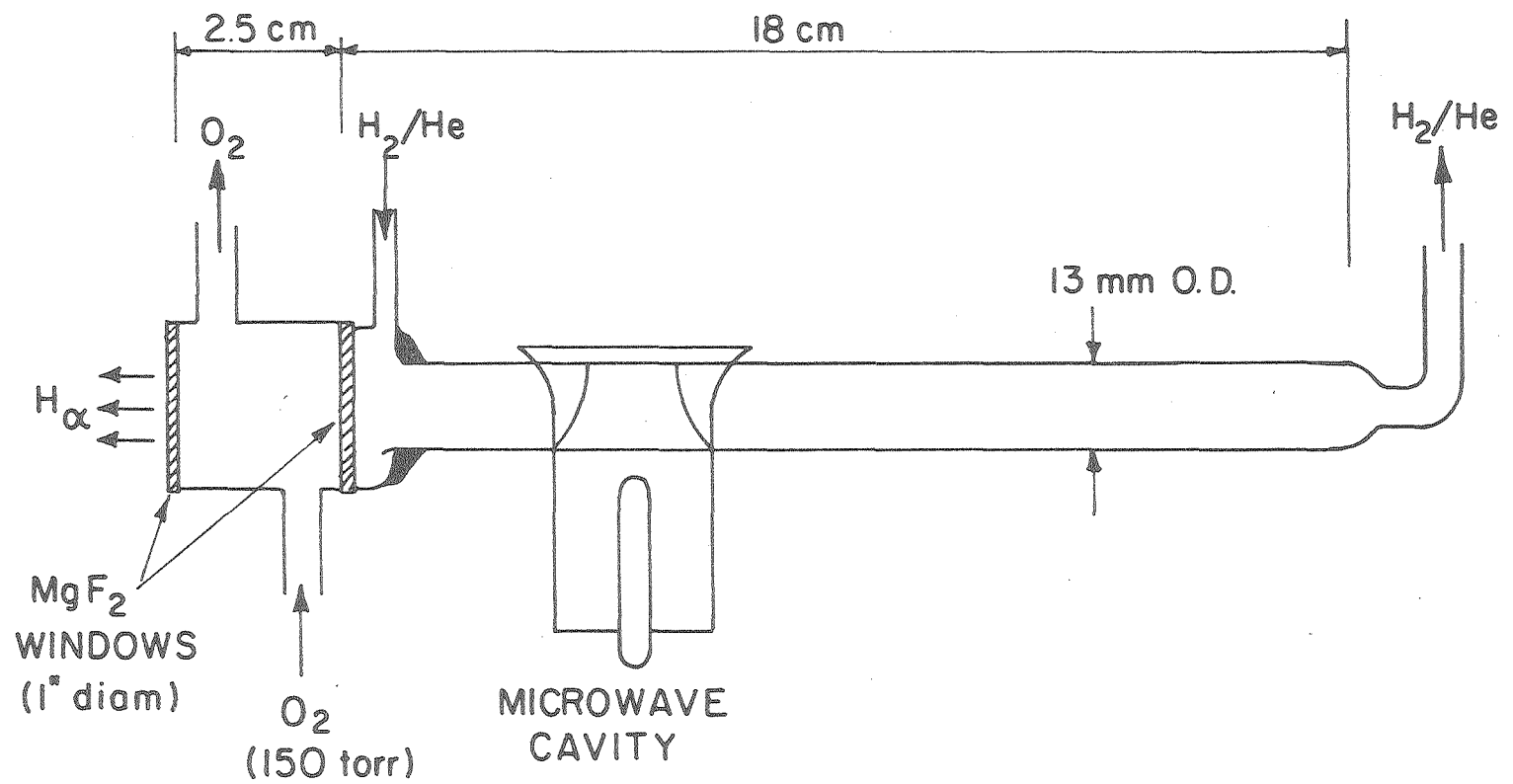
filter made out of 2.5 cm long pyrex tubing and 2.5 cm O.D., which was subsequently sealed to another MgF₂ window serving as the radiation output side. The whole assembly was then sealed to the fluorescence or absorption cell and kept under vacuum (high vacuum Torr-Seal epoxy resin supplied by Varian was used in all cases).

The H_α photons were produced using an electric discharge excited by a Microwave generator oscillating at 2450 MHz coupled to a 5 cm long x 2.5 cm O.D. cylindrical cavity through a 1 m long cable. The microwave generator was supplied by Raytheon (model) and the cavity was an Evenson-Broida type supplied by the Physical Chemistry Division, NBS, Washington, D.C.

The resonance lamp was originally operated by flowing 2% H₂/He gas mixture through at 1 torr pressure and 50 std. cc/min flow rate as recommended by Davis and Braun¹³⁶ for maximum output power. For reasons to become obvious below the lamp was slightly modified and operated at 0.1 to 1.0 torr of ultra high pure He (UHP 99.999% purity) purchased from Matheson Gas Products company. The microwave generator was normally run in the power range 40-80 watt and the discharge was brought very close to the output window in order to minimize resonance trapping which leads to a reversal in the resonance line. Figure 41 shows a schematic of the lamp used and conditions under which it was operated.

The O₂-gas filter was normally operated with 150 torr of O₂ gas (99.5%, Matheson) or 1 atm dry air flowing through.

Figure 41. Schematic of the H_{α} resonance lamp.



XBL788-5647

Fig. 41.

K. RESONANCE FLUORESCENCE AND LAMP PERFORMANCE

Several attempts were originally made towards measuring the appearance rates of H-atoms in formaldehyde using H_{α} resonance fluorescence detection. Here, the lamp was operated according to Davis and Braun¹³⁶ at 1 torr of 2% H_2 in He and 50 Std. cc/min flow rate. Under those conditions, the lamp is reported to deliver 0.76×10^{15} photons/sec at 1215.7Å. Using a tunable dye laser (Chromatix-CMX-4) with an output energy of 0.2 mJ/pulse (in the range 290-305 nm) passed five times through 1 torr H_2CO in the fluorescence cell, it was calculated that under the conditions of detection geometry described in sections E and G above (PMT gain = 10^6 , overall quantum efficiency = 9×10^{-4}), a current of $\sim 10^{-9}$ amp would develop across the PMT tube. Since the PMT tube background current is less than 10^{-10} amp under the same gain conditions, a detectable signal could be seen if the scattered light noise were effectively minimized. However, no signal was observed even upon averaging of 10,000 laser shots. The same attempts were also repeated using a N_2 laser delivering 10 mJ/pulse at 337.1 nm without success.

Suspecting a reversal in the H_{α} line due to resonance trapping from a possible high H-atom concentration produced in the lamp, the lamp was later operated using UHP He (99.999% purity with $H_2 < 1$ PPM) instead, but no signal was detected.

Stief and co-workers¹³⁷ were able to measure the decay rates of H atoms in H_2CO following photolysis by a flash lamp which delivered 318 J/pulse through resonance fluorescence detection. Here, the signal-to-noise ratio obtained was typically ~ 7 for 30 flashes through a mixture of 0.15 torr H_2CO plus 25 torr Ar at ~ 10 kHz post detection

electrical bandwidth. Though the flash lamp output energy was not monochromatic, an appreciable fraction is emitted in the wavelength range 1700-1800 where H₂CO absorbs considerably more strongly than in the near ultraviolet (the absorption coefficient of H₂CO at 175 nm is $2 \text{ cm}^{-1}\text{torr}^{-1}$ (Refs. 138,139) compared with $\sim 5 \times 10^{-4} \text{ cm}^{-1}\text{torr}^{-1}$ near 300 nm).

Given the limitations mentioned above, it was found necessary to examine the H_α resonance lamp performance as a function of several parameters including: lamp design, H₂/He concentration ratio, H₂/He pressure, gas flow rate, and the position and power level of microwave discharge.

1. Spectroscopic Apparatus

A moderately high resolution Vacuum Ultraviolet monochromator was used to study the H_α resonance line profile and lamp spectrum as will be shown below. The monochromator was a McPherson 3-meter (model 241) with a synchronous multispeed motor drive. The grating was 65x150 mm ruled with 1200 lines/mm, MgF₂-coated, and blazed at 2960Å. Used in second order, the dispersion was typically 2.8 Å/mm thus offering a resolution of $\sim 0.02 \text{ Å}$ (1.5 cm^{-1}) when the entrance and exit slits were set $\sim 8 \mu$ wide. The resonance lamp was sealed to the entrance slit through a suitable flange and the PMT was positioned on the exit slit through another flange. The PMT output current was measured using a picoammeter, and the results of the study are discussed below.

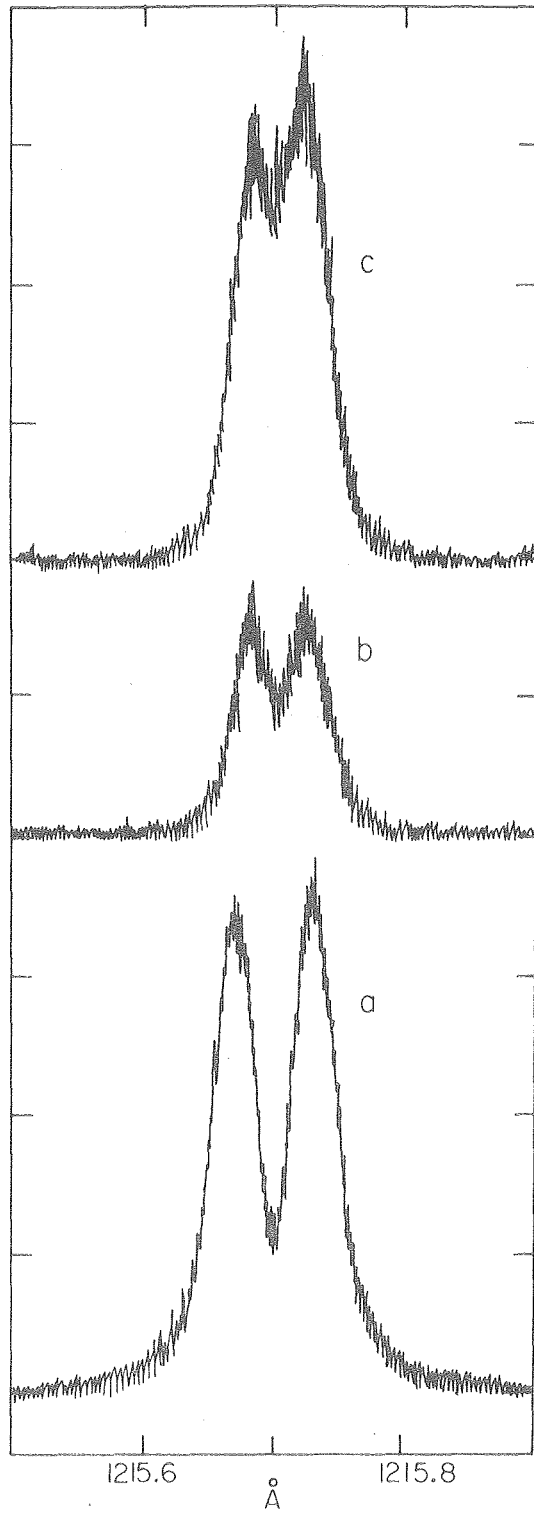
2. Resonance Line Profile

When the lamp was operated at 1 torr of 1.4% H₂ in He at 50 Std. cc/min, the resonance line at 1215.7Å was found to be completely reversed. It was even almost completely reversed when grade-A He gas (0.1% H₂) flowed through the lamp at 0.1 torr pressure and same flow rate as shown in figure 42a; here, the O₂-gas filter was kept under vacuum. The effect of O₂-gas flowing at 150 torr pressure on the transmission of the line is shown in figure 42b. It is seen that the O₂-filter reduces the transmitted intensity at the edges of the line with a negligible reduction at the line center. This is expected since O₂ has a very low absorption cross section ($\sim 1 \times 10^{-20}$ cm²).¹⁴⁰

When the microwave discharge was brought very close to the MgF₂ output window, the reversal was rather reduced and the intensity at the line center was improved as shown in figure 42c. This, however, adversely affected the transmission of the MgF₂ window, and after half an hour it was necessary to replace it with a new one.

With UHP He (H₂ < 1 ppm) used instead of grade-A He, the line profile improved significantly especially when the pressure was reduced to 0.1 torr and the flow rate set at 100 Std. cc/min as shown in figure 43. Within the spectral resolution of 0.017Å (1.5 cm⁻¹), the line was observed unreversed. This indicates a nearly complete absence of reversal since the Doppler width is 1.02 cm⁻¹. The effect of UHP He pressure on line intensity was also studied keeping the microwave discharge 1 cm away from the MgF₂ window (in order to increase its transmission lifetime). It was found that the line intensity increases by at least a factor of 5 when the pressure was decreased

Figure 42. H_{α} resonance line profile obtained for (a) 0.1 torr of grade-A He ($H_2 \approx 0.1\%$) flowing at 50 Std. cc/min with the O_2 -filter under vacuum, (b) same as in (a) except for flowing 150 torr O_2 in the O_2 -filter, and (c) same as in (b) except for having the microwave discharge almost hitting the MgF_2 output window. Spectral resolution was 0.017Å.



XBL 789-57 29

Fig. 42.

Figure 43. H_{α} resonance line profile obtained when the lamp was operated at 0.1 torr UHP He flowing at 100 Std. cc/min. Dry air at 1 atm pressure flowed through the O_2 -filter. The spectrum was taken at 0.017Å spectral resolution.

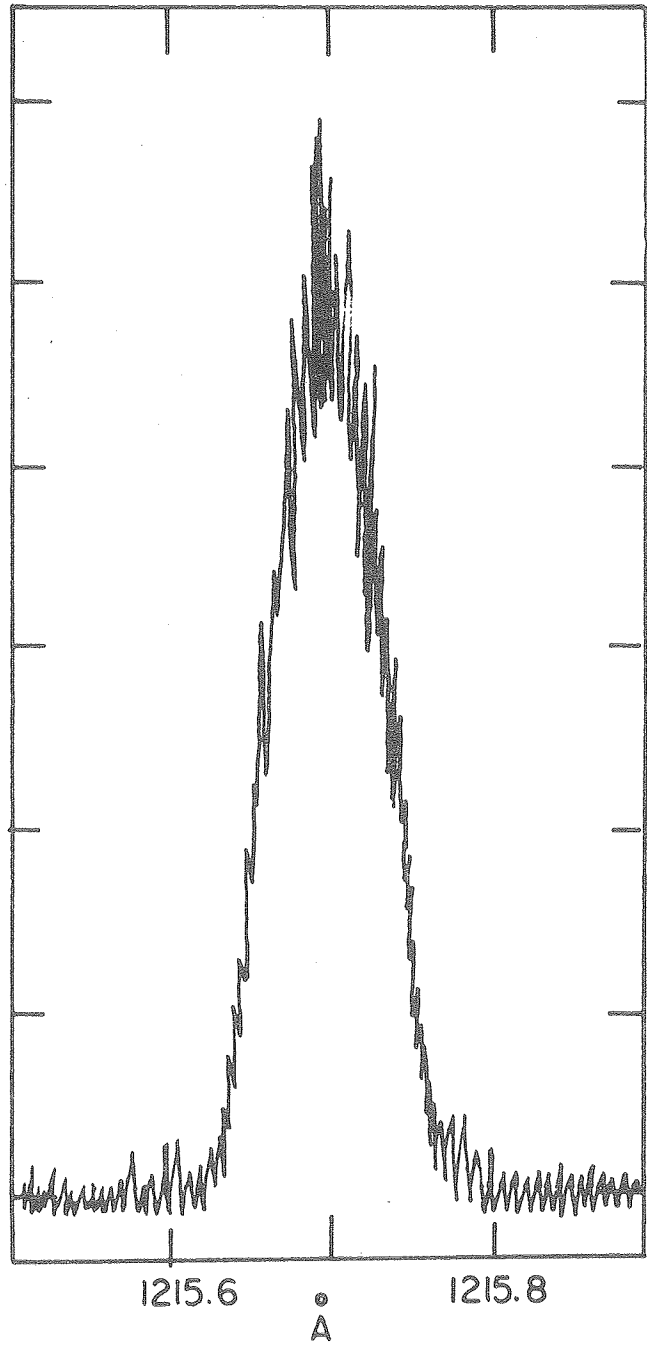


Fig. 43.

from 4.0 down to 0.1 torr. Below 0.1 torr, the intensity decreases until the lamp finally turns off at pressures below 60μ .

The variation of line intensity with microwave power was also examined and found to be linear in the power range 20-100 watt. The lamp was normally operated at 80 watt power, for at 100 watt the discharge covers the whole length of the lamp including the MgF_2 window.

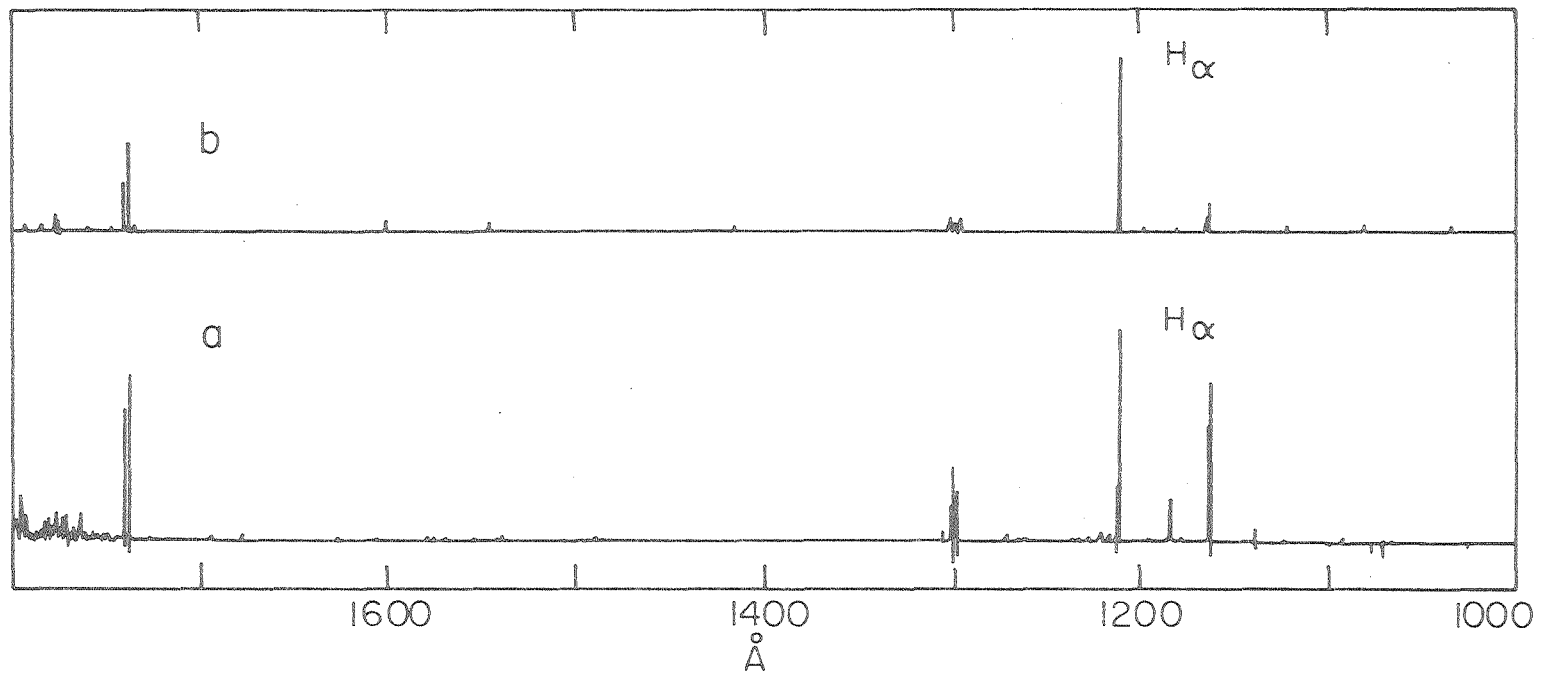
3. Resonance Lamp Spectrum

Examined over the wavelength range 1000-1800 Å, the lamp spectrum consisted of several sharp lines superimposed over a continuum of ~1% intensity. This is shown in figure 44a where the spectrum was obtained for 0.1 torr UHP He with the O_2 -filter kept under vacuum. Figure 44b shows the spectrum with dry air flowing at 1 atm through the gas filter. It is seen that the O_2 -filter effectively absorbs most of the lines with a minimal effect on the H_α resonance line.

4. H_2CO Absorption Coefficient at 1215.7Å

The attenuation of H_α radiation by H_2CO was examined as a function of gas pressure. Here, the monochromator was set at the center of the resonance line, the O_2 -filter evacuated, and the relative light transmission with and without a certain pressure of H_2CO inside the gas filter measured by monitoring the PMT output current. The results are indicated in Table XVII yielding an absorption coefficient: $\alpha = 0.39 \pm 0.04 \text{ cm}^{-1}\text{torr}^{-1}$. This is clearly rather high and any fluorescence or absorption cell design should take that into account.

Figure 44. H_{α} resonance lamp spectrum obtained in the wavelength range 1000-1800Å. The lamp was operated at 0.1 torr UHP He flowing at 100 Std. cc/min. Spectrum (a) was taken with O_2 -gas filter under vacuum while (b) represent the spectrum with dry air flowing at 1 atm pressure. The lamp was fitted with MgF_2 output window.



XBL 789-5731

Fig. 44.

Table XVII. H₂CO absorption coefficients for H_α resonance line at 1215.7Å as a function of gas pressure. Path length = 2.5 cm.

P _{H₂CO} (torr)	Current (I × 10 ¹⁰ amp)	$A = \ln \frac{I_0}{I}$	Absorption Coefficient (cm ⁻¹ torr ⁻¹)
0	0.47	0	--
0.15	0.40	0.16	0.43
0.51	0.30	0.45	0.35
1.30	0.13	1.25	0.40
5.00	0.01 ^a	3.9	(0.3)

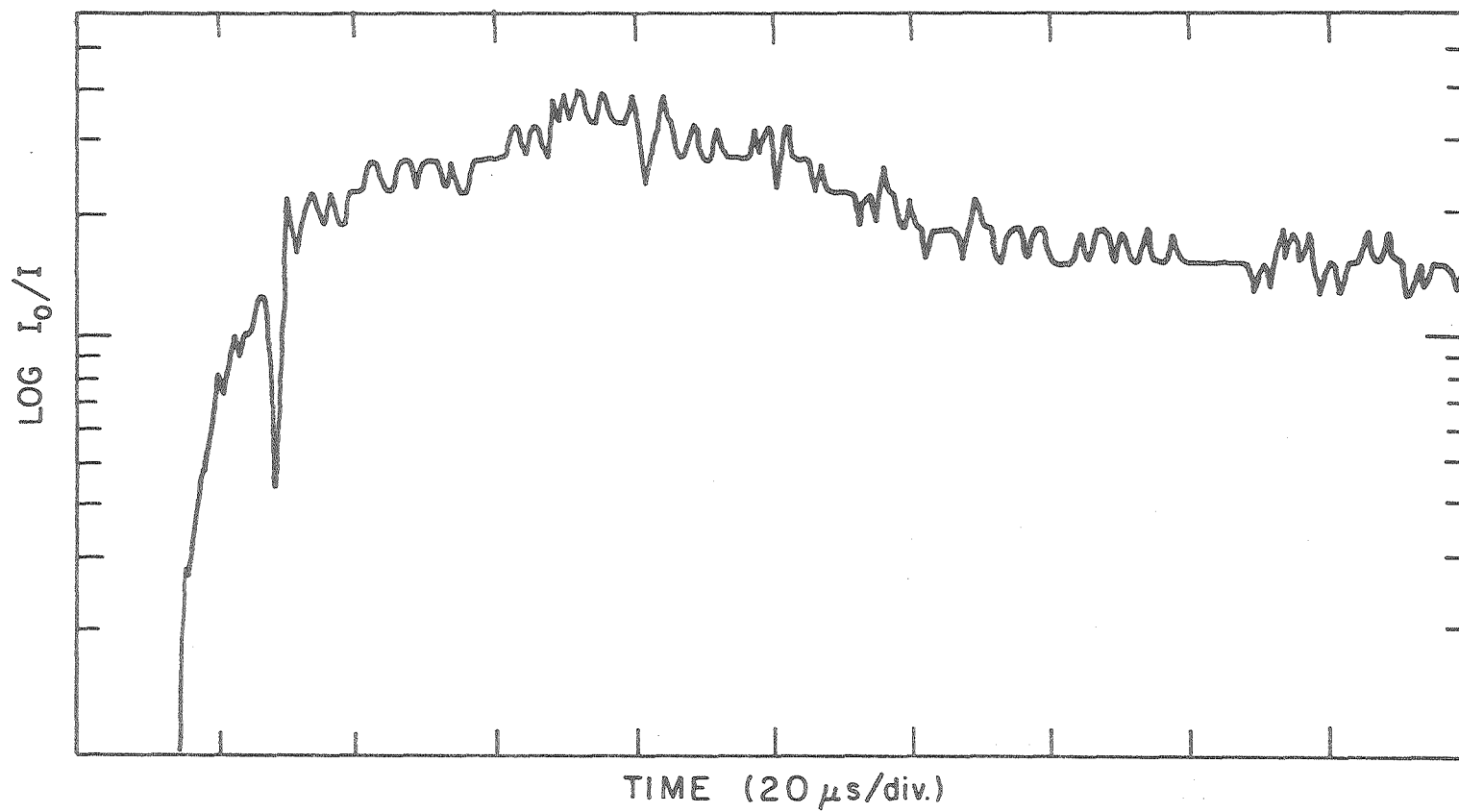
^aThe current measured at 5.00 torr H₂CO was too low and well within the maximum sensitivity of the picoammeter used of 0.5 picoamp. The uncertainty in the absorption coefficient at 5.00 torr is therefore high and will be ignored.

L. DETECTION BY RESONANCE ABSORPTION

Having the resonance lamp operated at optimal conditions with no line reversal, the resonance absorption technique was attempted to measure the H-atom appearance rates in formaldehyde. The choice over resonance fluorescence was dictated by a better prospect of obtaining a detectable signal and to avoid the possible efficient quenching of H γ fluorescence by formaldehyde (as discussed in Section C before) which tends to attenuate the signal considerably.

Using the output of a tunable dye laser (chromatix-CMX-4) tuned to the peak absorption of H₂CO at 303.5 nm ($\alpha \approx 2 \times 10^{-3} \text{ cm}^{-1} \text{ torr}^{-1}$), it was estimated that a beam of 0.25 mJ/pulse energy effectively passed 5 times within the absorption cell containing 1 torr of H₂CO would produce 2×10^{12} H atoms in a rectangular volume of 0.24 cm³. (This is calculated assuming 50% radical quantum yield in H₂CO). Now, if the absorption cell was designed such that the detector would only view the area in which H-atoms were produced and not the whole cross section illuminated by the resonance lamp, an absorption signal of 3% should be observed. Here, the absorption cross section of H for H α photons is $\sim 300 \text{ \AA}^2$ as measured by Michael and Weston¹⁴¹ ($\alpha \approx 1000 \text{ cm}^{-1} \text{ torr}^{-1}$). Figure 45 shows a semitogarithmetic trace obtained for 0.52 torr H₂CO averaged over 10,000 laser shots. This was observed with a postdetection electrical bandwidth of 10 kHz. Many further attempts were carried out to improve the time resolution by minimizing laser scattered light but failed. Tuning the dye laser over the different absorption peaks of H₂CO in the wavelength range 290-305 nm did not help much, however.

Figure 45. Semi-logarithmic trace of H_{α} resonance absorption obtained following photolysis of 0.52 torr H_2CO at 303.5 nm. The trace is an average of 10,000 laser shots.



XBL789-5732

Fig. 45.

Next, the higher laser output at 299.1 nm obtained by Raman shifting the Nd:YAG fourth harmonic in H₂ gas was used. The pulse energy was typically ~3 mJ/pulse, so with the absorption coefficient of H₂CO = $5 \times 10^{-4} \text{ cm}^{-1} \text{ torr}^{-1}$, a factor of 2.5 increase in the H-atom concentration to $\sim 5 \times 10^{12}$ atoms is estimated, using the same geometry mentioned above. The signal obtained however was not enough to enhance the time resolution as desired.

The Nd:YAG fourth harmonic at 266 nm was also used for H₂CO photolysis. Here the energy was 25 mJ/pulse, and the absorption coefficient was measured as $4 \times 10^{-5} \text{ cm}^{-1} \text{ torr}^{-1}$. Since this wavelength corresponds to an excitation energy well beyond the dissociation threshold for two H-atoms ($\text{H}_2\text{CO} \rightarrow 2\text{H} + \text{CO}$), the H-atom concentration could be slightly increased to 7×10^{12} atoms in the same geometry. The results were not much better than seen before.

At this stage, it was thought that photodissociation of H₂CO may produce H-atoms with high translational energy thus rendering their absorption only at the edge of the resonance line. Therefore, in order to Boltzmannize the H-atom velocity distribution, a mixture of H₂CO and Ar was used. With the pressure of Ar varied between 1 and 25 torr, no improvement was noticed. Later, the resonance lamp was operated at higher H₂/He pressure to broaden the resonance line with no success. It is not conceivable that H-atoms are photoproduced with high translational energy such that their absorption line is completely attenuated at the center of resonance line. Since the H Doppler width is 1.02 cm^{-1} at 300°K, the translational temperature required to broaden the absorption line by a factor of 10 is

30,000⁰K, corresponding to a translational energy of 45 kcal/mole.

At 300 nm wavelength of excitation, the energy available for radical products (H + HCO) is only ~8.5 kcal/mole, and how much of that retained by hydrogen is yet to be known.

M. DOPPLER-FREE TWO-PHOTON EXCITED H_α FLUORESCENCE

An experiment based on this technique was carried out with the prospect of measuring 28 detectable photons per laser pulse following laser photolysis of 1 torr H₂CO at 299.1 nm (as described in section D above). Great care was taken to have the photolysis beam aligned very well with the two-photon dye laser excitation beam, to bring the interaction region to within 2 mm of the MgF₂ window, and to slowly pressure tune the dye laser. Dry nitrogen was also kept flowing through the volume enclosed by the PMT tube, the H_α filter, and the MgF₂ window in order to displace any water vapor. Again, no detectable signal was observed during the several attempts made.

It should be noted here that our dye laser system was at a considerable disadvantage compared with that of Hansch and co-workers.¹²¹⁻¹²³ For due to the lack of an external etalon (a confocal Fabry-Perot interferometer), the dye laser line width was measured to be 2.4 GHz compared with only 150 MHz for the system used by Hansch. Since the transition rate is inversely proportional to the laser line width, as is clear from eq. (80) above, the signal we attempted to measure was apparently down by a factor of 16.

Another possibility for the lack of a detectable fluorescence signal could however be related to an efficient H_α fluorescence quenching by the more abundant H₂CO as discussed in Section C before. So it

appears that until a coherent H_{α} line source become available,¹⁴² the technique of three-photon ionization^{143,144} may be utilized for H-atom detection in formaldehyde as will be discussed in the next section.

N. DETECTION BY THREE-PHOTON IONIZATION: A PROPOSED EXPERIMENT

This technique has recently been used by Hurst, Nayfeh and Young¹⁴³ for detection of very low concentrations of alkali metal atoms in mixtures with rare gases. G. Bjorklund, et al.,¹⁴⁴ have also successfully applied it to detect H-atoms in H_2/He gas mixtures. Here, the H(1S-2S) transition was resonantly enhanced through two-photon absorption followed by a third photon absorption thus resulting in ionized atoms. The 1S-2S transition was excited with two photons: one of fixed frequency ω_1 , at 266 nm which was the Nd:YAG laser fourth harmonic, and the other of tunable frequency ω_2 at 224 nm. The tunable source at ω_2 was obtained by summing up the second harmonic of a tunable dye laser at 283 nm with the Nd:YAG fundamental at 1.06 μ , and the dye laser was pumped with the second harmonic of the Nd:YAG laser. Absorption of a third photon at ω_3 then excites the atom from the 2S state to the continuum.

In the arrangement mentioned above, the laser powers used were typically 1 MW peak power at ω_1 (6 nsec pulses of 1 cm^{-1} bandwidth) and 10-20 kW peak power at ω_2 (4 nsec pulses of 1 cm^{-1} bandwidth). The results indicate that the ionization signal is linear with H-atom concentration, and that the sensitivity covers a dynamic range over four orders of magnitude ($3.5 \times 10^9 - 1.5 \times 10^{14}$ atoms/cm³). The time resolution is also reported to be ~10 nsec.

Given the information mentioned above, an experiment could be designed accordingly to measure the appearance rates of H-atoms following photolysis of formaldehyde in the near ultraviolet (330-266 nm). Now, since such a measurement requires monitoring the H-ion signal at successive time intervals following the photolysis laser pulse, the probe laser frequencies should be chosen such that formaldehyde does not absorb. H_2CO , for example, has no absorption bands in the wavelength range 260-180 nm. Therefore, the utility of two probe laser sources in this region becomes desirable. In principle, an excimer laser (KrF) source at 249 nm in conjunction with a tunable frequency-doubled dye laser source at 238 nm may be used. It should be noted, however, that even though excimer lasers deliver enough peak powers typically 5-100 MW in 9-15 nsec pulses, they have many disadvantages. The rather large beam divergence (typically 3×7 mrad) makes it hard to collimate or focus properly, the linewidths are $\sim 2-5 \text{ \AA}$ (over 32 cm^{-1} for KrF at 249 nm), and the jitter is within ~ 100 ns which makes it hard to synchronize with the other probe laser source. So if it proves hard to overcome these problems and in the absence of other laser sources in the region 250-200 nm, it may be necessary to try the same system used by Bjorklund, et al.,¹⁴⁴ where the two probe laser frequencies were at 266 and 224 nm.

In planning such an experiment, there are few problems that have to be overcome and the following points should be kept in mind:

1. At 266 nm, the absorption coefficient of H_2CO is $4 \times 10^{-5} \text{ cm}^{-1} \text{ torr}^{-1}$. Thus at 1 torr H_2CO , a beam of 1 MW peak power will produce 4×10^{11} H-atoms in a 1 cm pathlength assuming 50%

photodissociation. Now, if the beam is focused into 0.02 cm waist diameter, then the concentration of H-atoms within the interaction region of $\sim 10^{-3}$ cm³ will be 4×10^{14} atoms/cm³. This will contribute to the H-ion signal tremendously, and in order to eliminate this contribution (possibly through frequency modulation), the photolysis beam should be powerful enough to produce at least a comparable concentration.

2. Due to the high photon flux needed to enhance the H(1S-2S) two-photon transition, especially at 266 nm, two-photon absorption and three-photon ionization of H₂CO may occur to some extent. Three photon absorption at 266 nm excites formaldehyde well beyond the ionization threshold measured at 1140 Å.¹⁴⁵ This plus any hydrogen atoms produced as a result of photodissociation induced by two- and three-photon absorption may put a serious limitation on the H-ion signal to be detected following the photolysis laser pulse. It should perhaps be emphasized here that although the cross sections for such processes in formaldehyde may be low, the larger concentration of H₂CO molecules present in the ionization cell (H₂CO/H ratio is typically 100-1000 times) may offset a difference in their three-photon absorption cross sections.
3. In order to avoid or rather minimize two-photon absorption and three-photon ionization of H₂CO at the probe frequency (266 nm), it is necessary to lower the probe beam intensity by as much as allowed by the H-ion detection sensitivity. Bjorklund, et al.¹⁴⁴ indicate that at lower peak powers of 1 MW

at 266 nm and ~10 KW at 224 nm, with both beams focused into ~0.025 cm waist diameter ($\pi\omega_0^2 = 5 \times 10^{-4} \text{ cm}^2$), the lowest easily detectable H-ion signal corresponds to 3.5×10^9 H-atoms per cm^3 . Since the ionization signal was found to be linear with H-atom concentration up to 1.5×10^{14} atoms per cm^3 , then it is perhaps possible to reduce the probe laser intensity at 266 nm without sacrificing much detection sensitivity. This can be achieved of course by having a photolysis beam powerful enough to produce the highest H-atom concentration prior to firing the probe beams.

As an example, a photolysis laser source near 300 nm offering 20 MW/cm^2 will produce 1.5×10^{14} H-atoms/ cm^3 in 1 torr H_2CO (assuming an absorption coefficient $\sim 10^{-3} \text{ cm}^{-1} \text{ torr}^{-1}$, 1 cm path length, and 50% photodissociation yield). This could be achieved by focusing a 1 MW peak power laser beam into 0.12 cm waist diameter. Now, since the detection sensitivity has a dynamic range of $\sim 4 \times 10^4$, the three-photon ionization rate in H could therefore be reduced by as much. The three-photon ionization rate is however proportional to the square of laser intensity at 266 nm, so the intensity could be reduced by a factor as much as 200. This implies that the beam intensity at 266 nm could be reduced from 4 GW/cm^2 into 20 MW/cm^2 by focusing at ~0.12 cm waist diameter while keeping the other probe beam at 224 nm tightly focused to 0.025 cm waist diameter. This arrangement will certainly decrease multiphoton absorption by H_2CO quite appreciably thus rendering the experiment doable.

VI. DISCUSSION

A. APPEARANCE RATES OF MOLECULAR PHOTOPRODUCTS

The measured rates of appearance of molecular products following photolysis of formaldehyde in the UV indicate the following:

1. At 354.7 nm (4_0^1 band), the rates vary linearly with gas pressure in the range of 0.1 to 5.0 torr and to within experimental error extrapolate to zero at zero pressure.
2. The rates demonstrate a deuterium isotope effect and follow the order $\text{H}_2\text{CO} > \text{HDCO} > \text{D}_2\text{CO}$. (See chapter IV and table XV for values of measured rates).
3. At the same wavelength and in the pressure range mentioned above, the rates are slower than the corresponding decay rates of the excited singlet, a result which is in agreement with that of P. L. Houston²⁵ who measured rates at 337.1 nm. For example, the decay rates of the excited singlet in H_2CO populated at 354.7 nm vary between $9 \mu\text{sec}^{-1}$ at 0.2 torr and $14 \mu\text{sec}^{-1}$ at 2.5 torr¹⁵ while, on the other hand, the dissociation rates (CO appearance rates) vary between $0.42 \mu\text{sec}^{-1}$ at 0.21 torr and $4.40 \mu\text{sec}^{-1}$ at 2.5 torr. The singlet decay rates in HDCO populated at 352.9 nm (4_0^1 band) are within $7\text{-}8 \mu\text{sec}^{-1}$ for the pressure range 0.20 to 2.00 torr,¹⁷ where as the dissociation rates are only $2.6 \mu\text{sec}^{-1}$ at 1.65 torr and $3.5 \mu\text{sec}^{-1}$ at 2.50 torr as measured for the same band at 354.7 nm (see table IX). In D_2CO , the singlet decay rates vary from $1.25 \mu\text{sec}^{-1}$ at 1.0 torr to $2.9 \mu\text{sec}^{-1}$ at 2.5 torr¹⁵ compared with CO production rates of $0.7 \pm 0.2 \mu\text{sec}^{-1}$ at 1.0 torr and 1.7 ± 0.2 at 2.5 torr.

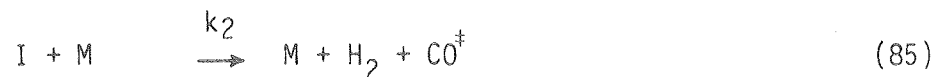
4. The dissociation rate constants measured for H_2CO and D_2CO at 354.7 nm are approximately equal to those reported by P. L. Houston²⁵ at 337.1 nm (see table XV). In other words, the dissociation rates appear to be insensitive to an increase of $\sim 1500 \text{ cm}^{-1}$ in the vibrational excitation of the excited singlet (4.2 kcal/mole). The decay rates of the excited singlet, on the other hand, increase by a factor of 3 for the same gas pressure range (~ 0.1 torr).^{1,15,17}
5. At 299.1 nm, H_2CO dissociates with a rate constant at least an order of magnitude higher than those measured at either 354.7 nm or 337.1 nm. At the lowest pressure of 0.18 torr, the rate was measured as $2.8 \pm 1.5 \mu\text{sec}^{-1}$ corresponding to $16 \pm 7 \mu\text{sec}^{-1} \text{ torr}^{-1}$ value for the rate constant (see table VII). The uncertainty in the measurement is rather large due to the very low signal-to-noise ratio of fluorescence traces obtained. It should be pointed out here that it was not possible to ascertain the actual pressure dependence of those rates since the measurements could not be extended to lower pressures. So it is possible that dissociation occurred promptly upon decay of the excited singlet. The vertical excitation energy at 299.1 nm (33.435 cm^{-1}) corresponds to 95.6 kcal/mole which is 10.8 kcal/mole (3770 cm^{-1}) above that at 337.1 nm.
6. In mixture of 0.5 torr H_2CO with foreign gases in the pressure range 0.1 to 4.5 torr, the measured rates following photolysis at 354.7 nm vary linearly with foreign gas pressure. The measured rates in units of $\mu\text{sec}^{-1} \text{ torr}^{-1}$ were: 1.04 ± 0.26 for He,

1.28 ± 0.20 for Ar, 1.45 ± 0.24 for Xe, and 1.40 ± 0.48 for NO.

The corresponding gas kinetic collision rate constants are calculated for the same mixtures as: 14.9 for He, 8.5 for Ar, 8.3 for Xe, 9.5 for NO, and 10.6 for H₂CO collision partners at room temperature (units of $\mu\text{sec}^{-1} \text{ torr}^{-1}$). The molecular diameters used were Lennard-Jones corresponding to 2.6 Å for He, 3.4 Å for Ar, 4.1 Å for Xe, 3.6 Å for NO, and 4.0 Å for H₂CO.¹⁴⁶

The measured dissociation rates would therefore represent collision efficiencies of: 0.07 for He, 0.15 for Ar, 0.17 for Xe, 0.15 for NO, and 0.16 for H₂CO.

7. The slower dissociation rates measured at 354.7 and 337.1 nm compared with the decay rates of the excited singlet does therefore require the formation of an intermediate state (I) which subsequently dissociates upon collision into molecular products. The linear variation of dissociation rates with formaldehyde and foreign gas pressure is compatible with the following kinetic scheme:



where CO^\ddagger represents vibrationally excited CO products.

In this scheme, k_2 and k_3 represent summations over the product of rate constant times concentration for all collision partners and are only written as such for simplicity. Now, since the pulse duration

is much less than k_1^{-1} , the concentration of molecules in the excited singlet (A^*) is equal to αA where A is the concentration of ground state molecules and α is a proportionally constant. The decay of excited singlet is single exponential and is therefore given by

$$A^* = \alpha A e^{-k_1 t} \quad (87)$$

The time evolution of I is given by

$$\begin{aligned} dI/dt &= k_1 A^* - k_2 M I \\ &= \alpha k_1 A e^{-k_1 t} - k_2 M I \end{aligned} \quad (88)$$

Integrating over t and applying the boundary condition $I = 0$ at $t = 0$ yields

$$I = \frac{\alpha k_1 A}{k_1 - k_2 M} (e^{-k_2 M t} - e^{-k_1 t}) \quad (89)$$

Now, if the excited singlet decays at a much greater rate than that of the intermediate ($k_1 > k_2 M$), then at $t > k_1^{-1}$ the second exponential form would be close to zero and eq. (89) could be approximated as

$$I = \alpha A e^{-k_2 M t} \quad (90)$$

The differential equation for CO^\ddagger could be developed as

$$\begin{aligned} dCO^\ddagger/dt &= k_2 M I - k_3 M CO^\ddagger \\ &= \alpha k_2 A M e^{-k_2 M t} - k_3 M CO^\ddagger \end{aligned} \quad (91)$$

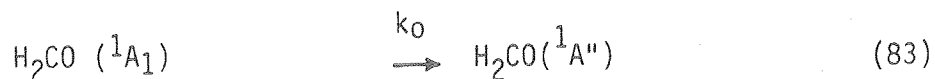
Integrating over t and setting $CO^\ddagger = 0$ at $t = 0$ finally yields

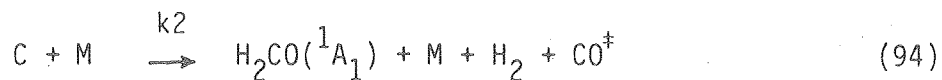
$$CO^\ddagger = \frac{\alpha k_2 A}{(k_2 - k_3)} (e^{-k_3 M t} - e^{-k_2 M t}) \quad (92)$$

Eq. (92) indicates that the fluorescence intensity of CO molecules monitored following photolysis of formaldehyde is a sum of a rising and falling exponential term. Since the rise (or appearance) of CO fluorescence is much faster than its decay ($k_1 \gg k_2$), then at longer times the fluorescence intensity will become a single exponential decay. A subtraction of this exponential decay portion from the total fluorescence should therefore yield a rise which is also single exponential. Thus from a semilogarithmic plot of fluorescence intensity against time, this subtraction procedure yields a straight line whose negative slope is the reciprocal of the rise (appearance) rate. A subsequent plot of appearance rates thus measured as a function of gas pressure should yield a straight line whose slope is the appearance rate constant (k_2).

The above analysis was adopted in this work and produced appearance rates which vary linearly with pressure thus confirming the above kinetic source.

8. In view of the proximity of the dissociation rate constants obtained for the rare gases (He, Ar, and Xe) to those of the parent molecule (H_2CO), the formation of a collision complex (between excited and ground state formaldehyde molecules) as a possible intermediate seems unlikely. This may be better understood by considering such a scheme as shown below.





Here, C represents the collision complex which dissociates upon collision into molecular products. Following a similar procedure to that given in the previous section, the excited singlet (A'') decays according to

$$A'' = \alpha A e^{-k_1 A t} \quad (90)$$

The variation of complex concentration with time is therefore given by

$$\begin{aligned} dC/dt &= k_1 A A'' - k_2 M C \\ &= \alpha k_1 A^2 e^{-k_1 A t} - k_2 M C \end{aligned} \quad (96)$$

When integrated over t, eq. (96) yields

$$C = \frac{\alpha k_1 A^2}{k_1 A - k_2 M} (e^{-k_2 M t} - e^{-k_1 A t}) \quad (97)$$

The differential equation for CO^\ddagger is finally developed as

$$\begin{aligned} d CO^\ddagger / dt &= k_2 M C - k_3 M CO^\ddagger \\ &= \frac{\alpha k_1 k_2 A^2 M}{k_1 A - k_2 M} (e^{-k_2 M t} - e^{-k_1 A t}) - k_3 M CO^\ddagger \end{aligned} \quad (98)$$

and when integrated over t yields

$$CO^\ddagger = \frac{\alpha k_1 k_2 A^2 M}{k_1 A - k_2 M} \left\{ \frac{e^{-k_1 A t}}{k_1 A - k_3 M} - \frac{e^{-k_2 M t}}{M(k_2 - k_3)} + \frac{(k_1 A - k_2 M) e^{-k_3 M t}}{M(k_2 - k_3)(k_1 A - k_3 M)} \right\} \quad (99)$$

It is clear from eq. (99) that the CO fluorescence intensity would yield a nonlinear variation of dissociation rates with gas pressure (M) contrary to what was found in this work. If, however, the rate of complex formation is much greater than the corresponding dissociation rate, that is, $k_1 A \gg k_2 M$, then the first exponential term in eq. (99) could be ignored. Thus, setting $k_1 A - k_2 M \approx R_1 A$ and $k_1 A - k_3 M \approx k_1 A$, eq. (99) reduces to

$$CO^\ddagger = \frac{\alpha k_2 A}{(k_2 - k_3)} e^{-k_3 M t} - e^{-k_2 M t} \quad (100)$$

which is identical with eq. (92) obtained for the previous kinetic scheme. This would nevertheless imply that the complete formation should occur at a time scale comparable to that of the decay of the excited singlet, which is very fast. Complex formation would also lead to scrambled isotopic products in cases where isotopically labeled formaldehyde molecules are selectively excited, contrary to experimental results. So on the basis of these arguments a complex is not likely to be the intermediate sought after.

9. In addition to the ground electronic state serving as a possible intermediate as discussed in Chapter II, the alternative decay of the excited singlet into the isometric form $\ddot{H}COH$ (hydroxymethylene) could not be overlooked as a possibility. Sodeau and Lee¹⁴⁷ have recently suggested this intermediate to explain their observation of some unidentified IR absorption bands, following photolysis of H_2CO/Ar and H_2CO/CO matrices at 12°K, suspected

of being caused by CH(OH)CO vibrations. The recent theoretical studies by Altman, et al.,⁵⁰ Lucchese and Schaefer,⁵¹ and also Goddard and Schaefer¹⁴⁸ place the ground state energy of hydroxymethylene about 46 kcal/mole above ground state H₂CO. Though this is well below the electronic excitation energy at 354.7 nm (~80.6 kcal/mole), the same calculations indicate an energy barrier to isometrization equal to 100.5 kcal/mole, or ~20 kcal/mole above the origin of the excited singlet. So, anticipating further and more generally optimized calculations which may bring the isometrization barrier close to the excited singlet origin, hydroxymethylene may be the intermediate state. Since such isometrization requires the migration of a hydrogen atom from carbon to oxygen in formaldehyde, the lower zero point energy for the deuterated molecules would probably raise the barrier to migration. The heavier deuterium atom also inhibits tunneling.

10. The larger dissociation rates observed for H₂CO at 299.1 nm over those at 354.7 and 337.1 nm may be understood in terms of the presence of an energy barrier to direct dissociation of the excited singlet. The barrier would then have to be placed between 337.1 and 299.1 nm (84.8 and 95.6 kcal/mole, respectively). One problem remains to be solved though and that is the equivalence of those rates measured at both 354.7 and 337.1 nm. The energy difference is about 1500 cm⁻¹ (4.2 kcal/mole) and it is not obvious why the rates would be equal since the thermal collision energy is only about 208 cm⁻¹ at room temperature.

11. The experiments carried out to measure the dissociation rates in other small carbonyls such as acrolein, propynal, ketene and cyclobutanone show that their photochemical behavior is almost certainly not analogous to that of formaldehyde. The dissociation rates were much higher for those molecules at the excitation energies indicated in table XV. Since the lower limits placed on collision induced rates are greater than gas kinetic, it is most likely that dissociation occurs collision-free.

B. CO ($v = 1$) DECAY RATES

The measured decay rates for the three isotopic species of formaldehyde agree to within experimental error with those reported by P. L. Houston²⁵ (see table XVI). Qualitatively speaking, the rates vary according to the frequency mismatch (ΔE) between the vibrational mode of formaldehyde with that of CO ($v = 1$) at 2143 cm^{-1} . For example, the decay rate constant in H_2CO is $(1.75 \pm 0.32) \times 10^3 \text{ sec}^{-1} \text{ torr}^{-1}$ and $\Delta E = +397 \text{ cm}^{-1}$; in HDCO the rate constant is $(7.3 \pm 0.3) \times 10^4 \text{ sec}^{-1} \text{ torr}^{-1}$ and $\Delta E = +22 \text{ cm}^{-1}$; whereas in D_2CO the rate constant is the highest $(1.15 \pm 0.10) \times 10^5 \text{ sec}^{-1} \text{ torr}^{-1}$ for $\Delta E = -17 \text{ cm}^{-1}$.

Ketene quenches CO ($v = 1$) at a rate constant equal $(1.14 \pm 0.20) \times 10^6 \text{ sec}^{-1} \text{ torr}^{-1}$ for which the vibrational frequency mismatch is only -9 cm^{-1} .¹⁴⁹

The larger molecules studied quench CO ($v = 1$) at a higher rate even though the frequency mismatch is quite large. Cyclobutanone, for example, exhibits a decay rate constant of $(1.38 \pm 0.24) \times 10^6 \text{ sec}^{-1} \text{ torr}^{-1}$ for which the frequency mismatch is $+327 \text{ cm}^{-1}$.

The larger number of vibrational normal modes apparently increases

the probability of accepting energy from CO ($v = 1$) Cis-2-butene quenches CO ($v = 1$) at a rate constant of $(1.35 \pm 0.26) \times 10^6 \text{ sec}^{-1} \text{ torr}^{-1}$ ($\Delta E = +483 \text{ cm}^{-1}$) and acrolein shows the highest rate constant $(2.02 \pm 0.22) \times 10^6 \text{ sec}^{-1} \text{ torr}^{-1}$ where $\Delta E = +361 \text{ cm}^{-1}$.

C. SUMMARY AND SUGGESTIONS FOR FUTURE WORK

The results discussed in this chapter indicate a photochemical behavior exhibited by formaldehyde which is different from other carbonyl compounds. The excited singlet state decays much faster than would otherwise be expected for such a small molecule. The density of states in the ground and triplet electronic states are too sparse near those of the excited singlet to enhance irreversible decay. The dissociation rates for molecular channel are much slower, on the other hand, and indicate the possibility of an energy barrier placed between 337.1 and 299.1 nm, perhaps at the radical channel dissociation threshold. The formation of a long-lived intermediate as a precursor for dissociation is obvious although the nature of it is far from resolved.

An extension of the measurements of dissociation rates to other energies of excitation is necessary. As more UV laser sources with enough power become available, such measurements could be made. For example, excimer lasers such as XeCl at 308 nm are available with perhaps enough power to enhance the time resolution necessary for such a measurement. An XeBr excimer laser source at 282 nm may become available soon in addition to other possible sources. The energy dependence of those rates would help identify whether the same mechanism for dissociation occurs at the higher energies or whether new dissociation channels open up. A measurement of dissociation rates for the radical

channel is also desirable and may be obtained through detection of H-atoms as described in chapter V. An alternative approach is detection of HCO radicals and the work is underway in this laboratory.

An experiment designed to look for hydroxymethylene as a possible intermediate could also be carried out. Singlet methylenes normally absorb in the visible (Ca. CH_2 absorbs at 589 nm),^{150,151} so hydroxymethylene may have an absorption band somewhere nearby. Probing for it by laser-induced fluorescence or by resonance absorption using a tunable dye laser source is therefore possible. The probe beam would have to follow the laser photolysis pulse by approximately the lifetime of the excited singlet state (typically about 70 nsec at 1 torr H_2CO and 354.7 nm).

A measurement of the dissociation rates in formylfluoride (HFCO, DF₂CO) is probably possible if one utilizes excimer laser sources such as KrF at 249 nm and ArF at 193 nm. The absorption coefficient for HFCO at 249 nm is certainly small ($\sim 6 \times 10^{-5} \text{ cm}^{-1} \text{ torr}^{-1}$)¹⁵² but the pulse energy provided by a KrF laser is high (100 - 200 mJ in 12-17 nsec pulses) which may render such experiments doable. At 193 nm, the absorption coefficient is much higher ($\sim 1.2 \times 10^{-3} \text{ cm}^{-1} \text{ torr}^{-1}$)¹⁵² and ArF laser pulse energies are also high enough (typically 40 - 100 mJ in 10 nsec pulses). Those measured rates for formylfluoride will certainly give a clue as to whether it exhibits the same dissociation mechanism as in formaldehyde. An examination of the energy distribution among both molecular products (HF and CO) would also be possible thus allowing the determination of how much of the original excitation energy end up in vibrational excitation of product molecules.

VII. REFERENCES

1. E. S. Yeung and C. B. Moore, J. Chem. Phys. 58, 3988 (1973).
2. A. P. Baronavski, A. Hartford, Jr. and C. B. Moore, J. Mol. Spect. 60, 111 (1976).
3. E. S. Yeung and C. B. Moore, Appl. Phys. Lett. 21, 109 (1972).
4. C. B. Moore, Acct. Chem. Res. 6, 323 (1973).
5. E. S. Yeung and C. B. Moore, J. Chem. Phys. 60, 2139 (1974).
6. J. Marling, J. Chem. Phys. 66, 4200 (1977).
7. A. P. Baronavski, J. H. Clark, Y. Haas, P. L. Houston, and C. B. Moore. Proceedings of the Second International Conference on Laser Spectroscopy, Eds. S. Haroche, et al., Springer-Verlag (1975), p. 259.
8. R. S. Berry and P. A. Lehman, Ann. Rev. Phys. Chem. 22, 47 (1971).
9. J. G. Calvert, J. A. Kerr, K. L. Demerjian, and R. D. McQuigg, Science, 175, 751 (1972).
10. D. M. Rank, C. H. Towness and W. J. Welch, Science, 174, 1083 (1971).
11. L. J. Steif, B. Donn, S. Glicker, E. P. Gentieu and J. E. Mentall, Astrophys. J. 171, 21 (1972).
12. J. C. Calvert and J. N. Pitts, Jr., "Photochemistry," John Wiley, and Sons, Inc. NY (1966), pp. 368-70.
13. B. A. DeGraff and J. G. Calvert, J. Am. Chem. Soc. 89, 2247 (1967).
14. R. D. McQuigg and J. G. Calvert, J. Am. Chem. Soc. 91, 1590 (1969).
15. J. C. Weisshaar, A. P. Baronavski, A. Cabello and C. B. Moore, to be published.
16. R. G. Miller and E. K. C. Lee, Chem. Phys. Lett. 33, 104 (1975).
17. R. G. Miller and E. K. C. Lee, J. Chem. Phys. 68, 4488 (1978).

18. D. A. Hansen and E. K. C. Lee, J. Chem. Phys. 63, 3272 (1975).
19. D. A. Hansen and E. K. C. Lee, J. Chem. Phys. 62, 183 (1975).
20. J. H. Clark, C. B. Moore and N. S. Noqar, J. Chem. Phys. 68, 1264 (1978).
21. J. H. Clark, Ph. D. Thesis, Department of Chemistry, University of California, Berkeley (1977).
22. G. K. Moortgat, F. Slemar, W. Seiler and P. Warnek, Chem. Phys. Lett. 54, 444 (1978).
23. R. S. Lewis, K. Y. Tang and E. K. C. Lee, J. Chem. Phys. 65, 2910 (1976).
24. R. S. Lewis and E. K. C. Lee, J. Phys. Chem. 82, 249 (1978).
25. P. L. Houston and C. B. Moore, J. Chem. Phys. 65, 757 (1976).
26. D. M. Hayes and K. Morokuma, Chem. Phys. Lett. 12, 539 (1972).
27. R. L. Jaffe, D. M. Hayes and K. Morokuma, J. Chem. Phys. 60, 5108 (1974).
28. R. L. Jaffe and K. Morokuma, J. Chem. Phys. 64, 4881 (1976).
29. A. P. Baronavksi, Ph. D. Thesis, Department of Chemistry, Univ. of California, Berkeley (1976).
30. D. C. Moule and A. D. Walsh, Chem. Rev. 75, 67 (1975).
31. V. A. Job, V. Sethuramen and K. K. Innes, J. Mol. Spect. 30, 365 (1969).
32. J. P. Byrne and I. G. Ross, Aust. J. Chem. 24, 1107 (1971).
33. A. C. Luntz and V. T. Maxson, Chem. Phys. Lett. 26, 553 (1974).
34. F. W. Birss, D. A. Ramsey and S. M. Till, Chem. Phys. Lett. 53, 14 (1978).
35. J. C. Brand and C. G. Stevens, J. Chem. Phys. 58, 3331 (1973).

36. J. E. Mentall, E. P. Gentieu, M. Kraus and D. Neuman, J. Chem. Phys. 55, 5471 (1971).
37. E. H. Van Veen, W. L. Van Dijk and H. H. Brongersma, Chem. Phys. 16, 337 (1976).
38. J. F. Gouyet and M. T. Prat, J. Chem. Phys. 64, 946 (1976).
39. J. C. Weisshaar and C. B. Moore, work in progress.
40. J. A. Pople and J. W. Sidman, J. Chem. Phys. 27, 1270 (1957).
41. E. R. Farnsworth, G. W. King and D. C. Moule, Chem. Phys. 1, 82 (1973).
42. K. Shibuya and E. K. C. Lee, (unpublished work).
43. R. Walsh and S. W. Benson, J. Am. Chem. Soc. 88, 4570 (1966).
44. A. Horowitz and J. G. Calvert, Int. J. Chem. Kinet., X, 713 (1978).
45. B. A. Ridley, J. A. Davenport, L. J. Stief, and K. H. Welge, J. Chem. Phys. 57, 520 (1972).
46. J. H. Clark, C. B. Moore and J. P. Reilly, Int. J. Chem. Kinet., to be published.
47. J. P. Reilly, J. H. Clark, C. B. Moore and G. C. Pimentel, to be published.
48. A. Horowitz, Fu Su, and J. G. Calvert, preprint.
49. W. R. Hindmarsch, S. A. Owen and E. L. Lewis, J. Phys. B. 7, 2570 (1974).
50. J. A. Altman, I. G. Csizmodia, K. Yates and P. Yates, J. Chem. Phys. 66, 298 (1977).
51. R. R. Lucchese and H. F. Schaefer, III. J. Am. Chem. Soc. 100, 298 (1978).
52. D. E. Klimek and M. J. Berry, Chem. Phys. Lett. 20, 141 (1973).

53. A. Yariv, "Quantum Electronics", 2nd ed., John Wiley and Sons, Inc., New York (1975), Chapt. 9 and 10.
54. E. Hecht and A. Zajac, "Optics," Addison-Wesley Publishing Co., Inc., Menlo Park, CA (1974) p. 261.
55. R. Goldstein, Laser Focus, Feb. 1968, p. 21.
56. R. L. Aggarwal and B. Lax, "Nonlinear IR Generation," Y. R. Shen, ed., Topics in Applied Physics, Vol. 16, Springer-Verlag, Berlin (1977) p. 32.
57. A. Yariv, "Introduction to Optical Electronics," Holt-Rinehart and Winston, Inc. New York (1971).
58. Z. J. Kiss and R. J. Pressley, "Crystalline Solid Lasers," in Laser Devices and Applications, ed. by I. P. Kaminov and A. E. Siegman, IEEE Press, New York (1973), p. 24.
59. M. M. Choy and R. L. Byer, Phys. Rev. B, 14, 1693 (1976).
60. F. Zernike, Jr., J. Opt. Soc. Am., 54, 1215 (1964).
61. W. R. Fenner, H. A. Hyatt, J. M. Kellam and S. P. S. Parto, J. Opt. Soc. Am., 63, 73 (1973).
62. N. Bloembergen, Am. J. Phys. 35, 989 (1967).
63. N. Bloembergen, G. Bret, P. Lallemand, A. Pine and P. Simova, IEEE J. Quant. Elect. QE-3, No. 5, 197 (1967).
64. R. W. Minck, W. Terhune and W. G. Rado, Appl. Phys. Lett. 3, 181 (1963).
65. P. Lallemand, P. Simova and G. Bret, Phys. Rev. Lett. 17, 1239 (1966).
66. L. Galatry, Phys. Rev. 122, 1218 (1961).
67. E. E. Hagenlocker and W. G. Rado, App. Phys. Lett. 7, 236 (1965).

68. P. V. Avizonis, A. H. Guenther, T. A. Wiggins, R. V. Wick and D. H. Rank, Appl. Phys. Lett. 9, 309 (1966).
69. "International Critical Tables of Numerical Data: Physics, Chemistry and Technology," Vol. 7, National Research Council, New McGraw Hill (1930), Index of Refraction data.
70. P. V. Avizonis, K. C. Junqing, A. H. Guenther, R. M. Heimlich and A. J. Glass, J. Appl. Phys. 39, 1752 (1968).
71. R. L. Bver and R. L. Herbst, "Parametric Oscillation and Mixing," in Topics in Applied Physics, Y. R. Shen, ed., Springer-Verlag, Vol. 16, Berlin (1977), p. 81.
72. R. Chiao and B. P. Stoicheff, Phys. Rev. Lett. 12, 290 (1964).
73. E. Garmire, F. Pandarese and C. H. Townes, Phys. Rev. Lett. 11, 160 (1963).
74. N. Bloembergen, "Nonlinear Optics," W. A. Benjamin, Inc., New York (1965).
75. Jack Finzi, Ph. D. Thesis, Department of Chemistry, Univ. of California, Berkeley (1975).
77. F. R. Arams, "IR to Millimeter Wavelength Detectors," Artech House, Inc. Dedham, Mass. (1973).
78. P. B. Fellegett, J. Opt. Soc. Am., 39, 970 (1949).
79. Mikael' A. Bramson, "IR Radiation: A Handbook for Applications," Plenum Press, New York (1968).
80. W. L. Wolfe, "Handbook of Military IR Technology," Office of Naval Research, Department of the Navy, Washington, D. C. (1965).
81. R. D. Hudson, Jr. and J. W. Hudson, ed. "IR Detectors," Dowden, Hutchinson and Ross, Inc. Stroudsburg, PA (1975).

82. H. Levinstein, Appl. Optics, 4, 639 (1965).
83. R. C. Jones, J. Opt. Soc. Am., 39, 327 (1949).
84. R. L. Williams, J. Appl. Phys. 40, 184 (1969).
85. L. Levi, "CRC Handbook of Tables of Functions for Applied Optics," CRC Press, Inc., Cleveland, Ohio (1974).
86. R. C. Jones, J. Opt. Soc. Am. 37, 879 (1947).
87. Z. J. Kiss and R. J. Pressley, "Crystalline Solid Lasers," in Laser Devices and Applications, ed. by I. P. Kaminow and A. E. Siegman, IEEE Press, New York (1973), pp. 331-351.
88. Santa Barbara Research Center Data Sheet, Santa Barbara, CA.
89. W. M. Rogers and R. L. Powell, "Tables of Transport Integrals," NBS, Circular 595, U.S. Dept. of Commerce, Washington, D.C. (1958).
90. M. Abramowitz and I. E. Stegun, "Handbook of Mathematical Functions," Dover publications, New York (1972).
91. I. S. Gradshteyn and I. W. Ryzhik, Tables of Integrals, Series, and Products, Academic Press, New York (1965).
92. OCLI Catalog, Optical Coating Laboratory, Inc., Technical Products Division, Santa Rosa, CA (1977).
93. D. F. Vanderwerf and J. H. Shaw, Appl. Opt. 4, 209 (1965).
94. R. Spence and W. Wild, J. Chem. Soc. (1935), p. 338.
95. R. L. Nutal, A. H. Laufer and M. V. Kilday, J. Chem. Thermodynamics, 4, 167 (1971).
96. F. Wille and L. Safer, Ann. 568, 34 (1950).
97. W. L. Hase and P. M. Kelley, J. Chem. Phys. 66, 5093 (1977).
98. M. J. Pilling and J. A. Robertson, J. Chem. Soc. Farad. Trans. I, 73, 968 (1977).

99. T. W. Eder and R. W. Carr, Jr., J. Phys. Chem. 73, 2074 (1969).
100. A. N. Strachan and D. E. Thornton, Can. J. Chem. 46, 2353 (1968).
101. J. S. Deech and W. E. Baylis, Can. J. Phys. 49, 90 (1971).
102. D'Yakonov and V. I. Perel, Sov. Phys. JETP, 20, 997 (1965).
103. J. P. Barrat, J. Phys. Radium, 20, 541 (1959).
104. J. P. Barrat, J. Phys. Radium, 20, 633 (1959).
105. J. P. Barrat, J. Phys. Radium, 20, 657 (1959).
106. T. Holstein, Phys. Rev. 72, 1212 (1947).
107. T. Holstein, Phys. Rev. 83, 1159 (1951).
108. A. C. G. Mitchell and M. W. Zemansky, "Resonance Radiation and Excited Atoms," The Macmillan Company, New York (1934), Chapt. 4.
109. H. A. Bethe and E. E. Salpeter, "Quantum Mechanics of One- and Two-Electron Atom," Springer-Verlag, Berlin (1957), p. 352.
110. S. R. Ravan, S. J. Czuchlewski, and M. V. McCusker, Phys. Rev. A, 16, 1892 (1977).
111. C. A. Slocumb, W. H. Miller, and H. F. Schaefer, III, J. Chem. Phys. 55, 926 (1971).
112. F. J. Comes and U. Wenning, Z. Naturforsch., 24a, 587 (1969).
113. F. J. Comes and U. Wenning, Ber. Bunsenges. Physik. Chemie, 73, 901 (1969).
114. J. E. Mentall and E. P. Gentieu, J. Chem. Phys. 52, 5641 (1970).
115. G. V. Volkenburgh, T. Carrington and R. A. Young, J. Chem. Phys. 59, 6035 (1973).
116. W. Braun, C. Calone, T. Carrington, G. V. Volkenburgh, and R. A. Young, J. Chem. Phys. 53, 4224 (1970).
117. W. A. Chupka and J. Berkowitz, J. Chem. Phys. 51, 4244 (1969).

118. W. L. Fite, R. T. Brackman, D. G. Hummer and R. F. Stebbings, Phys. Rev. 116, 363 (1959).
119. J. I. Gersten, J. Chem. Phys. 51, 637 (1969).
120. V. Dose, Comm. Atom. Mol. Phys. 5, 151 (1971).
121. T. W. Hansch, S. A. Lee, R. Wallenstein, and C. Wieman, Phys. Rev. Lett. 34, 307 (1975).
122. S. A. Lee, R. Wallenstein, and T. W. Hansch, Phys. Rev. Lett. 35, 1262 (1975).
123. S. A. Lee, Ph.D. Thesis, Department of Physics, Stanford University (1975).
124. M. Goppert-Mayer, Ann. Physik, 9, 273 (1931).
125. B. Cagnac, G. Grynberg, and F. Biraben, Le Journal de Physique, 34, 845 (1973).
126. F. V. Bunkin, Soviet Physics, JETP, 23, 1121 (1966).
127. E. A. Power and S. Zienau, Phil. Trans. Roy. Soc. (London), A251, 427 (1959).
128. J. J. Sakurai, "Advanced Quantum Mechanics," Addison-Wesley, Reading, Mass. (1967), Chapt. 2.
129. R. E. Moss, "Advanced Molecular Quantum Mechanics," Chapman and Hall, London (1973), Chapt. 12 and 13.
130. Y. Gontier and M. Trahim, Phys. Lett. 36A, 463 (1971).
131. M. Stobbe, Ann. d. Phys. 7, 661 (1930).
132. H. A. Bethe and E. E. Salpeter, "Quantum Mechanics of One- and Two-Electron Atom," Springer-Verlag, Berlin (1957), Sec. 71.
133. T. W. Hansch, Appl. Opt. 11, 895 (1972).
134. R. Wallenstein and T. W. Hansch, Opt. Comm. 14, 353 (1975).

135. R. Wallenstein and T. W. Hansch, Appl. Opt. 13, 1625 (1974).
136. D. Davis and W. Braun, Appl. Opt. 7, 2071 (1968).
137. B. A. Ridley, J. A. Davenport, L. J. Steif, and K. H. Welge, J. Chem. Phys. 57, 520 (1972).
138. E. P. Gentieu and J. E. Mentall, Science, 169, 681 (1970).
139. G. Fleming, M. M. Anderson, A. J. Harrison, and L. W. Pickett, J. Chem. Phys. 30, 351 (1959).
140. R. D. Hudson, "Critical Review of UV Photoabsorption Cross Sections," NBS-38, U.S. Dept. of Commerce, 19 (1971), p. 34.
141. J. V. Michael and R. E. Weston, Jr., J. Chem. Phys. 45, 3632 (1966).
142. R. T. Hodgson (unpublished work).
143. G. S. Hurst, M. H. Navfeh, and J. P. Young, App. Phys. Lett. 30, 229 (1977).
144. G. C. Bjorklund, C. P. Ausschnitt, R. R. Freeman, and R. H. Storz, Appl. Phys. Lett. 33, 54 (1978).
145. P. M. Guyon, W. A. Chupka, and J. Berkowitz, J. Chem. Phys. 64, 1419 (1976).
146. J. O. Hirschfelder, C. F. Curtis, and R. B. Bird, "Molecular Theory of Gases and Liquids," John-Wiley and Sons, Inc. New York (1954), Chapt. 3.
147. J. R. Sodeau and E. K. C. Lee, Chem. Phys. Lett. 57, 71 (1978).
148. H. F. Schaefer, unpublished work.
149. C. Bradley Moore, Ph.D. Thesis, University of California (1963).
150. G. Herzberg and J. W. C. Johns, Proc. Roy. Soc. A, 295, 107 (1966).

151. J. Danon, S. V. Filseth, D. Feldman, H. Zacharias, C. H. Duqan and K. H. Welge, Chem. Phys. 29, 345 (1978).
152. L. E. Giddings, Jr., and K. K. Innes, J. Mol. Spect. 6, 528 (1961).

This report was done with support from the Department of Energy. Any conclusions or opinions expressed in this report represent solely those of the author(s) and not necessarily those of The Regents of the University of California, the Lawrence Berkeley Laboratory or the Department of Energy.

TECHNICAL INFORMATION DEPARTMENT
LAWRENCE BERKELEY LABORATORY
UNIVERSITY OF CALIFORNIA
BERKELEY, CALIFORNIA 94720